UC Santa Barbara

UC Santa Barbara Electronic Theses and Dissertations

Title

Sensitivity Analysis for Mapping Methane with Airborne and Satellite Imaging Spectrometers

Permalink

https://escholarship.org/uc/item/6200j4pd

Author

Ayasse, Alana Kaleikaumaka

Publication Date

2021

Peer reviewed|Thesis/dissertation

eScholarship.org Powered by the California Digital Library
University of California

University of California
Santa Barbara

Sensitivity Analysis for Mapping Methane with Airborne and Satellite Imaging Spectrometers

A dissertation submitted in partial satisfaction
of the requirements for the degree

Doctor of Philosophy
in
Geography

by

Alana Kaleikaumaka Ayasse

Committee in charge:

Professor Dar A Roberts, Chair
Professor Philip E Dennison
Professor Chris C Funk
Professor Jennifer Y King

March 2021

The Dissertation of Alana Kaleikaumaka Ayasse is approved.

Professor Philip E Dennison

Professor Chris C Funk

Professor Jennifer Y King

Professor Dar A Roberts, Committee Chair

January 2021

Sensitivity Analysis for Mapping Methane with Airborne and Satellite Imaging Spectrometers

Copyright © 2021

by

Alana Kaleikaumaka Ayasse

Acknowledgements

I am lucky to have had a plethora of people who have helped me personally and professionally through graduate school. There are too many people to acknowledge and thank but I would like to highlight a few individuals who have been especially important to this journey.

First and foremost, I would also like to thank Andrew Thorpe for his support and guidance throughout all of this work. I am incredibly grateful for everything you have done for me over the last six years. You have been an excellent mentor, collaborator, and I would not be here today without you. In addition to Andrew, I would also like to thank everyone a JPL who worked with me or supported my work.

I would like to thank Dar Roberts, my advisor, for an illuminating and interesting six years. You are truly an amazing teacher and I have learned so much from you. Outside of academics I have enjoyed getting to know you as a person. From discussions on world destruction to songs about compost, there is never a dull moment in your presence. I would like to thank Phil Dennison at the University of Utah, your advice and support made this dissertation possible. I would also like to thank my committee for all the helpful advise and time they put into reading and editing my work.

I would also like to thank all of the VIPER Lab students past and present. Sarah Shivers, Erin Weatherly, Susan Meerdink, and Zach Tane in particular, thank you for your friendship and for teaching me how to survive and navigate graduate school. In addition, I would like to thank all of my fellow geography and UCSB graduate student friends (you know who you are). The friendships, stimulating conversations, and sense of community have made this journey so enjoyable.

Lastly, I would also like to thank my friends and family, near and far, for supporting me through this journey. Thank you to all of the people whom I lived with over the years in Santa Barbara, particularly Kat Millage. Most of all, thank you to Ryan Barnes for the last two years

of constant love and sympathy. I could not have done this without you all.

Curriculum Vitæ

Alana Kaleikaumaka Ayasse

Education

2021	Ph.D. in Geography (Expected), University of California, Santa Barbara.
2013	B.A. in Geography/Environmental Studies and GIS, University of California, Los Angeles.

Publications

In Prep.	Ayasse AK, Thorpe AK, Dennison PE, Roberts DA. Sensitivity of Spectral Resolution, Wind, and Spatial Resolution for Detecting Methane Plumes with Imaging Spectrometers. Remote Sensing of Environment.
2020	Kumar S, Torres C, Ayasse AK, Roberts DA, Manjunath BS. 2020. Deep Learning Remote Sensing Methods for Methane Detection in Overhead Hyperspectral Imagery. IEEE Winter Conference on Applications of Computer Vision. pp. 1776-1785.
2019	Ayasse AK, Dennison PE, Foote M, Thorpe AK, Roberts DA, Green RO, Thompson D. 2019. Remote Sensing of Point Source Methane Emissions with Future Satellite Sensors. Remote Sensing. 11(24), 3054.
2018	Ayasse AK, Thorpe AK, Roberts DA, Funk CC, Dennison PE, Frankenberg C, Steffke A, Aubrey AD. 2018. Evaluating the effects of surface properties on methane retrievals using a synthetic airborne visible/infrared imaging spectrometer next generation (AVIRIS-NG) image. Remote Sensing of Environment. 215: 386-397.

Posters and Presentations

2019	Ayasse AK, Dennison PE, Foote M, Thorpe AK, Roberts DA, Green RO, Thompson D. 2019. Point Source Methane Mapping with Future Satellite Imaging Spectrometers. AGU Fall Meeting.
2017	Ayasse AK, Thorpe AK, Roberts DA, 2017. The Effects of Surface Properties and Albedo on Methane Retrievals with the Airborne Visible/Infrared Imaging Spectrometer Next Generation (AVIRIS-NG). Poster. AGU Fall Meeting.
2016	Ayasse AK, Thorpe AK, Roberts DA, Aubrey AD, Dennison PE, Frankenberg C, Thompson DR, Frankenberg C. 2016. Evaluating the Effects of Surface Properties on Methane Detection with the Airborne Visible/Infrared Imaging Spectrometer Next Generation (AVIRIS-NG). Poster. AGU Fall Meeting.

2015	Ayasse AK, Thorpe AK, Roberts DA, Aubrey AD. 2015. Sensitivity Analysis for the Remote Sensing of Methane using the Airborne Visible/Infrared Imaging Spectrometer (AVIRIS). Poster. AGU Fall Meeting.

Research Experience

2015 – Present	Graduate Student Researcher, UCSB Received a JPL Subcontract to test the sensitivity of methane detection with AVIRIS-NG and to explore the potential for satellite mapping of methane with future space borne imaging spectrometers.
2013	Research Assistant/Field Observer, UCLA Conducted field-testing in major intersections in Los Angeles to measure the effects of urban form and traffic on pedestrian exposure to air pollution.
2013	Field Assistant, UCLA/Botswana Constructed and installed meteorological towers and equipment in the Southern Kalahari Desert to measure climate and dust emission potential.

Professional Experience

2017-2019	Graduate Student Board Member, UCSB Coastal Fund Review and award grants to local non-profits, students, and faculty who work to protect, enhance, understand, and restore the UCSB coastal environment.
2012	Student Volunteer/Intern, Environmental Protection Agency Region 9 Complied a user manual for residents of a superfund site in West Oakland on how they can use fertilizer to amend their soil and reduce the risk of lead poisoning from the soil.

Teaching Experience

2020	Teaching Associate, UCSB Geography: Remote Sensing of the Environment 2
2017-2020	Teaching Assistant, UCSB Geography: Remote Sensing of the Environment 1 Geography: Remote Sensing of the Environment 2 Geography: Environmental Optics Geography: Physical Oceanography

2018	Mentor, NASA Student Airborne Research Program (SARP) Terrestrial Remote Sensing Group

Technical Skills

programming	IDL, MATLAB, R, Python
Software	ENVI, ArcGIS, GGIS, MODTRAN

Abstract

Sensitivity Analysis for Mapping Methane with Airborne and Satellite Imaging Spectrometers

by

Alana Kaleikaumaka Ayasse

Atmospheric methane has been increasing in concentration since the beginning of the Industrial Era due to anthropogenic emissions. Methane has many anthropogenic sources, including the oil and gas industries, agriculture, and waste management. There continues to be considerable uncertainty regarding the contribution of each source to the total methane budget; therefore, remote sensing techniques for monitoring and measuring methane emissions are of increasing interest. Imaging spectrometers have proven to be a valuable instrument for quantitative mapping of point source methane plumes. However, there are significant uncertainties regarding the sensitivity of the retrieval algorithms, including the influence of albedo, the impact of surfaces that may cause spurious signals, aerosols, and the influence of the wind speed on flux estimations. In addition, questions remain regarding the potential to move these sensors from airborne platforms to satellites. I explore these sensitivities to help improve accurate mapping of this important greenhouse gas. I also explore the possibility to expand our ability to map point sources methane plumes from a a local scale to a global scale. The findings from this study help define the accuracy and limitations of current and future systems for methane mapping and outline what is needed in order to map point source methane globally.

Contents

Curriculum Vitae **vi**

Abstract **ix**

1 Introduction **1**
1.1 Atmospheric Methane 1
1.2 Imaging Spectrometers and Absorption Spectroscopy 3
1.3 Mapping Methane with AVIRIS-NG 5
1.4 Research Motivation and Summary of Chapters 7

2 Evaluating the Effects of Surface Properties on Methane Retrievals Using a Synthetic AVIRIS-NG Image **10**
2.1 Abstract 11
2.2 Introduction 12
2.3 Methods 15
2.3.1 Synthetic Image 15
2.3.2 The IMAP-DOAS Retrieval Algorithm 23
2.4 Results 24
2.4.1 Aerosol Scattering 24
2.4.2 IMAP-DOAS 25
2.4.3 Surface Type 31
2.4.4 Albedo 35
2.5 Discussion 36
2.5.1 Albedo 37
2.5.2 Surface Type 38
2.5.3 Comparison to Real AVIRIS-NG Images 41
2.5.4 Limitation and Potential Solutions 42
2.6 Conclusions 44

3 Methane Mapping with Future Satellite Imaging Spectrometers **45**
3.1 Abstract 46

3.2 Introduction . . . 46
3.3 Methods . . . 48
3.3.1 Imagery . . . 49
3.3.2 Simulated Satellite Images . . . 50
3.3.3 Matched Filter Methane Retrieval . . . 53
3.3.4 Integrated Mass Enhancement . . . 54
3.3.5 Flux Estimate . . . 55
3.4 Results and Discussion . . . 56
3.4.1 Methane Plumes by Sector . . . 56
3.4.2 Flux . . . 64
3.4.3 Spatial Resolution and Signal-to-Noise Ratio . . . 66
3.4.4 Limitations . . . 68
3.5 Conclusions . . . 69

4 Exploring the Effects of Wind Speed, Flux Rate, and Spatial Resolution on Mapping Methane Plumes with Imaging Spectrometers 71
4.1 Abstract . . . 72
4.2 Introduction . . . 73
4.3 Methods . . . 76
4.3.1 Synthetic Images . . . 76
4.3.2 Matched Filter . . . 77
4.3.3 IMAP-DOAS . . . 78
4.3.4 Large-Eddy Simulation Plumes . . . 79
4.3.5 Thresholds and Plume Detection . . . 81
4.3.6 Calculated Flux Rates . . . 83
4.4 Results . . . 84
4.4.1 Thresholds . . . 84
4.4.2 Spatial Resolution and Wind Speed . . . 91
4.5 Discussion . . . 97
4.5.1 Thresholds . . . 97
4.5.2 Spatial Resolution . . . 99
4.5.3 Wind Speed . . . 101
4.6 Conclusion . . . 103

5 Conclusion 105

Bibliography 109

Chapter 1

Introduction

1.1 Atmospheric Methane

Methane (CH_4) is a potent greenhouse gas that contributes significantly to global climate change. It is the second most important greenhouse gas after carbon dioxide. While there is significantly more carbon dioxide than methane in the atmosphere a single molecule of methane has 86 times more radiative forcing abilites than carbon dioxide. [1]. Overall methane is estimated to be responsible for about 20 percent of all global warming. [2]. In addition methane has a much shorter atmospheric life time than carbon dioxide, 12-15 years versus 100 year. Consequently, methane makes an excellent mitigation target. However, in order to effectively reduced emissions, it is important to understand, at a source specific scale, where emissions are coming from.

Methane emissions have both natural and anthropogenic sources; natural sources are thought to make up about 40 percent of methane emissions while anthropogenic sources make up the other 60 percent [3]. While natural methane emissions have existed long before humans, anthropogenic methane emissions have increased substantially due to human activities and are now contributing to global climate change. Anthropogenic methane emissions come from three

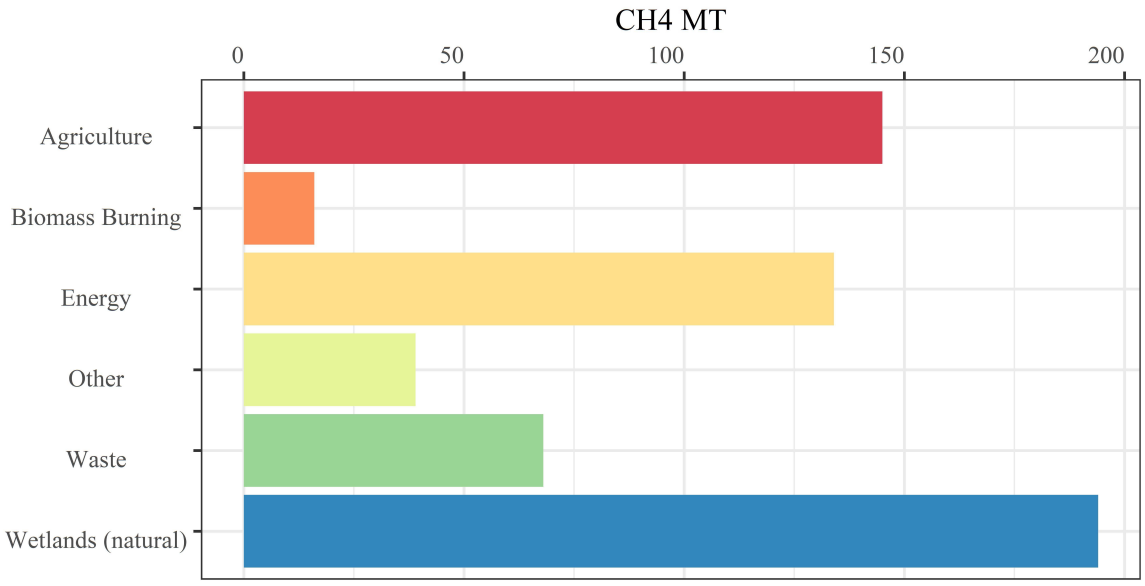


Figure 1.1: Methane emissions in million tonnes (MT) per year by sector. [3]

major sectors: the energy sector, agriculture (specifically livestock), and the waste management industry. Figure 1.1 shows the relative amount of methane from the three major anthropogenic sources as well as the major natural source. Traditional methods of studying methane from these sources, such as scientific aviation, flux towers, and large-scale satellite data, have made significant progress in constraining the methane budget [4, 5, 6, 7]. However, these techniques lack the ability to directly attribute a methane emission plume to a specific source. For example, traditional methods can characterize the basin wide flux from an area with heavy oil and gas infrastructure but cannot pinpoint which well, compressor station, or storage tank is emitting methane. In order to effectively target mitigation efforts, knowledge of the specific emitting source is important.

Recently the Airborne Visible InfraRed Imaging Spectrometer Next Generation (AVIRIS-NG) and similar imaging spectrometers have been used to map methane plumes. These instruments can map methane plumes, quantify the size and flux of the plume, and directly attribute the plume to a specific source. However, AVIRIS-NG can only monitor a limited area and

satellite platforms are needed to understand global emissions. Expanding this type of work is key to enacting an effective mitigation strategy.

1.2 Imaging Spectrometers and Absorption Spectroscopy

Imaging spectrometers are a class of remote sensing instruments defined by a narrow spectral bandwidth and a high number of bands. Traditionally this class of instruments has a $\sim$10 nm spectral spacing and $>$100 bands. AVIRIS-NG, an imaging spectrometer that is featured heavily throughout this work, is a push-broom instrument with a 36-degree Field of View (FOV) and 432 spectral channels between 380 and 2510 nm, with a 5 nm spectral spacing and a 6 nm Full Width Half Maximum (FWHM) [8]. See Table 1.1 for more details on AVIRIS-NG. AVIRIS-NG and other operational imaging spectrometers, such as the National Earth Observation Network Airborne Observation Platform (NEON AOP) and the Global Airborne Observatory (GAO) [9, 10] were originally designed as instruments to map terrestrial surfaces. The high spectral resolution and sampling can identify different physical and biological characteristics of soils, rocks, and plants [11]. However, imaging spectrometers are also very sensitive to the atmosphere including absorption by greenhouse gases.

Table 1.1: AVIRIS-NG specifications and characteristics.

Parameter	**Value**
Wavelength	380 nm to 2510 nm
FWHM	6 nm
Spectral Resolution	5 nm
Field of View	36 degrees
Spatial Sampling	1 mrad
Spatial Resolution	0.3 to 20 m
SNR @ 600 nm	2000 nm
SNR @ 2200 nm	1000 nm

Greenhouse gases, like methane, have specific absorption bands in infrared wavelengths.

These are due to vibrational and rotational absorptions caused by bonds between atoms with in the gas molecules. In the case of methane, this is the carbon and hydrogen bonds. Methane specifically has its fundamental absorption features in the mid and thermal infrared [12], which are outside of the wavelength ranges of AVIRIS-NG and most Visible Infrared and Short Wave InfraRed (VISWIR) imaging spectrometers. However, overtones and combinations of the fundamental vibrational models produce weaker but significant absorption features in the short-wave infrared (SWIR) which is within the wavelength range of some imaging spectrometers, like AVIRIS-NG. Water vapor and carbon dioxide, two other dominate greenhouse gases, also have absorption features in the SWIR that overlap partially with methane [13, 14]. This leaves two small windows where we can see methane. The first window is around 1600 nm, where the methane is distinct but has a weak absorption. The second, and more commonly used window, is around 2300 nm, where methane is the strongest absorber at typical atmospheric concentrations [15] (Figure 1.2).

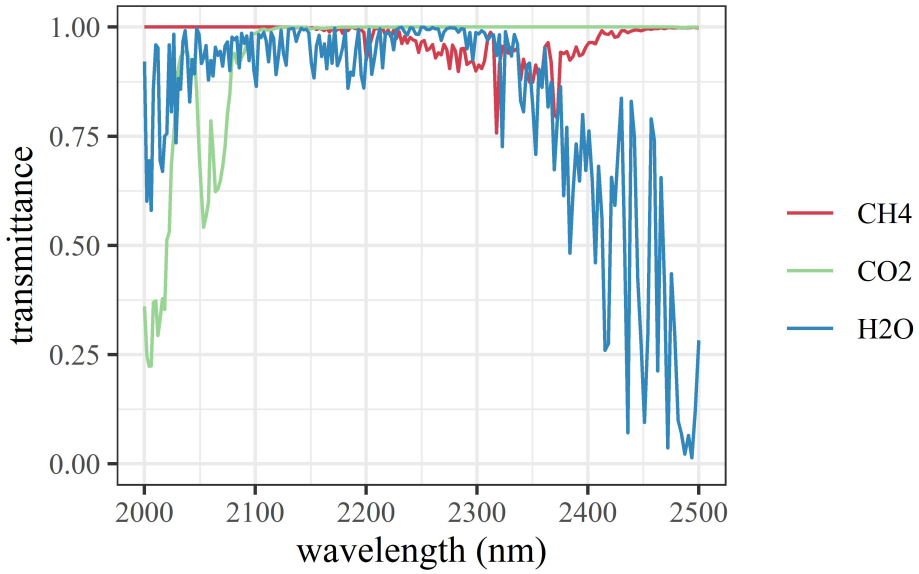


Figure 1.2: The transmittance spectra of methane, water vapor, and carbon dioxide in the short-wave infrared. Note the area around 2300 nm where methane is the primary absorber.

The depth of the absorption feature can be described using Beer-Lambert's law which states

that the attenuation or absorption of light is directly related to the materials through which the light is traveling. Transmitted radiance decreases exponentially as a product of the number of absorbers and the strength of the absorber. The strength of the absorber, or the absorption coefficient, is wavelength dependent. In the case of atmospheric methane, the absorption coefficient for a molecule of methane at a given wavelength is known and is static. The number of absorbers is a function of both concentration of methane and the pathlength (distance) along which light travels. Thus, if path lengths are equivalent, we can assume that a deeper absorption feature indicates more methane in the air column. This information can be applied to imaging spectrometer data and is the physical basis behind detecting and quantifying methane with imaging spectrometers.

1.3 Mapping Methane with AVIRIS-NG

The use of remote sensing to map methane is well established. Historically methane has been mapped using atmospheric sounders such as the Atmospheric Infrared Sounder (AIRS) [16]or high spectral resolution and low spatial resolution non- imaging spectrometers such as the SCanning Imaging Absorption spectroMeter for Atmospheric CartograpHY (SCIAMACHY) aboard Envisat [17] or the TROPOspheric Monitoring Instrument (TROPOMI) [18]. The use of an imaging spectrometer, such as AVIRIS-NG, to map methane is a much more recent development. Since 2010 the use of imaging spectrometers to map methane has gone from a proof-of-concept to an integral part of our carbon monitoring system. In 2010, Roberts et al. published the first paper that demonstrated imaging spectrometers could be used to map methane [15]. Previous studies had only used imaging spectrometers to map other greenhouse gasses such as water vapor and carbon dioxide. Water vapor and carbon dioxide are far more abundant in the atmosphere, and therefore their spectral signatures are more prominent. While methane has a relatively high absorption coefficient in the SWIR compared to water vapor

and carbon dioxide, much lower concentrations produce a smaller signature. In order to show that methane could also be mapped with an imaging spectrometer, Roberts et al. (2010) took advantage of sun glint over the Coal Oil Point methane seep and was able to map a methane signature. In 2011 Bradley et al. further proved that methane could be mapped with an imaging spectrometer by developing a SWIR band ratio technique [19]. This again used sun glint over the Coal Oil Point methane seep. Although the band ratio worked well for sun glint, it was not an optimal technique for more spectrally diverse surfaces. In order to map methane over a diversity of surfaces, Thorpe et al. (2012) applied a cluster tuned matched filter to AVIRIS data to map methane [20]. The cluster tuned matched filter has previously been used to map weak gas signatures in thermal hyperspectral imagery[21]. This was successfully applied at the Coal Oil Point seep and in 2013 it was applied over a spectrally diverse area as well [22]. By showing that methane could be mapped over a spectrally diverse setting, they also demonstrated that methane emissions from anthropogenetic sources could be targeted with this technique. The cluster tuned matched filter could identify a methane plume, but it could not provide the total abundance of methane in the plume. Quantitative gas mapping using remote sensing had been used in other missions such as SCIAMACHY [23]. However, those sensors had very fine spectral resolution, which made a quantitative estimate of the abundance of gas slightly easier. In 2014 Thorpe et al. successfully applied the quantitative retrieval used on SCIAMACHY data to AVIRIS-NG data and proved that not only can we detect methane, but we can also quantitatively measure the amount of methane in an air-column with an imaging spectrometer [24].

From then on, mapping methane with an imaging spectrometer moved away from a strictly proof of concept exercise to being applied to do carbon science. Frankenberg et al. (2016) applied the AVIRIS-NG instrument to map oil and gas related plumes in the Four Corners area. This study showed how this instrument could map the size, distribution, and exact sources of point source methane plumes over a large area [25]. At the end of 2015 and into the beginning

of 2016, the Aliso Canyon gas storage facility had a major well blowout that released a record amount of methane into the atmosphere. Thompson et al. (2016) were able to harness the now defunct satellite imaging spectrometer Hyperion to map the blowout [26]. This study showed that there was potential to not only use an airborne instrument to map point source plumes but also that satellite imaging spectrometers could potentially do it as well.

Beginning in 2016 the AVIRIS-NG instrument began to fly hundreds of methane specific flights over potential methane sources in California. This work culminated in a 2019 paper published in *Nature* that showed exactly which sources in California were emitting the most methane and provided a clear path forward for how this type of work could be used to target the highest emitting facilities and significantly reduce methane emissions [27]. Also, in 2019 more work was published supporting the possibility to map point source emissions with imaging spectrometers. Work presented in this dissertation (chapter 3) and Cusworth et al. (2019) both showed that upcoming imaging spectrometers missions have the capability for mapping methane [28, 29]. In addition, private aerospace companies, such as GHGSat, began experimenting with using imaging spectrometers to map point source methane plumes from space [30]. By 2020 AVIRIS-NG and similar instruments have become an integral part of the carbon observatory and are being integrated with other data sources to provide a holistic view of carbon emissions [31].

1.4 Research Motivation and Summary of Chapters

As mapping methane with imaging spectrometers is integrated into the global carbon monitoring efforts and more instruments similar to AVIRIS-NG are launched into space, it is critical to understand the capabilities and sensitivities of these instruments. The motivation behind this dissertation is to better understand what factors can affect methane detection. The key factors include the underlying land cover and the wind speed at the time of the image acquisition to the

spatial resolution and signal-to-noise ratio of the sensor. Throughout this dissertation I also explore how synthetic images can be created and used to test the sensitivity to the aforementioned factors.

In Chapter 2, I use synthetic AVIRIS-NG images to understand how the underlying land cover can affect methane detection. I quantitatively show how and why albedo is the most significant source of error in methane mapping. I also show how surfaces with an absorption feature similar to the methane absorption feature can act as confusers and also cause a large amount of error in the results. Lastly, I show that the land cover is a larger source of error than aerosols.

In Chapter 3, I use the methods developed to create the synthetic images to develop images that represent data from proposed satellite sensors. I then use these images to test the capabilities of measuring methane from space. I show that point source methane plumes from a variety of anthropogenic sources can be mapped with these proposed imaging spectrometers. I also show, that spatial resolution may be the most important factor for accurately mapping methane plumes.

Lastly, in chapter 4, I look more closely at the effect of spatial resolution and the effects that wind speed and flux rates have on methane detection. Here I utilize synthetic images to quantitatively determine methane detection thresholds. I then apply the threshold to Large Eddy Simulation (LES) plumes. The LES plumes allow for the isolation and analysis of the effect of wind speed and spatial resolution on the detection limits and how errors propagate into the calculated flux.

The results from this study are crucial for advancing the understanding of the sensitivities and limitation of mapping methane with imaging spectrometers. Without these results, we cannot know if the design of the instruments will be able to map the methane plumes of interest. These results also will help to inform best practices when applying the data to real world challenges. Lastly, this study provides an analysis of the instrumentation and methods needed

to map point source methane globally.

Chapter 2

Evaluating the Effects of Surface Properties on Methane Retrievals Using a Synthetic AVIRIS-NG Image

With Andrew K Thorpe, Dar A Roberts, Christian Frankenberg, Andrew D Aubrey, Philip E Dennison, Christopher C Funk, and Andrea Teffke

This chapter is based off a manuscript published in the journal Remote Sensing of Environment:

Ayasse, A.K.; Thorpe, A.K.; Roberts, D.A.; Frankenberg, C.; Aubrey, A.D.; Dennison, P.E.; Funk, C.C.; Teffke, A. Evaluating the effects of surface properties on methane retrievals using a synthetic airborne visible/infrared imaging spectrometer next generation (AVIRIS-NG) image. Remote Sens. Environ. 2018, 215, 386–397.

2.1 Abstract

Atmospheric methane has been increasing since the beginning of the industrial era due to anthropogenic emissions. Methane has many sources, both natural and anthropogenic, and there continues to be considerable uncertainty regarding the contribution of each source to the total methane budget. Thus, remote sensing techniques for monitoring and measuring methane emissions are of increasing interest. Recently, the Airborne Visible-Infrared Imaging Spectrometer - Next Generation (AVIRIS-NG) has proven to be a valuable instrument for quantitative mapping of methane plumes. Despite this success, uncertainties remain regarding the sensitivity of the retrieval algorithms, including the influence of albedo and the impact of surfaces that may cause spurious signals. To explore these sensitivities, we applied the Iterative Maximum a Posterior Differential Optical Absorption Spectroscopy (IMAP-DOAS) methane retrieval algorithm to synthetic reflected radiances with variable methane concentrations, albedo, surface cover, and aerosols. This allowed for characterizing retrieval performance, including potential sensitivity to variable surfaces, low albedo surfaces, and surfaces known to cause spurious signals. We found that dark surfaces (below 0.10 μWcm^{-2}nm^{-1}sr^{-1} at 2139 nm), such as water and green vegetation, and materials with absorption features in the 2200 - 2400 nm range caused higher errors in retrieval results. We also found that aerosols have little influence on retrievals in the SWIR. Results from the synthetic scene are consistent with those observed in IMAP-DOAS retrievals for real AVIRIS-NG scenes containing methane plumes from a waste dairy lagoon and coal mine ventilation shafts. Understanding the effect of surface properties on methane retrievals is important given the increased use of AVIRIS-NG to map gas plumes from a diversity of sources over variable landscapes.

2.2 Introduction

Methane (CH_4) is a potent greenhouse gas that contributes significantly to global climate change. Methane is estimated to be responsible for about 20 percent of the total global warming induced by anthropogenic greenhouse gases [2] and abundances have been increasing since the industrial revolution [32]. However, from 1999 to 2006 the growth rate stagnated only to rise again starting in 2007 [33, 34]. The cause of this stagnation and subsequent rise is still debated. Some argue that the increase in methane is due to the natural gas industry while others argue it is due to increased emissions from wetlands [35, 36, 37]. Other studies point to changes in the methane lifetime [38, 39]. Regardless of cause, the recent unexpected rise in methane reflects our uncertainty regarding the contribution of various sources to the total methane budget. In addition, recent increases in atmospheric methane have revived concern about its relative contribution to global warming, which has resulted in some states, such as California, enacting new regulations to curb emissions (SB-1383, Lara, 2016; AB-1496, Thurmond, 2015). These policy measures underscore the importance of unraveling sectoral contributions through deployment of effective techniques for monitoring and quantifying methane emissions.

Using remote sensing to study greenhouse gases, such as methane, has gained prominence over the last decade [40]. There have been a variety of instruments launched into space with the goal of observing methane and other greenhouse gases. The Atmospheric Infrared Sounder (AIRS), the SCanning Imaging Absorption SpectroMeter for Atmospheric CHartographY (SCIAMACHY), and the Greenhouse gases Observing SATellite (GOSAT) are three such examples [41, 42, 43]. These sensors generate global maps of gas concentrations with coarse spatial resolutions on the order of kilometers. AIRS, SCIAMACHY, and GOSAT have greatly increased our understanding of global methane distribution and quantity, but lack the spatial resolution to directly attribute observed emissions to individual sources. Finer spatial resolution sensors are necessary to improve sensitivity to local emissions sources. For exam-

ple, the 30 m pixel resolution of the Hyperion imaging spectrometer enabled the space-based detection of a methane plume from Aliso Canyon [26]. However, the Aliso Canyon plume was anomalously large and Hyperion was not well suited for methane detection given an aged focal plane at the time of detection and low signal-to-noise ratio in wavelength regions capturing methane absorption [44].

In addition to space-based observations, airborne observations have also been used to detect and measure methane. Airborne remote sensing has fine spatial resolution and is well suited to resolving individual sources, although these retrievals are limited in time. Current airborne sensors used to measure methane emissions include the Methane Airborne MAPper (MAMAP), a non-imaging spectrometer specifically designed to map methane and carbon dioxide [45]. This sensor was able to obtain flux estimates from point sources such as landfills and coal mine ventilation shafts [46, 47]. MAMAP and other similar sensors are able to make very accurate column concentration estimates but must fly many downwind transects in order to map a full plume. This makes detection of emissions from unknown sources difficult, and these sensors are best suited for studying known methane sources. More recently, imaging spectrometers have been used to map methane. Thermal imaging spectrometers such as Mako and the Hyperspectral Thermal Emission Spectrometer (HyTES) have successfully mapped methane plumes from multiple sources [48, 49]. However, the sensitivity of these sensors to emissions near the ground depends on the thermal contrast between the ground and atmosphere and decreases as flight altitude increase, which in turn limits ground coverage.

The Airborne Visible and Infrared Imaging Spectrometer (AVIRIS) and the Next Generation instrument (AVIRIS-NG) are imaging spectrometers that measure reflected solar radiation in the visible and shortwave infrared (VSWIR) and have also been used to map methane emissions [25, 15, 50, 51, 22]. AVIRIS measures a spectral range between 400 and 2500 nm and has a 10 nm spectral sampling [11] while AVIRIS-NG measures the same spectral range with 5 nm spectral sampling and improved signal to noise ratio (SNR) [8]. AVIRIS-NG has a 34 degree

field of view with a 1 milliradian instantaneous field of view that results in spatial resolutions that typically range between 1 to 8 meters depending on the flight altitude. These sensors were not originally designed to map greenhouse gases but their sensitivity to gas absorption features between 900 nm and 2500 nm has allowed for detection and quantitative mapping of methane, carbon dioxide, and water vapor [19, 52, 53, 15, 51]. Recently, quantitative retrievals have been developed to estimate column concentrations of methane from AVIRIS-NG data [50, 51, 24]. For example, the Iterative Maximum a Posterior Differential Optical Absorption Spectroscopy algorithm (IMAP-DOAS) [23] was adapted for AVIRIS-NG [51]. Success using AVIRIS-NG for methane mapping has prompted multiple flight campaigns in the Western United States focused on mapping methane emissions from the energy sector [50, 25, 51].

Although AVIRIS-NG has been used successfully to map methane plumes, there are still uncertainties regarding the sensitivity of the retrieval algorithms, including the influence of albedo on results and the impact of surfaces that can cause spurious signals. Low albedo surfaces reduce the observable difference in reflected radiance between a background methane concentrations and enhanced concentrations. At the 5 nm spectral sampling of AVIRIS-NG, surfaces with absorption features in the shortwave infrared can mimic the absorptions caused by methane. In this study, we apply the IMAP-DOAS algorithm to a synthetic image with variable methane concentrations, surfaces, and albedo. In an observed AVIRIS-NG scene we cannot control the exact column concentration of a gas, but synthetic radiances based on accurate radiative transfer modeling allows us to control these values and therefore test the accuracy of the algorithms used to estimate the gas concentrations [52, 54, 55]. In addition, the land cover properties, such as albedo and surface type, can be controlled, allowing us to test the sensitivity of the algorithms to these factors. The ability to manipulate these parameters allows us to quantify how the retrieval algorithm is impacted by variations in albedo, surface type, and specific surfaces known to cause spurious signals in order to improve our understanding of retrieval results. In this study, we will first create a synthetic image, run the IMAP-DOAS

retrievals algorithm on the synthetic image, and then compare the retrieved CH_4 values to the known values.

2.3 Methods

The general method for this study is to create a synthetic image and to run the IMAP-DOAS algorithm on the synthetic image. Figure 2.1 summarizes the workflow for creating the synthetic image and the steps to achieve the results discussed subsequently. Details on the synthetic image and IMAP-DOAS algorithm are discussed below.

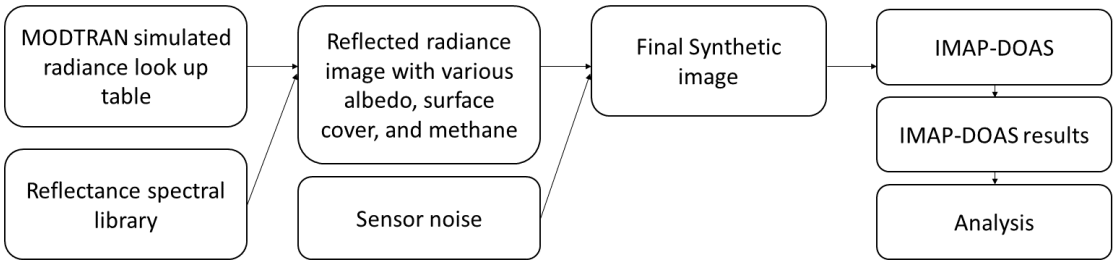


Figure 2.1: Workflow framework for the study.

2.3.1 Synthetic Image

The synthetic image used in this study consists of three main components; it has 30 different surface types modeled at 50 surface albedos and 25 different methane concentrations. MODTRAN 5.3, a radiative transfer model, was used to simulate reflected solar radiance spectra for the synthetic image [56]. MODTRAN is commonly used to create lookup tables for many atmospheric correction algorithms including ACORN [57, 58] FLAASH [59, 60] , and ATCOR [53, 61]. It has also been used in a similar way to retrieve water vapor and carbon dioxide from AVIRIS images [53]. We generated a radiance look up table that consisted of

radiance files with 1,000 brightness levels and 25 methane concentrations. The methane concentration within the lowest 1 km of the atmosphere, intended to simulate a methane plume or local emission source, ranged from 0 ppm to 12.5 ppm above a background of 1.864 ppm with a 0.5 ppm step (Figure 2.2). The MODTRAN atmospheric profiles used to generate these synthetic radiances were modified to match profiles used in the IMAP-DOAS retrieval. Assuming a 4 km sensor height and a nadir view zenith angle, two-way transmittance (upwelling and downwelling) was calculated for the atmospheric layers below the sensor, including the 1 km layer with variable methane concentrations (Figure 2.2). The solar reflected radiance was then convolved to the AVIRIS-NG wavelengths using the AVIRIS-NG sensor response function; this produced 432 bands with approximately 5 nm full width half maximum.

The additional atmospheric and geometric variables included in the model were held constant and are listed in Table 2.1. These variables reflect typical conditions under which AVIRIS-NG data are collected. The sensor height in the original studies using AVIRIS Classic to detect methane was 8.95 km [19, 15]. Recent AVIRIS-NG flight campaigns that have targeted methane emissions had sensor heights ranging from 0.43 to 3.8 km with the average around 3 km [27, 62]. In this study, a height of 4 km was chosen to reflect the upper limit of typical AVIRIS-NG flights for methane mapping. Given this sensor height, methane concentrations were calculated in units of mixing ratio-path length (ppm-m) for the 0 to 4 km layer to permit direct comparison between the modeled concentrations in the synthetic image and the IMAP-DOAS retrieval results. The volume mixing ratios (VMRs) generated by MODTRAN for each kilometer layer of the 0-4 km layer were multiplied by 1000 m and summed. The lowest methane concentration modeled in the image is 6,264 ppm-m and the highest concentration, with a 12.5 ppm enhancement above background, is 18,764 ppm-m. The background carbon dioxide, water vapor, location, date, and time of day all represent typical conditions for AVIRIS-NG data collection. The MODTRAN visibility was set at 30 km for a rural atmosphere, including scattering components comprised of 70 percent ammonium, calcium sulfate,

and other organic compounds and 30 percent dust like aerosols [63]. Additional testing was done to determine that a single visibility was sufficient.

Scattering from aerosols in the atmosphere is hypothesized to have a minimal impact on AVIRIS-NG methane retrievals due to the small amount of scattering in the shortwave infrared (SWIR 1100 to 3000 nm) [52]. In order to test this assumption and to be confident that the use of a single 30 km visibility was sufficient, we created a small synthetic image with all of the same attributes described below but with a 5 km visibility for a rural atmosphere. The 30 km visibility atmosphere has a total column extinction coefficient of 0.177 and the 5 km visibility atmosphere has a 1.082 total column extinction coefficient (MODTRAN normalizes the extinction coefficient to 1 at 550 nm). The 5 km visibility value was chosen because it is an extreme example, therefore any effects from aerosols should be apparent based on the differences between 5 and 30 km visibility. This image had the same variable land cover and albedo (described below) but only had three methane concentration (1.864 ppm, 2.864 ppm, 9.864 ppm). The IMAP-DOAS algorithm was run on this image in the same way described later (see Section 2.3.2) and the results are reported in Section 2.4.

The spectra selected for this study represent surface types common in both natural and urban areas. The surfaces include common cover types imaged by AVIRIS-NG and surfaces hypothesized to be challenging for methane mapping. The majority of the surface spectra used to construct the synthetic image were derived from a spectral library originally developed by Roberts et al. (2017) that consists of spectra representing urban and natural environments in Southern California [64]. The spectra were originally collected from a combination of Analytical Spectral Device (ASD) measurements and AVIRIS Classic data. Two additional spectra were obtained from other sources, a calcite spectrum from the US Geological Survey and oil coated vegetation from an AVIRIS Classic image of the Louisiana coastline following the Deep Water Horizon oil spill [65]. The spectral library was convolved and resampled to AVIRIS-NG band centers and full-width half maxima. The surface types are broken up into eight main

Table 2.1: AVIRIS-NG inputs for the MODTRAN simulation. The attributes are the environmental factors affecting the radiative transfer model and the values are the modeled values. All attributes remain constant except for albedo and methane.

Attribute	**Values**
Sensor height	4 km
Wavelengths	350-2500 nm
Carbon dioxide	405 ppm
Water Vapor	1.535 cm
Visibility	30 km
View zenith angle	0 degrees
Latitude	34.1
Longitude	-118.4
Day of Year	262
Time (UTC)	21.30
Solar Zenith Angle	29.77 degrees
Methane (1 km layer)	1.864-14.364 ppm

categories: Green Vegetation (GV), Non-Photosynthetic Vegetation (NPV), soil (or bare soil), water, paved material, roofs, rocks, and "confusers". Previous studies have hypothesized that surfaces with strong hydrocarbon absorptions can be potential confusers[22] , therefore the spectra in the confuser class were selected because they contained hydrocarbons or similar SWIR absorptions, which might interfere with the methane absorption features. This class consists of materials such as white painted commercial roof (WPCR), calcite, plastic covered vegetation (greenhouse), and oil-coated vegetation. The individual spectra used in all the classes are listed below in Table 2.2.

The spectral library reflectance data were converted to radiance using the aforementioned look up table. For each wavelength of each reflectance spectrum, the reflectance value was matched with the closest simulated reflectance value for a specified methane concentration [52]. The corresponding radiance from the lookup table was then extracted, and the process was repeated for the next wavelength. This was then repeated for every methane concentration and every reflectance spectrum, to create a synthetic image of radiance spectra with known

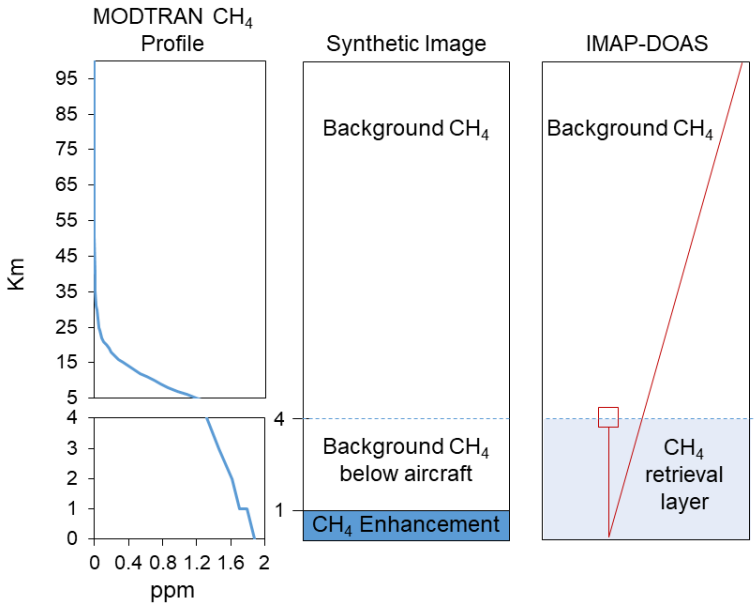


Figure 2.2: The left panel is the methane profile modeled by MODTRAN for an atmosphere with no methane enhancement. The bottom 0-4 km layer is plotted on a different scale then the 5-100 km layer. The middle panel is a schematic of how the synthetic image models methane in the atmosphere. The far right panel shows IMAP-DOAS retrieval layers, and the light blue layer is below the sensor where the algorithm allows for methane perturbation. For the IMAP-DOAS retrieval, the methane profile above the sensor (white layer) remains constant. The red square represents the sensor and the red line represents transmittance path from the sun to the sensor.

atmospheric parameters.

The layout of the synthetic image is such that there are 30 "boxes" on the grid, and each box represents a single background spectrum. The bottom half of the box has methane concentrations grading from 0 to 12.5 ppm above background in 25 steps. The top half of the box uses background methane throughout the entire atmosphere. The reflectance of the background spectrum varied from 2 percent on the left to 52 percent on the right. Figure 2.3 depicts how the surface type, methane, and albedo vary across the image. The gridded layout allowed for easy visual analysis of the performance of IMAP-DOAS algorithm. A noise component aimed at mimicking sensor noise was added using noise equivalent delta radiance (NEdL) to param-

eterize random noise [52]. NEdL is the minimum change in radiance distinguishable from sensor noise and varies by wavelength and radiance level. For each pixel at each wavelength, the NEdL value is calculated by using the original radiance value and NEdL coefficients that were calculated by Dennison et al. (2013) [52]. A random number between 0 and 2 was generated and multiplied by the NEdL value so that different amounts of noise were added to each pixel with the average amount being the original NEdL value. The result was then added to the original radiance value. The purpose of varying NEdL was not to simulate the radiance distribution of sensor noise, but rather to create random but true to life variation in each pixel. The total size of the image was 500 by 612 pixels.

Table 2.2: The surface type and spectra used to create the synthetic image.

Land Cover Class	**Surface Name**
Confusers	Oil coated vegetation
	White painted commercial roof 1 (WPCR1)
	Calcite
	Plastic covered crops
	White painted commercial roof 2 (WPCR2)
	White painted commercial roof 3 (WPCR3)
Green Vegetation (GV)	Ceanothus (CEME)
	Wetland Vegetation (MARSH)
	Coyote brush (BAPI)
	Willow (SASP)
	Golf course grass
	Palm tree
Water	Hope Lake
	Ocean water (glint)
Non-Photosynthetic Vegetation (NPV)	Dead grass
	Evergreen bark
	Bark
	Needle litter
Paved Surface	Airport asphalt
	Concrete bridge
	Concrete parking structure 1
	Concrete parking structure 2
	Tennis court
Roof	Asphalt and gravel roof
	Red tile roof
Soil	Soil 1
	Soil 2
	Soil 3
	Soil 4

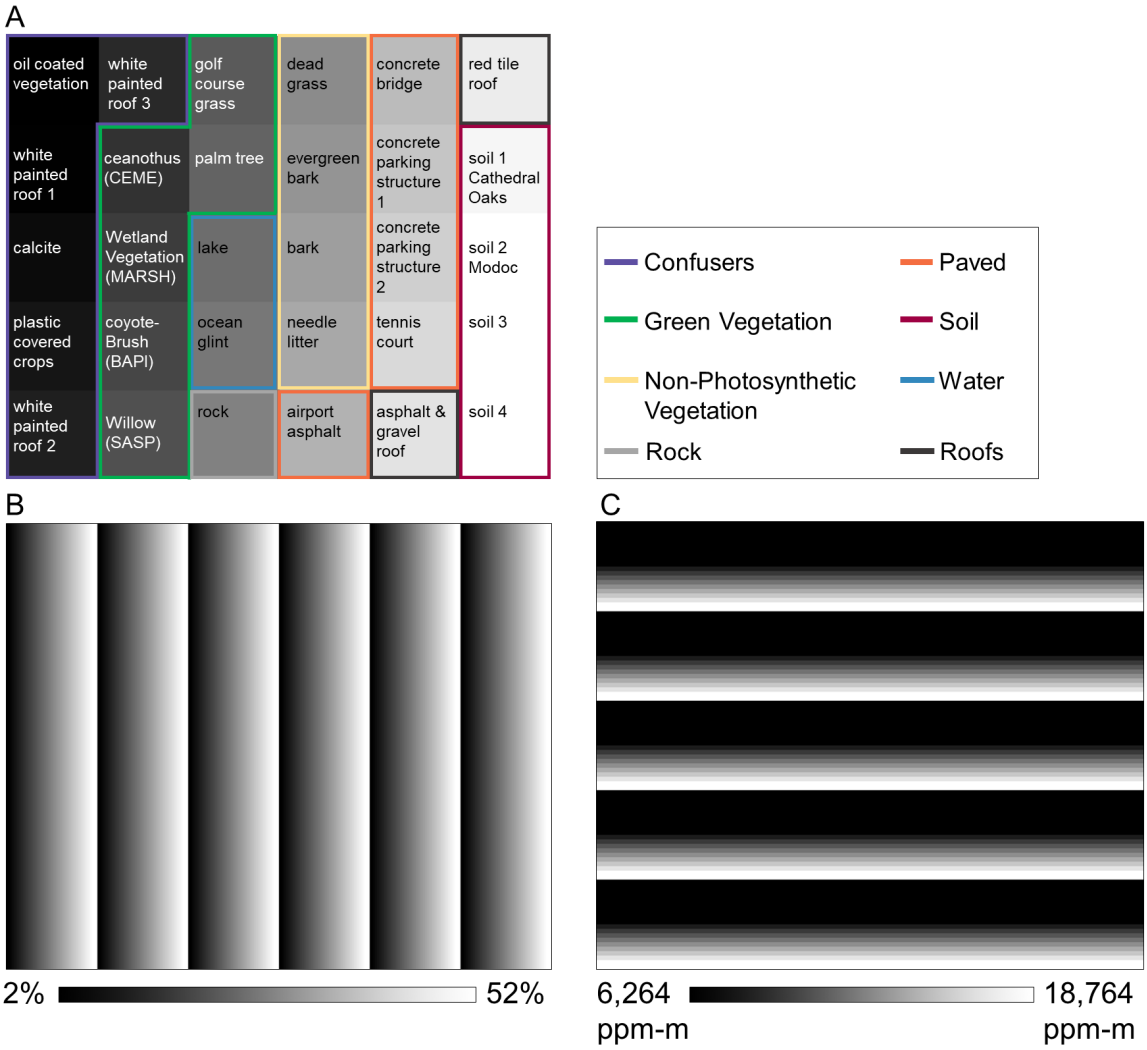


Figure 2.3: The organization of the synthetic image. A. The location of the surface types in the synthetic image. B. The modeled albedo levels for each background spectrum varied from 2 percent on the left to 52 percent on the right. C. The modeled methane concentrations in ppm-m for the atmosphere between 0 and 4 km.

2.3.2 The IMAP-DOAS Retrieval Algorithm

Based on the Beer-Lambert law, Differential Optical Absorption Spectroscopy (DOAS) describes the relationship between incident intensity for the vertical column and measured intensity after passing through a light path containing an absorber [66]. The IMAP-DOAS retrieval incorporates optimal estimation theory to adjust the column densities of gases until there is optimal agreement between the measured and modeled radiances [67] and has been modified for use with AVIRIS-NG [51]. For this study, IMAP-DOAS was setup to model reflected solar radiation using a two layer model. Above the aircraft, the vertical optical densities were combined with an air mass factor (AMF) calculated to account for one-way transmission. Below the aircraft, vertical optical densities were also combined and an AMF calculated to account for two-way transmission (Figure 2.2). Atmospheric profiles from the LOWTRAN/MODTRAN U.S. standard atmosphere [68] were updated to reflect background concentrations, including 1.864 ppm methane near the surface and volume mixing ratios (VMR) that decreased with altitude. These atmospheric profiles and spectral parameters for methane, water vapor, and nitrous oxide from the HITRAN database [12] were used to calculate vertical optical densities.

Methane retrievals were performed between 2215 and 2410 nm and included fits for the additional absorbing species of water vapor and nitrous oxide. The resulting state vector (x_n) has six entries (three gases for two atmospheric layers). Modeled radiance was calculated for each wavelength with a forward radiative transfer model using the following equation:

$$F^{hr}(x_i) = I_0^{hr} * exp(-\sum_{n=1}^{6} A_n * \tau_n^{ref} * x_{n,i}) * \sum_{i=0}^{k} a_k \lambda^k \tag{2.1}$$

Where $F^{hr}(x_i)$ is the forward modeled radiance (high spectral resolution) at the i-th iteration of the state vector, I_0^{hr} is the incident intensity (solar transmission spectrum), A_n is the AMF for each n number of atmospheric state vector elements (6 rows, specified for each of the 2 layers and repeated for each gas), τ_n^{ref} the reference total optical density for each n number

of atmospheric state vector elements (including optical densities of methane, water vapor, and nitrous oxide), $x_{n,i}$ is the gas related state vector at the i-th iteration (gas scaling factor), which scales the prior optical densities of methane, water vapor, and nitrous oxide in each n layer (6 rows). a_k are polynomial coefficients to account for broadband variability in surface albedo. The high resolution modeled radiance F^{hr} is then convolved with the instrument line shape and sampled to the center wavelengths of each AVIRIS-NG spectral band. This results in a low resolution modeled radiance at the i-th iteration of the state vector $F^{hr}(x_i)$), calculated using a known τ_n^{ref} scaled by $x_{n,i}$.

The IMAP-DOAS algorithm was run using the same parameters used to generate the synthetic image, including the sensor height, location, date, time, and solar zenith angle (Table 2.1). In this study, the IMAP-DOAS algorithm assumed background concentrations above the aircraft and perturbed the absorbing species in the lowest layer of the model (from 0 to 4 km). The resulting gas state vector for the lowest layer of the model at the last iteration (gas scaling factor) was then multiplied by the product of the VMR for the lowest layer of the reference atmosphere and the distance between the aircraft and the ground, resulting in gas concentrations in units of ppm-m. Therefore, IMAP-DOAS retrievals reflect the methane concentrations present in the atmospheric subcolumn beneath the aircraft (from 0 to 4 km). Additional details on the IMAP-DOAS retrieval can be found in Thorpe et al. (2014, 2017) [24, 51].

2.4 Results

2.4.1 Aerosol Scattering

We first tested the effects of aerosol scattering on the IMAP-DOAS results. We found that the differences between the modeled methane and IMAP-DOAS retrieved methane is much larger than the differences between the 5 and 30 km visibility (Figure 2.4), indicating that

more error is associated with surface type or albedo than visibility. Figure 2.4 shows that the distribution of the difference for 5 km and 30 km is very similar with a slight offset between the peaks, corresponding to a mean difference of 1559.9 ppm-m for the 5 km visibility and 1712.39 ppm-m for the 30 km visibility. In addition to the differences between the 5 and 30 km histograms being relatively minor, 5 km visibility is an extremely low visibility and in practice there would be smaller differences in retrieved concentrations across a more realistic range in visibilities.

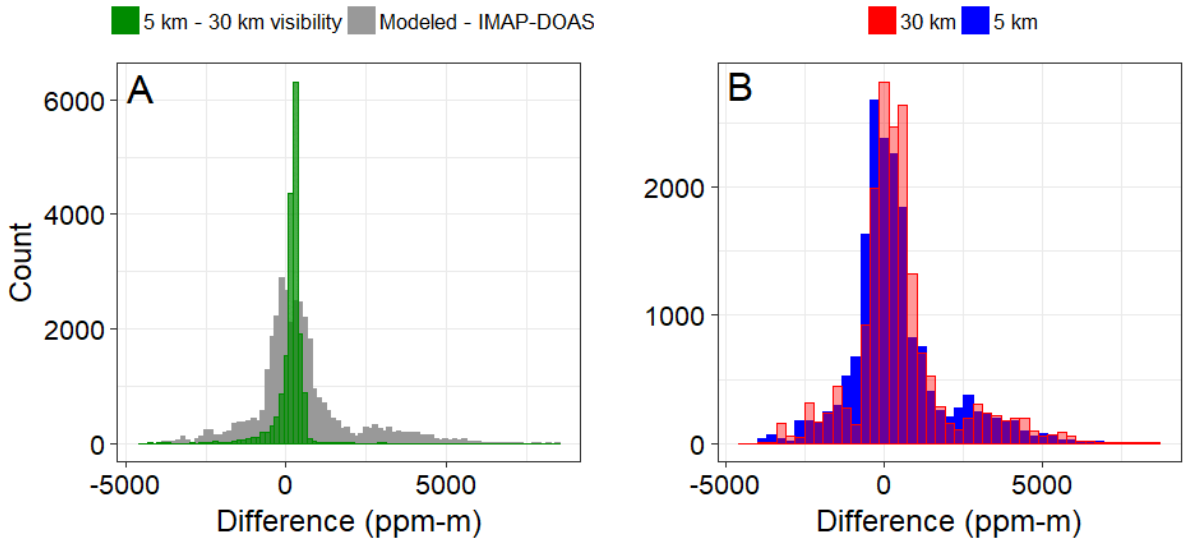


Figure 2.4: A) The green histogram shows the difference in the retrieved IMAP-DOAS results for the 5 km visibility and the 30 km visibility. The gray histogram is the difference between the methane modeled in the synthetic image and the methane retrieved by IMAP-DOAS for both visibilities. B) The blue histogram is the difference between the methane modeled in the synthetic image and the IMAP-DOAS results for the 5 km visibility atmosphere. The red histogram is the difference between the methane modeled in the synthetic image and the IMAP-DOAS results for the 30 km visibility atmosphere.

2.4.2 IMAP-DOAS

The IMAP-DOAS algorithm was successful in retrieving the modeled methane enhancement in the synthetic image (Figure 2.5). In addition, the pattern and values of retrieved

methane enhancement were consistent with the methane enhancement modeled in the synthetic image. Initial visual analysis indicates that the IMAP-DOAS retrieved methane concentration ranged from between 5,000 and 6,000 ppm-m and then gradually increased until it reached the 18,000 to 20,000 range (Figure 2.5). The most notable exception was the Hope Lake box (the box displayed white). This water spectrum had very low reflectance between 2,215 and 2,410 nm, resulting in no ability to retrieve or detect methane using IMAP-DOAS.

Figure 2.6 shows the correlation between the methane concentration from the synthetic image and the IMAP-DOAS retrieved concentrations for the entire image except pixels using the Hope Lake spectrum. The best fit trend was close to the 1:1 line, however IMAP-DOAS underestimated the modeled concentrations by an average error of 385.11 ± 1568.33 ppm-m (Table 2.3) and the RMSE for the entire image was 1614.92 ppm-m. These results incorporate all land cover types except the lake water and include confusers. The average RMSE dropped to 862.75 ppm-m and the average error dropped to an overestimate of 5.93 ± 862.73 ppm-m when the confuser and Hope Lake background spectra were excluded. When we organize the results by land cover class, it becomes clear that each class responds differently, and a few classes are primarily responsible for the spread in the data. Figure 2.7 plots the IMAP-DOAS results against the modeled methane for eight different land cover classes (rock is combined with the soils and lake water and sun glint are separated) and Table 2.3 summarizes the mean error for each land cover class. We found roofs, soil, NPV, and sun glint all had good agreement and low spread (Figure 2.7, Table 2.3). The lake water, green vegetation, and confusers all had relatively poor agreement and larger spread (Figure 2.7, Table 2.3).

Table 2.3: The mean error between the synthetic image and retrieved IMAP-DOAS methane concentrations. The mean error is the average of the residuals between the known methane concentrations from the synthetic image and IMAP-DOAS retrieved methane concentrations (negative means are overestimations and positive means are underestimations).

Land cover class	**Mean Error ppm-m**
Confusers	1884.10 ± 2490.45
Paved	-243.92 ± 382.39
GV	-62.51 ± 1466.72
Soil	372.45 ± 307.40
Lake Water(Hope Lake)	-32757.44 ± 16661.133
NPV	22.44 ± 462.67
Sun Glint	645.49 ± 310.57
Roofs	-168.62 ± 428.8
All (except Hope Lake)	385.11 ± 1568.33
All (except Hope Lkae and Confusers)	-5.93 ± 862.73

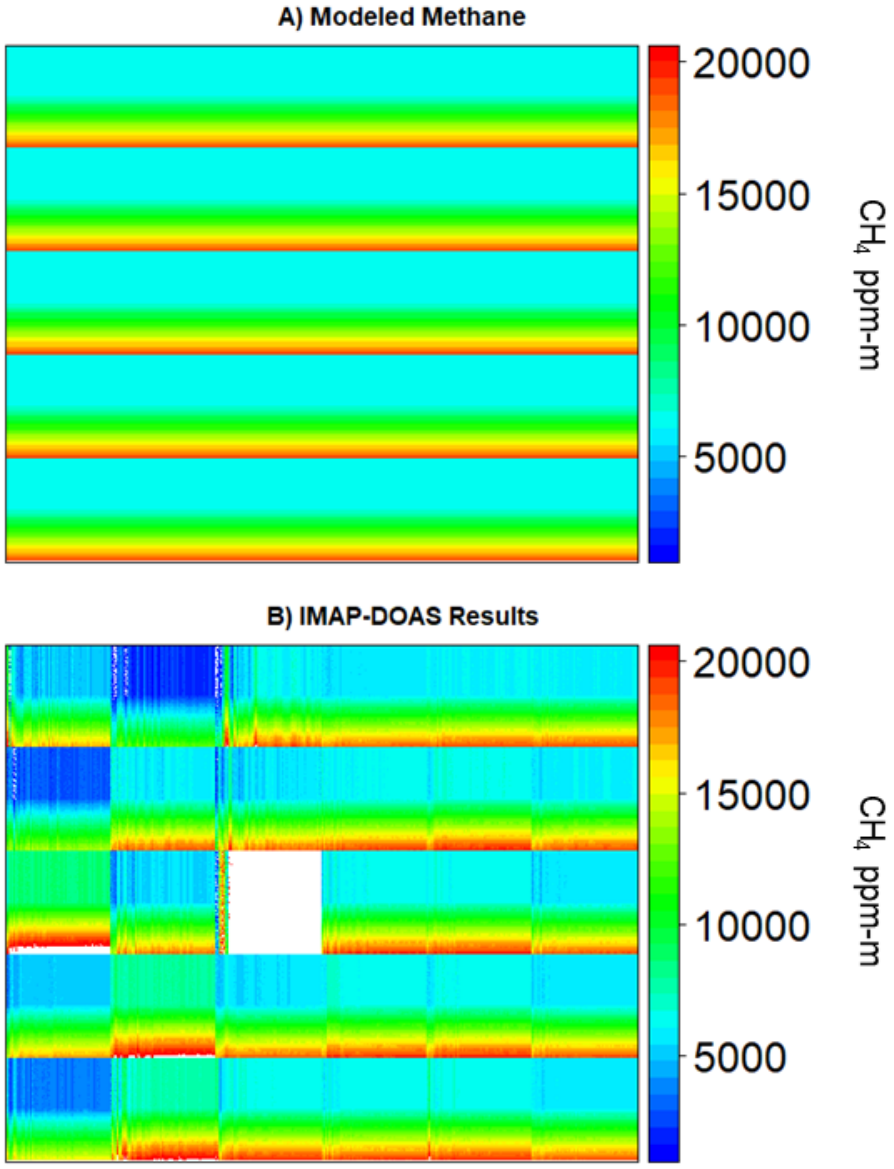


Figure 2.5: A) The methane concentration in ppm-m modeled by A) MODTRAN, and B) retrieved by IMAP-DOAS. Scaling in the two plots is the same, with results outside of the displayed range shown in white. See Figure 2.3 for the configuration of the synthetic image.

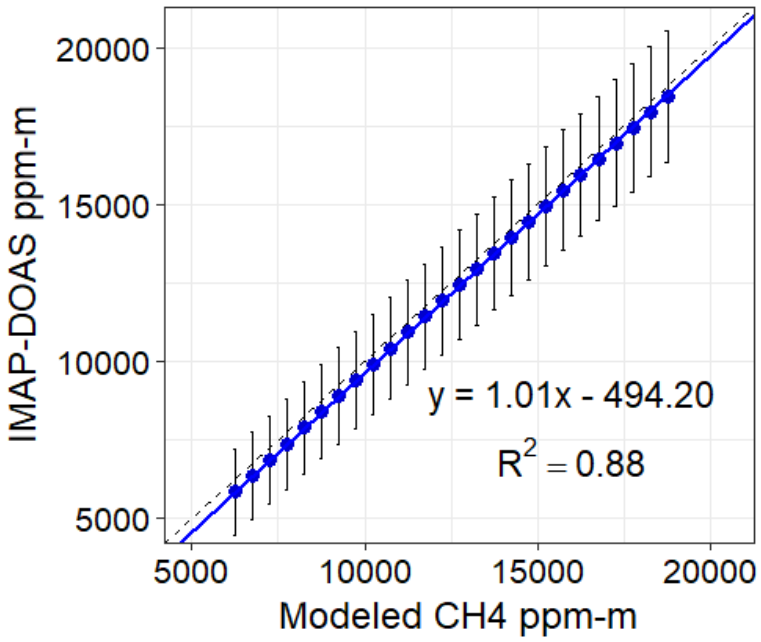


Figure 2.6: The mean IMAP-DOAS retrieved concentration for each synthetic image concentration, plotted against the image concentration for all pixels except Hope Lake. The error bars represent one standard deviation. The dotted line represents the one to one line and the blue solid line is the linear fit. The linear model has a slope of 1.01, an intercept of -494.2, and an R-squared of 0.88.

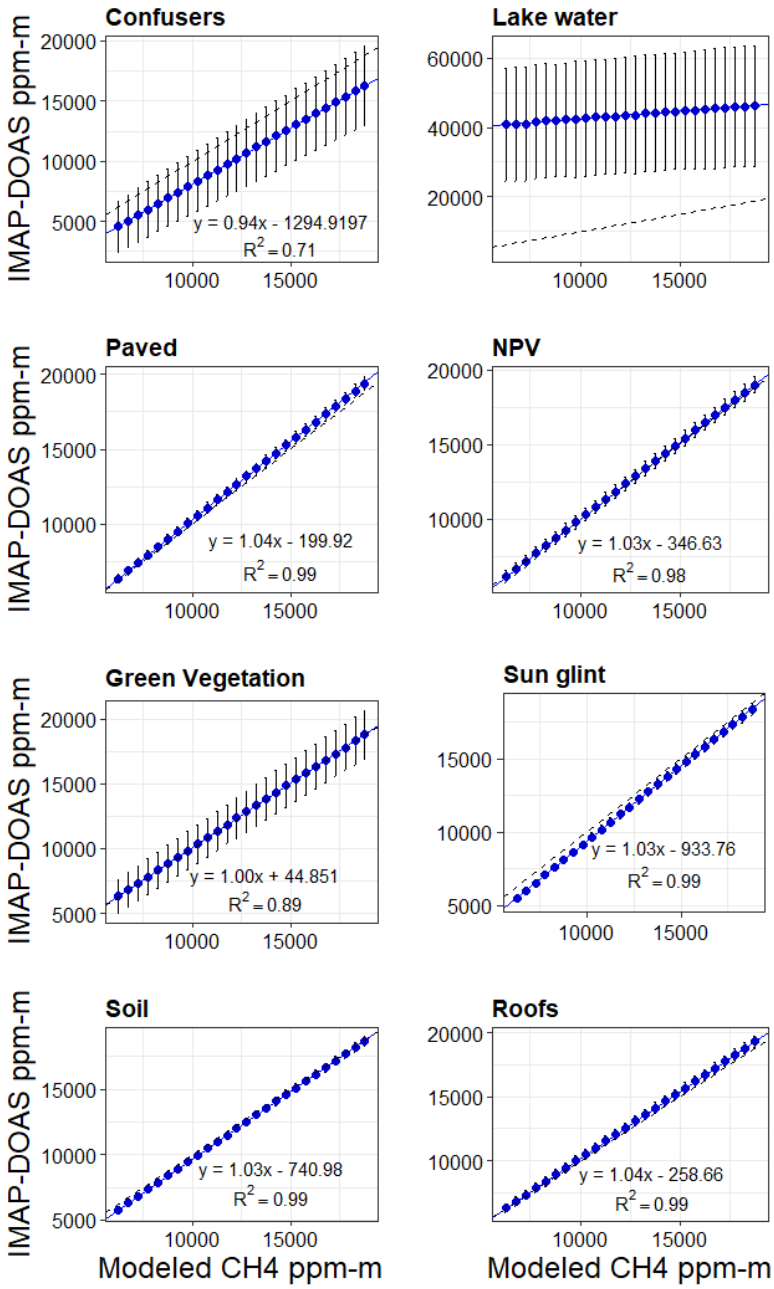


Figure 2.7: The mean IMAP-DOAS retrieved concentration for each synthetic image concentration, plotted against the image concentration within each land cover class. The error bars represent one standard deviation from the mean. The dashed line represents a one-to-one relationship and the blue line is the linear regression. The slope, intercept, and r-squared for the linear model are reported for each plot except lake water.

2.4.3 Surface Type

In addition to looking at the correlation between IMAP-DOAS retrieved concentration and synthetic image concentration, we also looked at the per-pixel error. Figure 2.8 shows the error between IMAP-DOAS retrieved and synthetic image concentrations (synthetic image minus IMAP-DOAS). In total, 90 percent of the error (excluding Hope Lake) fell between -1941.65 and 3793.06 ppm-m. Excluding the confusers as well, the 90 Percent range decreased from the afore mentioned range to -1609.96 ppm-m to 998.36 ppm-m. We observed a few distinct patterns in error (Figure 2.8 and 2.9). First, the error seems to be related to individual surface types because different background spectra boxes have distinctive error patterns. Some surface types (Lake water, white painted roofs, and calcite) exhibited a large degree of error, with error increasing with methane concentration. A number of other surfaces also exhibited heteroscedastic errors, with the error tending towards overestimation with increasing methane.

In order to summarize the pattern of error, we averaged the residuals and calculated the root mean square error (RMSE) for each background spectrum (Table 2.4). In addition, we plotted the error for each background spectrum as box plots (Figure 2.9). The Hope Lake (water), the white painted roofs, calcite, coyote brush, and golf course grass had high mean errors and had the largest RMSE. The remaining GV and confuser surfaces also had high RMSE. The soils, the paved surfaces, NPV, and roofs were the surfaces with lower mean error and lower RMSE.

Apart from the patterns associated with surface type, the results shown in Figure 2.8 exhibit two characteristic error patterns: the residuals scale with the methane concentration and the results indicate slight vertical banding. We observed a greater overestimate at higher methane concentrations and underestimation at low methane concentrations. These relationships between the error and the modeled methane may be due partly to the difference in how MODTRAN and IMAP-DOAS model radiance. MODTRAN accounts for multiple scattering while IMAP-DOAS does not. This means the path radiance for MODTRAN is larger than for IMAP-

DOAS, and therefore an equivalent methane concentration will have a more pronounced absorption feature [15], which is consistent with the observed IMAP-DOAS overestimates. Additionally, varying degrees of vertical banding are observed in Figure 2.8. The banding results from the combined effects of the layout of the albedos in the synthetic image and the retrieval fit errors. For example, two adjacent pixels with the same concentration of modeled methane, the same surface, but with a 1 percent albedo difference (Figure 2.3) can result in differing retrieved methane concentrations. This effect is more pronounced for certain surface types like confusers and green vegetation and less visible for bright surfaces such as soils and paved surfaces.

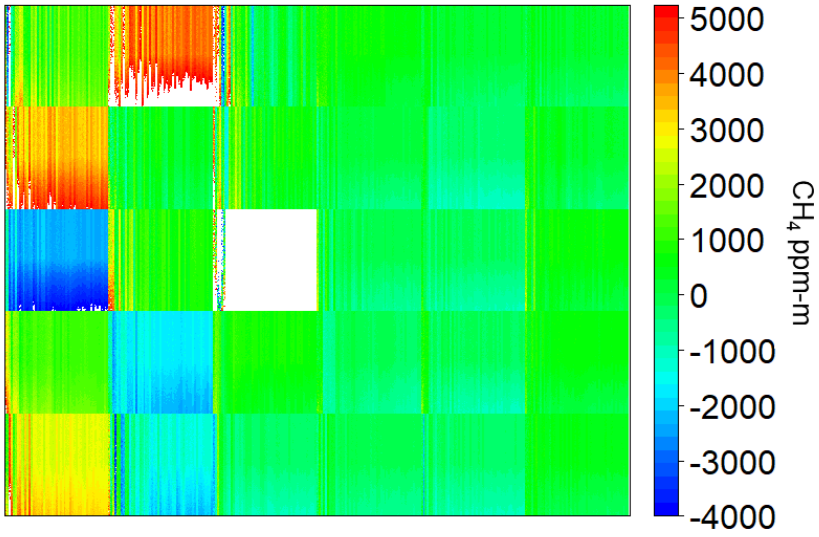


Figure 2.8: The error between the synthetic image and IMAP-DOAS retrieved methane concentrations (image minus IMAP-DOAS). The white areas represents values outside of the displayed range. The all white box is lake water and the partially white box is one of the white painted roofs. See Figure 2.3 for the complete configuration of the synthetic image.

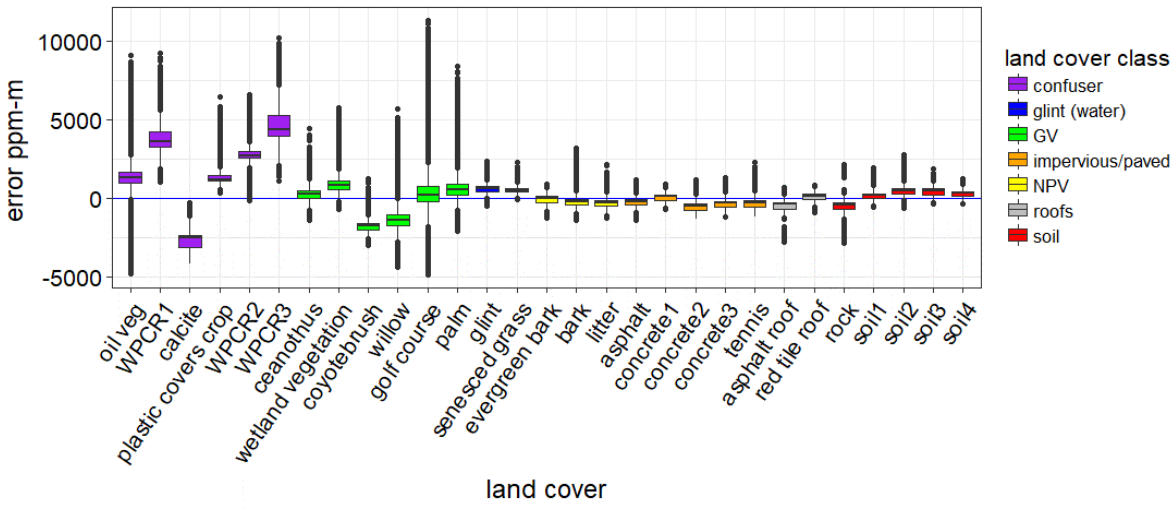


Figure 2.9: Box plots of the error for every surface type. The colors, as indicated in the legend, represent the larger land cover class. Lake water is omitted.

Table 2.4: Table showing the surface name, the mean error, and root mean square error (RMSE). The surface types are organized by RMSE.

Surface Type	**Mean Error ppm-m**	**RMSE**
Hope Lake	-32757.44	36750.73
WPCR3	4632.82	4748.20
WPCR1	3799.22	3890.20
WPCR2	2759.16	2826.87
Calcite	-2647.97	2728.81
Golf course grass	602.23	1996.17
Coyote brush (BAPI)	-1754.34	1793.47
Oil coated vegetation	1381.89	1791.71
Willow (SASP)	-1203.39	1558.20
Plastic covered crops	1379.49	
Wetland Vegetation (MARSH)	998.93	1262.71
Palm tree	689.21	1193.34
Ocean water (Glint)	645.5	716.32
Rock	-429.51	657.00
Concrete parking stucture 1	-488.67	608.21
Soil 4	516.57	606.86
Dead grass	545.54	593.19
Asphalt and gravel roof	-464.08	591.98
Ceanothus (CEME)	292.32	532.02
Soil 1	454.77	518.77
Tennis court	-283.93	507.79
Bark	-139.65	491.13
Concrete parking structure 2	-338.11	449.42
Needle litter	-274.18	430.17
Soil 2	318.41	393.68
Soil 3	200.05	374.79
Airport asphalt	-196.72	360.06
Evergreen bark	-41.94	283.02
Red tile roof	126.83	272.32
Concrete bridge	87.84	363.07

2.4.4 Albedo

We also evaluated the effect of albedo on retrievals. To determine the albedo of a spectrum we used the radiance value at 2139 nm. The radiance at this wavelength is a good indicator of albedo because there are no atmospheric absorptions from any of the major greenhouse gases[15]. In addition, 2139 nm is in the SWIR, which means the radiance values represent the albedo in the region of the electromagnetic spectrum of interest. To test the influence of albedo on the IMAP-DOAS retrieved concentration, the residuals were binned by radiance level and then plotted as box plots (Figure 2.10). The lowest radiance bin, with values ranging between 0 and 0.104 μWcm^{-2}nm^{-1}sr^{-1} at 2139 nm, had the largest spread in the residuals and the poorer results. The pixels with radiance between 0.206 and 0.611 μWcm^{-2}nm^{-1}sr^{-1} at 2139 nm had a much smaller range of residuals compared to the darkest pixels but still exhibited some spread. The pixels above 0.611 μWcm^{-2}nm^{-1}sr^{-1} had the least spread and the most accurate results. Lastly, the outlying residuals around and below 5000 and -2500 ppm-m, can all be attributed to the confusers.

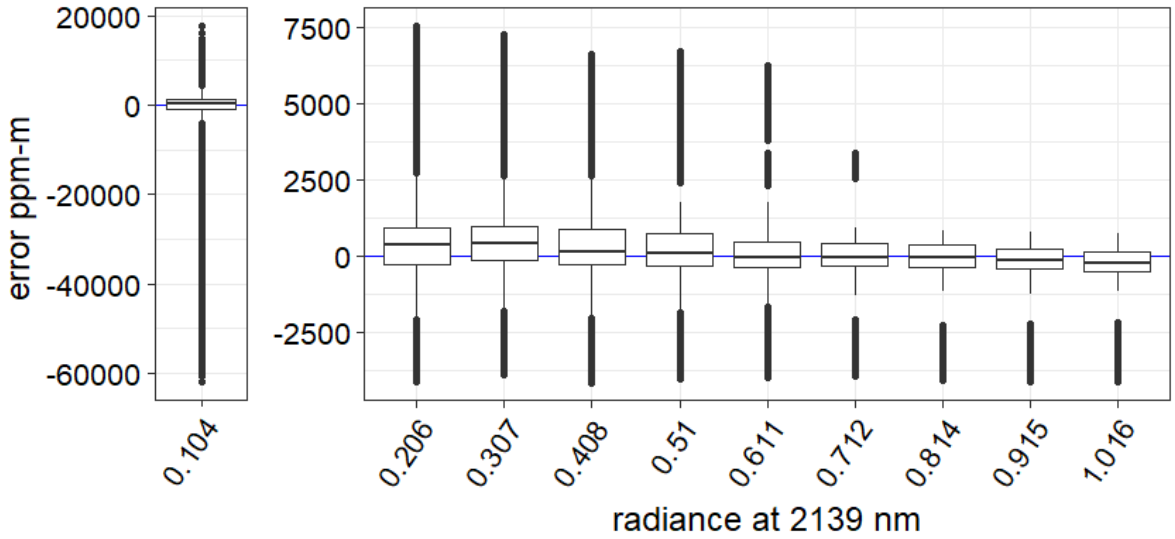


Figure 2.10: The residuals between the image and IMAP-DOAS retrieved concentration (image minus IMAP-DOAS) binned by radiance at 2139nm (μWcm^{-2}nm^{-1}sr^{-1}) and then plotted as box plots. The x-axis represents the upper level of the radiance threshold used to bin the residuals. The plot on the left has a different y-axis to accommodate the larger range in error.

2.5 Discussion

Surface type and albedo both have an effect on the methane retrieval results for the synthetic image. By isolating and quantifying the effect of different surface types, we can better understand detection limits and potential error sources of methane concentration retrievals. We found that soils, paved surfaces, roofs, and NPV generally possess high reflectance and no confusing absorption features in the SWIR and resulted in good methane retrievals. Low reflectance materials (water, green vegetation) and materials with confusing absorption features (confusers) produced large uncertainties for methane retrievals. In the following sections, we will discuss the surfaces and albedos that caused poor retrieval results, reasons for the poor results, and possible solutions.

2.5.1 Albedo

Albedo has a significant effect on the accuracy of the results but only for the lowest albedos. We found that surfaces (independent of surface type) with very low radiance, below 0.10 μWcm^{-2}nm^{-1}sr^{-1} at 2139 nm, had extremely poor results with large error. This finding is consistent with Thorpe et al. (2017)[51] who found that dark surfaces resulted in anomalously high retrievals and removed spectra if there were radiance values less than 0.01 μWcm^{-2}nm^{-1}sr^{-1} at any band in the fitting window. Zhang et al. (2017) [55] also examined the effects of many factors, including albedo, on a different retrieval technique and concluded that albedo was a significant factor in determining the bias of the methane concentration retrieval. In contrast, we found that the impact of albedo on retrieval accuracy was small, except at the lowest albedos. We found no linear correlation between albedo and error. For the darkest surfaces (0.10 μWcm^{-2}nm^{-1}sr^{-1} and below), there is insufficient reflected radiance to discern methane absorptions. Surfaces that fell between 0.10 and 0.60 μWcm^{-2}nm^{-1}sr^{-1}1 at 2139 nm had a detectable methane signature but the error in the results was higher than for brighter surfaces. For pixels with radiance above 0.60 μWcm^{-2}nm^{-1}sr^{-1}1 at 2139 nm the range in the residuals was much lower and the column concentrations in this range are fairly accurate. In addition, all outlying error in Figure 2.10 is attributed to the confusers. Although albedo affects the accuracy of the column concentration, the effect is far less significant than described in Zhang et al. (2017) [55]. In addition, although column concentration accuracy may be poor at low albedos, detection is still possible at all radiance values save for the lowest. As shown in Figure 2.5 and 2.7, methane retrieval accuracy is poor for the dark lake water example however water with sunglint results in high retrieval accuracy.

2.5.2 Surface Type

Previous studies that tested the IMAP-DOAS retrieval technique on AVIRIS Classic imagery concluded that the results were also influenced by the underlying surface [24]. Different surface types can affect the accuracy of the IMAP-DOAS results either through the spectral shape of the material in the SWIR or with their inherent albedo. To explore this idea further and to better understand the error associated with surface type we looked at the spectral shape of the reflectance data in the SWIR. Figure 2.11 shows the four spectra with worst accuracy, the four spectra best accuracy (accuracy is defined by the RMSE as reported in Table 2.4), and a GV spectrum.

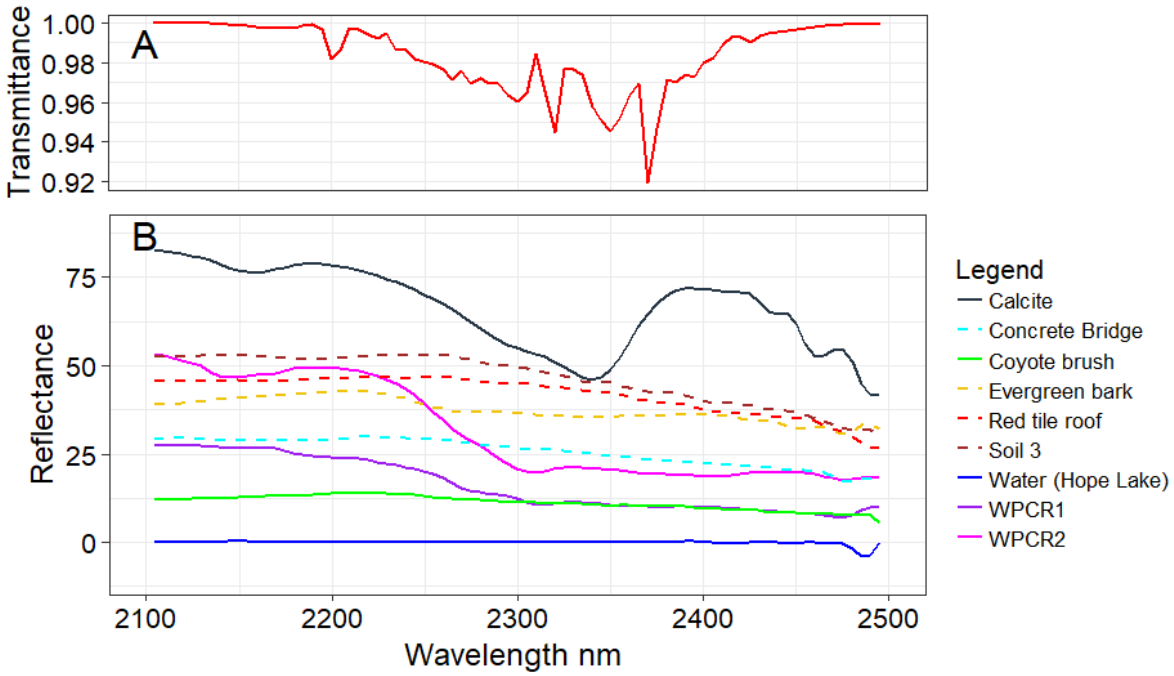


Figure 2.11: A) The transmittance spectra for methane calculated from MODTRAN and convolved to the AVIRIS-NG bandpass function. B) The reflectance spectra in the SWIR (2100 nm to 2500 nm) for calcite, water, the white painted roofs, soil, evergreen bark, red tile roof, coyote brush, and concrete. The solid lines represent surface types that had high amounts of error. The dashed lines represent surface types that had the lowest amount of error.

Green Vegetation

Thorpe et al. (2014) noted that retrieval performance was poorer for areas dominated by green vegetation compared to areas dominated by soil. Green vegetation spectra, especially the golf course grass and coyote brush, are generally very dark in the SWIR (Figure 2.11), which was the main cause of the error. Green vegetation is not as dark as water and therefore the results are far better for green vegetation than for water. In addition, despite green vegetation having little reflectance in the SWIR, the spectral shape is relatively flat which causes improved results compared to the confuser class. Green vegetation is a very common surface type especially in natural and agricultural landscapes and therefore can make accurate quantification of methane plumes in these areas more challenging. However, green vegetation in AVIRIS-NG images can easily be classified and an estimate of uncertainty applied. In addition, future sensors with finer spectral resolution and improved gas sensitivity should have improved accuracy over vegetation [62]. Lastly, although IMAP-DOAS results have some uncertainly, methane detection remains possible over vegetated surfaces.

Confusers

The confusers had large mean error and RMSE. After lake water, the confuser class had the most error with the worst results attributed to the white painted roofs and calcite. These surfaces, although bright in the visible portion of the spectrum and part of the SWIR, have significant drops in reflectance in the methane absorption bands. In the case of the white painted roofs, the SWIR absorption is due to hydrocarbon absorptions from oil-based paints. In the case of calcite, this feature is due to the vibrational absorption bands found in carbonate minerals [69]. These absorption features are thought to be the cause of the poor results. Other studies have also found that surfaces with strong absorption features between 2200 and 2400 nm can cause error. Thorpe (2013) [22] used a cluster-tuned matched filter to detect methane in

various AVIRIS Classic scenes concluding that surfaces with hydrocarbon absorptions or any significant absorptions in the 2200 to 2500 nm window were likely to confuse the matched filter and result in a spurious signal. Our study specifically tested these types of surfaces and found that they caused error in IMAP-DOAS concentration retrieval as well but not necessarily a spurious signal. Interestingly, these surfaces did not all cause an overestimation in the methane concentration as would be expected. Of the four surfaces with the most pronounced absorptions in the 2300 nm window, only calcite caused overestimations and the other surfaces (white painted roofs 1, 2, and 3) caused underestimations. Figure 2.11 shows the spectra of calcite, white painted roof 1, and white painted roof 2. The calcite is much brighter and has a more prominent absorption versus the other white painted roofs. White painted roof 2 also has a clear absorption feature but does not have overestimation. The other white roofs, the oil coated vegetation, and the plastic covered crops also had very poor results but the cause of the error for these surfaces was due to low reflectance in the SWIR. These types of surfaces, especially the white painted roofs, are common in urban and commercial areas and can pose challenges when detecting methane plumes in these types of environments. Similar to green vegetation, these surfaces can be classified and masked out of images so as not to cause spurious signals or inaccurate results.

Water

The largest source of error in the IMAP-DOAS results was Hope Lake. In general, water has extremely low reflectance in the SWIR (Figure 2.11) and this is the source of the error in the results. Given the low reflectance over water bodies, mapping methane sources over water bodies with AVIRIS-NG will remain challenging. Despite this, methane plumes originating from water bodies, like manure lagoons and wastewater treatment plants, will still offer opportunities for plume detection and quantification as the plume moves over background surfaces with higher reflectance (Figure 2.12). For larger water bodies, sun glint reflected off the surface

of the water can provide an excellent means of detection [19, 15, 24]. In addition, this study concluded that results from sun glint are fairly accurate. On a global scale, wetlands are the largest natural source of atmospheric methane and are predicted to become a more important source in the future [70, 55]. This study suggests that methane detection should be possible for wetlands covered in vegetation.

2.5.3 Comparison to Real AVIRIS-NG Images

These patterns are consistent with previous studies and results from IMAP-DOAS applied to real AVIRIS-NG images (Figure 2.12). In Figure 2.12, IMAP-DOAS methane retrievals are shown for a dairy and a coal mine ventilation shaft imaged by 2015 AVIRIS-NG flights over Bakersfield, California and the Four Corners region of the United States respectively. In both of these images, there are clear examples of the underlying surface reflectance affecting the methane retrievals. In Figure 2.12 the methane plume emanates from the waste lagoons and extends southeast over the combination of buildings with metal roofs, soils, and green vegetation shown in Figure 2.12. The plume is most visible over the soil and roof but seems to disappear over the green vegetation due to difficulty in detecting methane over vegetation. The plume is more visible over the metallic roofs and less visible over low albedo shaded areas between the buildings. In addition, it appears that there is no methane directly over the dairy waste lagoons, due to the difficulty of methane retrieval over water. The image of a coal mine ventilation shaft (Figure 2.12) has a much larger methane plume (Figure 2.12), and the plume is clearer in this image compared to the dairy waste lagoon example. The majority of the surfaces in this image are soil, NPV, and paved surfaces, all surfaces that are ideal for retrieving methane. The one exception is the pond; the plume seems to disappear as it passes over the water due to very low radiance. The same surfaces in these images and the synthetic images cause poor detection, providing assurance that the synthetic image is

accurately capturing patterns found in real imagery.

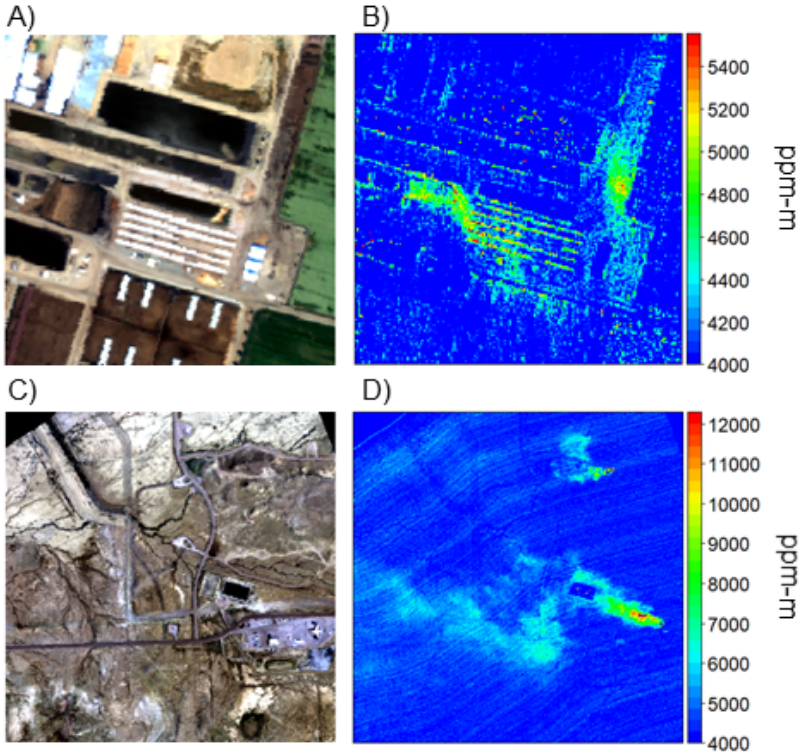


Figure 2.12: A) True color AVIRIS-NG image of a dairy in Bakersfield. CA April 29, 2015. The sensors height was 2.9 km resulting in a 2.6 m pixel. B) IMAP-DOAS methane retrieval for image A shows methane plumes emanating from dairy waste lagoons. C) True color AVIRIS-NG image of coal mine ventilation shafts near the Four Corners region of the United States from April 22, 2015. The sensor height was 2.9 km resulting in a 2.7 m pixel. D) IMAP-DOAS methane retrieval for image C shows methane plumes that originate from known coal mine ventilation shafts. For all scenes north is up.

2.5.4 Limitation and Potential Solutions

While this study provided an opportunity to control and test the effect of the surface properties on methane quantification, there are some limitation to this study. As mentioned previously and illustrated in Figure 2.8, there was not perfect agreement between the retrieved IMAP-DOAS methane concentrations and the known concentrations from the synthetic scene. As expected, some of this was due to the underlying surface, however, some patterns in the

error were unexpected and likely due to differences in the radiative transfer calculations used in IMAP-DOAS and MODTRAN. The most notable error in the image is the slight overestimation of methane at higher concentrations. We believe this can be partly attributed to the fact that MODTRAN incorporates multiple scattering while IMAP-DOAS does not. To investigate this possibility, we ran MODTRAN without the multiple scattering component, created a small synthetic image, and ran IMAP-DOAS. We found that the overestimation decreased but not enough to explain all of the error in the results. This study primarily focused on the effect of the surface on methane detection but also determined that aerosols have a minimal influence on methane retrievals. Despite these limitations, the synthetic image remains a powerful tool to study the sensitivities of surface type and other factors on detection.

This study found that some surface types can influence the accuracy of the IMAP-DOAS results. A potential solution to account for the influence of land cover is to classify the underlying surface. In addition to the SWIR, AVIRIS-NG collects data in the visible and near infrared portion of the spectrum. This additional information can be used to classify the underlying land cover and a measure of error could be applied to each class. This could be done for classes such as vegetation and soil or for albedo classes. Additionally, a higher spectral resolution sensor will reduce sensitivity to land cover type. AVIRIS-NG has a 5 nm spectral resolution, which is well suited for mapping land cover and other surface properties. However, at 1 nm spectral resolution the spectral signatures of gases are more pronounced and have higher frequency variations compared to the surface, which should decouple the spectral signature of the atmosphere from the surface [62]. A 1 nm instrument specifically designed for gas mapping will provide increased gas sensitivity [62, 27] and its performance could be tested empirically using a similar sensitivity study.

2.6 Conclusions

The synthetic AVIRIS-NG image provided an excellent framework through which we were able to test the effects of land cover and albedo on methane retrievals with the IMAP-DOAS algorithm. The synthetic image allowed us to model known methane concentrations, albedo, land cover, and other atmospheric variables. By quantifying the effects of the surface on methane retrievals, we were able to characterize the sensitivity of the IMAP-DOAS algorithm applied to AVIRIS-NG data. Overall, we found excellent agreement with the modeled methane and the IMAP-DOAS results. We found that the most accurate retrievals were over soils and paved surfaces. Conversely, we found that low albedos, below 0.10 μWcm^{-2}nm^{-1}sr^{-1} at 2139 nm, caused higher error in the retrieval results but above that threshold, there was significantly less error. Green vegetation had high error due to low albedo in the SWIR. Water, the darkest surface, had the most error. Confusers also had higher error due to the absorption features in the 2200-2400 nm window but not all caused a spurious signal as hypothesized. Changes in the surface can affect our ability to retrieve column concentration accurately. This means that methane plumes over water bodies will present a greater challenge and require further study and attention. Potential solutions to dealing with these challenging surfaces include using other regions of the electromagnetic spectrum to classify then flag or mask out these surfaces. Finer spectral resolution provided by future imaging spectrometers will provide greater gas sensitivity as well. The synthetic image has strength in its versatility and therefore can be modified to test the sensitivity of these future sensors or other retrieval algorithms, gas species, and land cover. Overall, the results from this study help us to understand the capabilities of the AVIRIS-NG sensor for methane retrievals and aid in understanding the limitations and uncertainty in mapping methane over large regions with variable surface types

Chapter 3

Methane Mapping with Future Satellite Imaging Spectrometers

With Philip E Dennison, Marcus Foote, Andrew K Thorpe, Sarang Joshi, Robert O Green, Riley M Duren, David R Thompson, and Dar A Roberts

This chapter is based off a manuscript published in the journal of Remote Sensing:

Ayasse, A.K.; Dennison, P.E.; Foote, M.; Thorpe, A.K.; Joshi, S.; Green, R.O.; Duren, R.M.; Thompson, D.R.; Roberts, D.A. Methane mapping with future satellite imaging spectrometers. Remote Sens. 2019, 11, doi:10.3390/rs11243054.

3.1 Abstract

This study evaluates a new generation of satellite imaging spectrometers to measure point source methane emissions from anthropogenic sources. We used the Airborne Visible and Infrared Imaging Spectrometer Next Generation(AVIRIS-NG) images with known methane plumes to create two simulated satellite products. One simulation had a 30 m spatial resolution with 200 Signal-to-Noise Ratio (SNR) in the Shortwave Infrared (SWIR) and the other had a 60 m spatial resolution with 400 SNR in the SWIR; both products had a 7.5 nm spectral spacing. We applied a linear matched filter with a sparsity prior and an albedo correction to detect and quantify the methane emission in the original AVIRIS-NG images and in both satellite simulations. We also calculated an emission flux for all images. We found that all methane plumes were detectable in all satellite simulations. The flux calculations for the simulated satellite images correlated well with the calculated flux for the original AVIRIS-NG images. We also found that coarsening spatial resolution had the largest impact on the sensitivity of the results. These results suggest that methane detection and quantification of point sources will be possible with the next generation of satellite imaging spectrometers.

3.2 Introduction

Methane is a prominent greenhouse gas and is responsible for about 20 percent of all atmospheric radiative forcing [32, 71]. As our planet continues to warm due to radiative forcing caused by greenhouse gases, understanding, monitoring, and reducing these emissions will become increasingly important. However, there remains a high level of uncertainty regarding the magnitude of methane sources and sinks globally [2, 71]. Anthropogenic sources, which make up 50–65 percent of all methane emissions, mostly come from the energy, waste, and agriculture sectors [72, 71]. These are generally point sources, or emissions emanating from a single

easily identifiable source like a gas storage tank or a landfill [25, 73]. Although these sectors can also contain diffuse sources, or emissions coming from a larger area, a few point sources can dominate the emissions budget. Identifying emission sources and quantifying their rates can improve regional greenhouse gas budgets and mitigation strategies [25, 27].

This study investigates the potential to use a future generation of Earth observing satellites to map methane emissions. Past and present satellite missions measure atmospheric methane, but lack the fine spatial resolution needed to measure individual point sources. These sensors, such as the Atmospheric Infrared Sounder (AIRS), SCanning Imaging Absorption SpectroMeter for Atmospheric CHartographY (SCIAMACHY), TROPOspheric Monitoring Instrument (TROPOMI), and the Greenhouse gas Observing Satellite (GOSAT), can accurately characterize the global and regional distributions of methane, but only at spatial resolutions between 7 and 60 km [18, 74, 67, 39, 75]. More recently, GHGsat demonstrated the ability to map methane plumes at a resolution as fine as 50 m [76, 30]. Future satellites may be able to detect methane at even finer spatial resolutions.

In the coming decade, there is strong interest in a new generation of Earth observing satellites equipped with Visible and Shortwave Infrared (VSWIR) imaging spectrometers[77]. VSWIR imaging spectrometers typically measure between 380 and about 2500 nm with between 5 to 10 nm spectral spacing [25, 15, 22, 51, 50]. These imaging spectrometers are sensitive to gas absorption features, which allows for the detection and quantitative mapping of methane, carbon dioxide, and water vapor [15, 19, 53, 20]. In 2019, the Italian space agency launched the Hyperspectral Precursor and Application Mission (PRISMA), a medium resolution imaging spectrometer [78, 79]. In 2020, the German space agency plans to launch the Environmental Mapping and Analysis Program (EnMAP) [80] and the Japanese government plans to launch the Hyperspectral Imager Suite (HISUI) [81], both of which are spaceborne imaging spectrometers.The National Aeronautics and Space Administration (NASA) plans to launch the Earth Surface Mineral Dust Source Investigation (EMIT) to the International Space

Station (ISS) in 2021. NASA's Surface Biology and Geology investigation is likely to include an imaging spectrometer that could launch as early as 2025 [82]. None of these sensors are being designed for gas mapping, but if these instruments can be used for methane mapping, the global monitoring of greenhouse gases will drastically improve.

Recent work with a current satellite VSWIR imaging spectrometer and airborne imaging spectrometer data have provided a testbed for evaluating point source methane detection and measurements with these types of instruments [15, 19, 20, 26, 51]. The Hyperion imaging spectrometer on board the EO-1 satellite successfully detected the accidental methane release at Aliso Canyon [26], despite the age of the sensor and low signal-to-noise ratio (SNR). The Airborne Visible and Infrared Imaging Spectrometer Next Generation instrument (AVIRIS-NG), detected, geolocated, and quantified over 500 methane point sources throughout California from the oil and gas, manure management, and waste management sectors [27]. Across each sector, a small number of point sources contributed the majority of observed methane emissions, demonstrating the importance of observing point sources.

While none of the proposed future imaging spectrometers are explicitly designed to map greenhouse gases, given their design and the prior successful work using similar airborne sensors to map methane, the upcoming generation of spaceborne imaging spectrometers has great potential for global mapping of near-surface methane emissions. This study examines the possibility of using these future sensors to monitor emissions from three of the largest anthropogenic methane sectors: oil/gas, waste management, and agriculture.

3.3 Methods

In order to test the capability of future sensors for methane mapping, we resampled AVIRIS-NG data to create a simulated satellite product (Figure 3.1) and then tested methane retrievals using this new product. We based our simulated satellite data on the sensor design for the

upcoming EMIT mission [83]. The EMIT sensor design favors radiometric sensitivity over spatial resolution, leading to a 60 m spatial sampling that is slightly coarser than the 30 m spatial sampling slated for many orbital VSWIR sensors. Therefore, we simulated two sensor designs. The first was characteristic of a hypothetical future NASA mission modeled after EMIT as well as those already operating or planned for launch by other space agencies. It has a 30 m spatial resolution with lower SNR. The second was a direct analogue of the EMIT instrument, with a 60 m spatial resolution and a higher SNR. Both simulations are important for understanding the methane mapping potential for NASA's future generation of sensors. The following section describes the original AVIRIS-NG data used, the process to resample it to a simulated satellite product, and the methane retrieval algorithm.

3.3.1 Imagery

AVIRIS-NG is an airborne imaging spectrometer that measures radiance in the visible through shortwave-infrared (SWIR). It measures in the spectral range from about 380 to 2500 nm with a 5 nm spectral sampling [8, 11, 84]. AVIRIS-NG has a 36 degree field of view and a one milliradian instantaneous field-of-view that results in spatial resolutions ranging between approximately 1 and 8 meters, depending on the height of the aircraft. The AVIRIS-NG data used in this study were collected in 2016 and 2017 throughout California as part of the California Methane Survey and an image from a 2018 controlled release experiment [27]. We selected images of plumes from a landfill, a dairy, a dairy digester, a wastewater treatment facility, and oil/gas infrastructure. In this study, eight examples of plumes (Table 3.1), one or more from each source, were resampled to satellite specifications using the methods described below.

Table 3.1: The Airborne Visible and Infrared Imaging Spectrometers Next Generation (AVIRIS-NG) flight lines used in this study. The methane source type, time, date, and spatial resolution of each flight line.).

Line Name	Source Type	Date of Flight	Time of Flight (UTC)	Spatial Resolution
ang20161104t183025	Gas Storage Facility	11/4/2016	18:30:25	1.6 m
ang20160915t185210	Gas Distribution Line	9/15/2016	18:52:10	1.7 m
ang20170618t194516	Landfill	6/18/2017	19:45:16	3.3 m
ang20170918t201542	Well	9/18/2017	20:15:42	3.3 m
ang20170618t193955	Wastewater Treatment	6/18/2017	19:39:55	3.3 m
ang20170616t210522	Dairy Manure Lagoon	6/16/2017	21:05:22	3.0 m
ang20170616t212046	Dairy Digester	6/16/2017	21:20:46	3.0 m
ang20180917t201723	Controlled Release	9/17/2018	20:17:23	2.3 m

3.3.2 Simulated Satellite Images

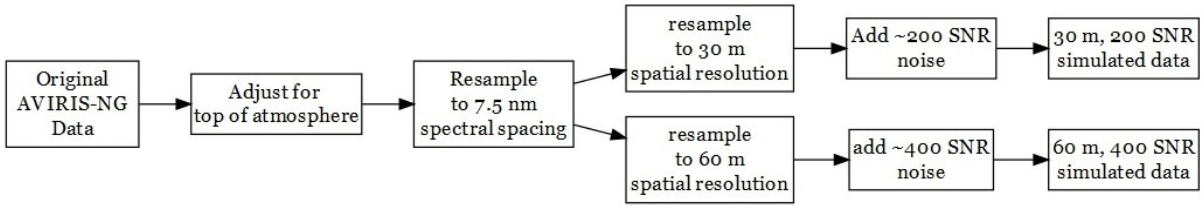


Figure 3.1: Flow chart of the steps for creating the simulated satellite data.

Aircraft to Top-of-Atmosphere

To simulate the additional atmosphere between the original aircraft height and the top of the atmosphere (TOA), we used MODerate resolution atmospheric TRANsmission 6 (MODTRAN6) to simulate one-way transmittance between the two heights [56]. Each transmittance simulation was generated with the aircraft height, latitude, longitude, day, and time of day of the original AVIRIS-NG flight. In addition, we assumed a background carbon dioxide, methane, and water vapor profile. Pixel radiance values from each image were multiplied by each simulated transmittance spectrum.

Spectral Resampling

The exact band centers and full width half maximum (FWHM) for EMIT are still to be determined. However, EMIT will most likely have a 7.4 nm spectral sampling with an 8.2 to 8.8 nm FWHM. We resampled spectra from AVIRIS-NG radiance images using a Gaussian convolution with band centers and FWHM based on these specifications. In total, the resampled spectra had 288 bands between 376.4 and 2500 nm.

Re-sample Spatial Resolution

Each image was resampled to 30 m and 60 m spatial resolutions using Gaussian resampling. The stated spatial resolution represents the full-width half maximum of the Gaussian function, with the x-y coordinates for each AVIRIS-NG pixel center used to calculate each pixel's weighting for resampling. The original unorthorectified AVIRIS-NG images were used for resampling, but pixel coordinate information allowed the creation of orthorectified 30 m and 60 m output images.

Sensor Noise

The SNR from AVIRIS-NG is higher than the proposed SNR for the EMIT sensor and in addition, after spatial and spectrally resampling the data, some of the noise from the original AVIRIS-NG data is reduced through averaging. Therefore, adding sensor noise back into the data is critical for accurately modeling satellite data. To properly model the SNR of the satellite sensors, a noise component aimed at mimicking expected sensor noise was added to the radiance. Modeled sensor noise comes from two main components: photon noise (*PN*) and constant noise (*CN*). *PN* increases as the number of photons hitting a detector increases, and scales with the square root of radiance. *CN* is mainly associated with electronics and quantization in the signal chain. A primary contributor is "read noise", caused by the analog-to-digital

conversion as the instrument digitally records the signal, and this parameter can be modeled as constant across wavelengths and pixels. To calculate *PN*, we first converted the spectral radiance to the total number of photons and then multiplied it by the etendue (G), which is calculated based on the area of the emitting source (in this case, the Sun) times the solid angle, band $FWHM$, integration time (τ), and the system transmittance factor (T):

$$PN = \sqrt{L_\lambda * (\frac{\lambda}{hc}) * G * FWHM * \tau * T} \tag{3.1}$$

where *PN* is the photon noise; L_λ is the radiance at each wavelength in each pixel; λ is the wavelength; and *hc* is Planck's constant times the speed of light. The AVIRIS-NG *CN* is 100 photons, therefore the same value was used for this simulation. The total noise was calculated as follows:

$$TN = \sqrt{(PN^2 + CN^2)} \tag{3.2}$$

where TN is the total noise. The total noise was then converted back to radiance units by substituting TN for *PN* in Equation (3.1) and inverting. TN converted to radiance was then multiplied by a random number from a Gaussian distribution with a mean of 0 and standard deviation of 1, then added to the original radiance for each wavelength for each pixel. *PN* increases with increasing radiance; for low radiance values, *CN* dominates the total noise and for higher radiance values, PN dominates. For the 60 m image, we multiplied PN by the square root of 2. The SNR was calculated by dividing the signal by the noise. In this case, the signal was the number of photons and the noise is the total noise. The resulting average SNR for the 30 m simulated satellite images in the SWIR (2100 nm–2500 nm) was 214 and the average SNR for the 60 m simulated satellite images in the SWIR was 484. Figure 3.2 shows the full spectrum SNR for the two simulations.

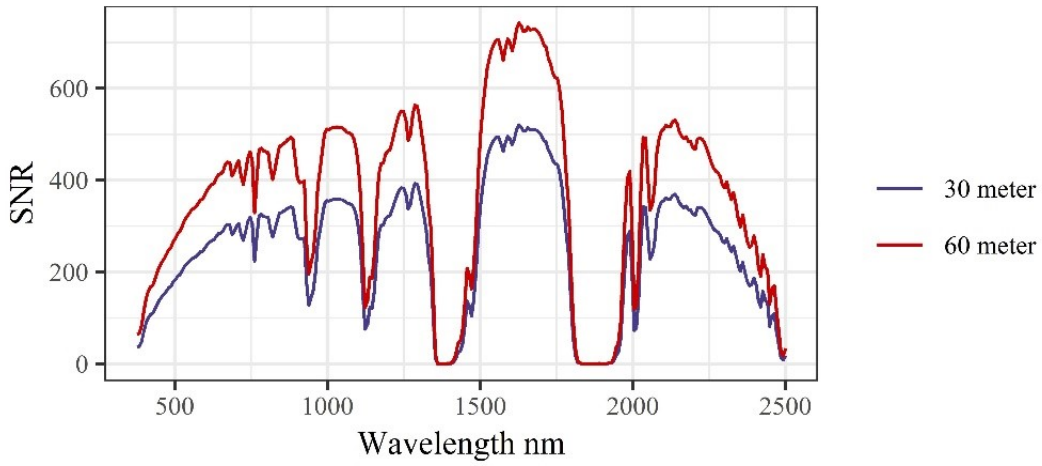


Figure 3.2: . Signal-to-Noise Ratio (SNR) for the 30 m simulated satellite data (blue) and for the 60 m simulated satellite data (red).

3.3.3 Matched Filter Methane Retrieval

The methane enhancement above the background for each pixel was estimated using an iterative matched filter technique tuned with a methane unit absorption spectrum [50, 21, 85, 86]. This iterative method included additional optimization factors that correct for spatially varying surface albedo. In addition, a L1 sparsity prior was included to reflect the expectation that methane enhancement is a rare occurrence within an image. This sparse approach is similar to methods employed in compressed sensing techniques for the reduction of acquisition time or improved resolution in fields as varied as medical imaging, radio astronomy, and electron microscopy. The iterative technique required for solving this sparse optimization problem additionally produces the explicit removal of any methane absorption signal from the background covariance matrix; failure to remove this signal is detrimental to matched filter techniques [85, 86]. This iterative matched filter with sparsity and albedo correction was applied to the AVIRIS-NG images and simulated 30 m and 60 m images. For all scenes, the sparse matched filter was run for 30 iterations, which includes an additional 50 percent margin over the 20 iterations that produced initial observable convergence of the optimization energy. The number

of iterations was based on observations of convergence from a test dataset. The methane unit absorption spectrum for each scene was computed from the change in radiance corresponding to a change in methane concentration in MODTRAN6 with each scene's sensor height and solar zenith angle. The albedo correction factor was estimated by the ratio of a pixel's radiance to the mean radiance in the scene. For the original AVIRIS-NG data, the matched filter was applied to groups of five adjacent columns, corresponding to adjacent detectors of the AVIRIS-NG instrument. This grouping improved the covariance estimate used by the matched filter to describe the background by suppressing artifacts from non-uniformity among detector elements [50]. For the simulated satellite images, column artifacts were averaged out by spatial resampling, and therefore the matched filter was applied to the entire image. The resulting methane enhancement image is measured in ppm-m, where ppm represents concentration and m represents the path length over which absorption occurs. Due to this algorithm's sparsity prior, many pixels are reported to have no methane enhancement above the background. This allows for interpreting the enhancement values as a detection result (presence/absence of methane for a positive/zero enhancement value). We also consider the resulting images as a quantitative retrieval directly from the per-pixel methane concentration. For more information on the retrieval algorithm please see Foote et. al., 2020 [87].

3.3.4 Integrated Mass Enhancement

The integrated mass enhancement (IME) is the sum of all the methane enhancement above the background concentration present in each plume. To calculate the IME, we first need to identify the pixels associated with the plume and filter out spurious signals. We applied a 200 ppm-m threshold to filter out any potential spurious signals. The 200 ppm-m threshold was determined by reviewing the mean and standard deviation for the matched filter outputs. A 200 ppm-m value represents a round average of one standard deviation below the average

mean of the enhanced pixels. To further filter out spurious signals, we calculated the number of pixels in contiguous clusters, any clusters below a certain threshold were filtered out. For the original AVIRIS-NG images, any clusters below 350 contiguous pixels were filtered out. For the 30 m satellite simulation, clusters below four pixels were filtered out and for the 60 m satellite simulation, clusters below two pixels were filtered out. Different thresholds were used for some cases based on empirical adjustments and are documented in Appendix A. We then calculated an integrated mass enhancement (IME) or the sum of the methane present in each plume [25] as follows:

$$IME = k \sum_{i=0}^{n} \alpha(i) S(i) \tag{3.3}$$

where α is the methane value in ppm-m for the n pixels in the plume over the pixel area S and the constant k is used to convert to methane mass units [25].

3.3.5 Flux Estimate

A simple flux estimate can be calculated using the IME, the length of the plume, and the wind speed. The methods for calculating the IME are listed above. To calculate the length of the plume, we identified the two pixels in the plume with the furthest distance and calculated the Euclidean distance between the two pixels. HRRRv3 10 m wind fields in forecast mode were used to estimate wind speeds for the location and time of each AVIRIS-NG scene [88, 89]. Using the 3 km grid product, an average wind speed and standard deviation was calculated using a total of 27 HRRRv3 grid cells, a 3 by 3 box centered on the source for three time-steps (plume detection time within 1 hour). The equation for the flux is as follows:

$$Flux = \frac{IME}{l} s \tag{3.4}$$

where IME is the amount of methane in kg (calculated above); l is the plume length in meters; s is the wind speed meter/hour; and the resulting flux in the units of kg/hour. The uncertainties for the flux estimates result from uncertainties in the wind speeds.

3.4 Results and Discussion

3.4.1 Methane Plumes by Sector

One advantage of using a satellite system to detect methane plumes is the ability to observe a large diversity of methane emitting sectors. Plumes from different sectors have different shapes, sizes, and underlying land cover that can influence how well a plume is detected. Here, we look at plumes from the three largest anthropogenic methane emitting sectors to understand how well a satellite system would perform in each sector. The following sections present the matched filter methane retrieval results for the AVIRIS-NG, 30 m, and 60 m satellite simulations.

Petroleum and Natural Gas

The natural gas and petroleum industry represents about 30 percent–35 percent of all anthropogenic methane emissions globally [71, 72, 90]. Methane emissions from this sector can be challenging to characterize, given the significant variability in source type, plume shape and size, and intermittence. Here, we present three examples from different sources. The first is a gas storage facility that has two emission sources, the second is a well with a methane plume, and the third is a leak from a natural gas distribution line in a neighborhood [22]. All plumes were detectable from the 30 m and 60 m simulated satellite images.

Figure 3.3 depicts the results of two plumes at the Honor Ranch gas storage facility. The source for the top plume is an emergency shutdown stack and for the bottom plume, it is a

compressor unit. In the AVIRIS-NG image, these two plumes were distinct, which allows the plumes to be attributed to their exact sources. In the 30 m image, some of the detail of the plume is lost, but two distinct plumes are still visible. At 60 m, the methane enhancement is visible, but the distinction between the two plumes disappears. At the 30 m and 60 m resolution, we could easily attribute the plume to the facility, but not to the exact locations within the facility as we could with the original AVIRIS-NG image.

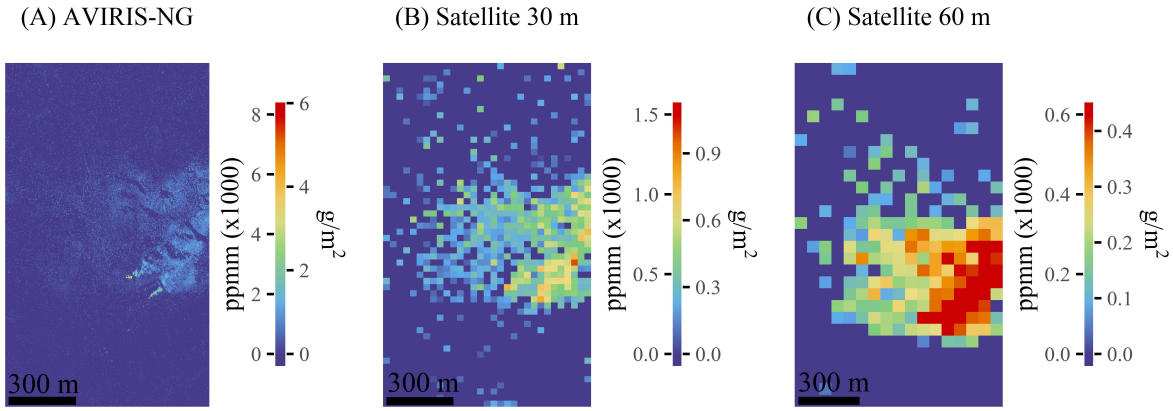


Figure 3.3: Matched filter methane retrieval for a plume from a 4 November, 2016 AVIRIS-NG image. The plume is from the Honor Ranch gas storage facility, where there are two plumes, one from an emergency shutdown stack and the other from a compressor unit. (A) Results from the original AVIRIS-NG image. (B) Results from the 30 m simulated satellite image with 200 SNR. (C) Results from the 60 m simulated satellite image with about 400 SNR. The left side of the scale bar are units in parts per million per meter (ppm-m) above the background. The right side of the scale bar are methane units in g/m^2.

Figure 3.4 shows the matched filter results from a methane plume from a well. Given the sheer quantity and high density of wells throughout the United States, a satellite system would be well suited to identify those that are emitting methane. This particular example is from a hydrocarbon extraction site within the Aliso Canyon gas storage facility. The details of the plume are most distinct in the original AVIRIS-NG image. In the 30 m and 60 m satellite images, the plume is still clearly detectable, but becomes increasingly less detailed.

One concern in the natural gas and petroleum sector are leaks and other fugitive emissions. Not only do these emissions contribute to the overall greenhouse gas budget, but they also

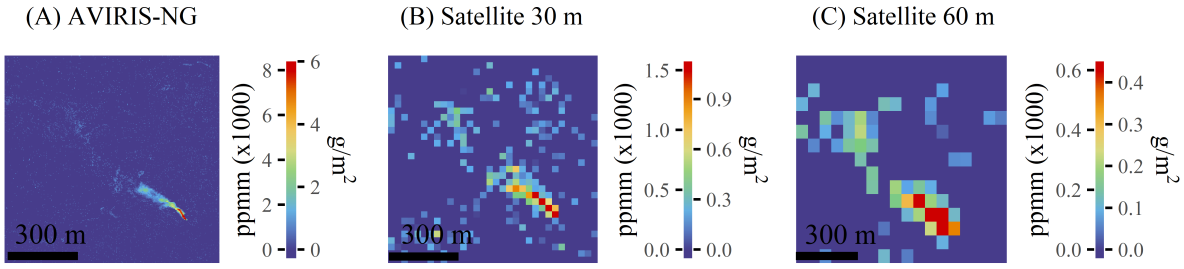


Figure 3.4: Matched filter methane retrieval results from a plume from a 18 September, 2017 AVIRIS-NG image. The plume is from an oil producing well in Aliso Canyon. (A) Results from the original AVIRIS-NG image. (B) Results from the 30 m simulated satellite image with 200 SNR. (C) Results from the 60 m simulated satellite image with about 400 SNR. The left side of the scale bar are units in parts per million per meter (ppm-m) above the background. The right side of the scale bar are methane units in g/m^2.

represent lost revenue and in sufficiently large amounts can pose a public safety hazard. The ability to detect leaks over large areas could help improve the mitigation of greenhouse gas emissions and hazards. Figure 3.5 is an example of an underground natural gas distribution line leak that was detected in 2016 in the Chino Hills neighborhood, CA. This particular leak was detected using the real time methane mapping capability of AVIRIS-NG and the results were shared with the local gas company who quickly confirmed and repaired the leak [50]. The plume is clearly visible in the AVIRIS-NG image and a distinct methane enhancement is visible in the 30 m and 60 m simulated images.

Current and past satellite sensors, like SCIAMACHY and TROPOMI, are able to detect regional methane enhancements over areas with heavy oil and gas production, like the methane anomaly over the Four Corners areas in the Western United Sates [91], but cannot identify the exact location of individual point sources. Currently, the only way to locate a specific source is through a ground or airborne campaign, which can be costly, time consuming, and have a limited geographic extent [25]. Therefore, a higher spatial resolution satellite sensor that could identify point sources would help us understand the dynamics of oil and natural gas methane emissions. Other studies have looked into the possibility of using spaceborne sensors to do fine

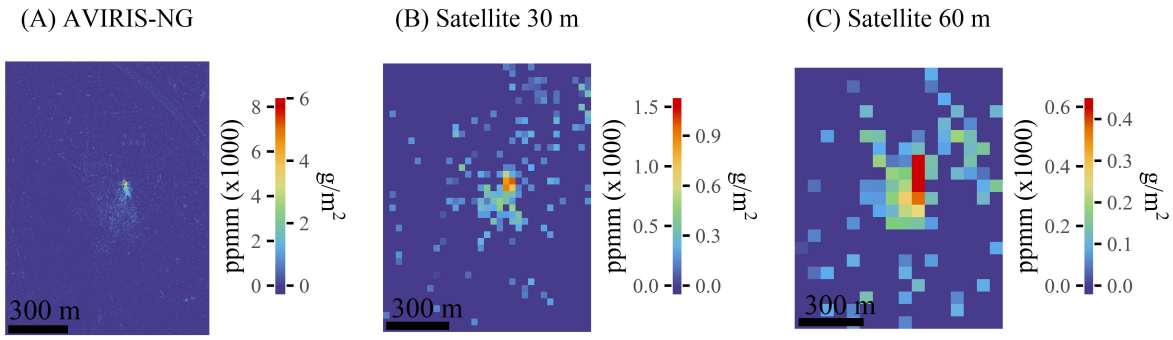


Figure 3.5: Matched filter methane retrieval results for a plume from a 15 September, 2016 AVIRIS-NG image. The plume is from a low pressure natural gas distribution line leak in the Chino Hills neighborhood. (A) Results from the original AVIRIS-NG image. (B) Results from the 30 m simulated satellite image with 200 SNR. (C) Results from the 60 m simulated satellite image with about 400 SNR. The left side of the scale bar are units in parts per million per meter (ppm-m) above the background. The right side of the scale bar are methane units in g/m^2.

scale methane plume detection. Varon et al. [76] performed a sensitivity study indicating that individual plumes could be mapped with a sufficiently sensitive constellation of point source monitoring satellites, similar to the planned GHGSat fleet. In addition, Cusworth et al. showed that plumes from oil/gas facilities could be detected with the upcoming EnMAP mission [29]. The future generation of imaging spectrometers will help us to improve our understanding of methane emissions from the oil and natural gas sectors.

Landfill/Wastewater Treatment

The waste sector, which includes landfills and wastewater treatment, is thought to make up about 16 percent of global anthropogenic methane emissions, with the majority coming from landfills [71, 72]. Globally, landfills take on many different forms, and factors like the composition of the waste, the temperature, the age, and management system can all influence the amount of methane emitted from a landfill [92, 93, 94]. Of those landfills exhibiting plumes during the California Methane Survey, plumes appeared persistent across multiple years, therefore making them an excellent target for spaceborne studies [27]. Satellite monitoring of these

sites can help understand emissions from this under sampled sector, assess gas capture systems, and generally provide a better understanding of landfill emissions.

Figure 3.6 shows the matched filter results from the Newby Island landfill in San Jose, CA. In this image, a very large plume is present, originating from multiple places in the landfill. Note the scale on (C) Satellite 60 m is higher than the other figures, which is due to the large size of the plume. The plume remains visible in all simulated satellite images. Large plumes have been detected with AVIRIS-NG from other landfills in California and a large landfill in India, indicating that this type of methane source can be studied from space.

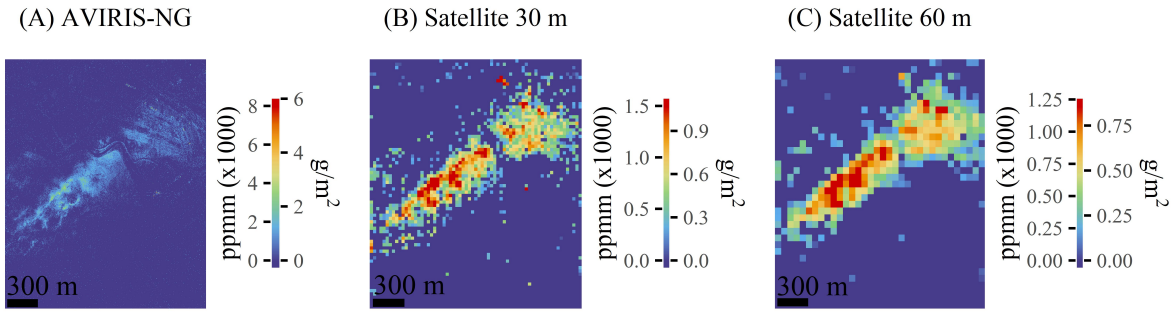


Figure 3.6: Matched filter methane retrieval results for a plume from a 18 June, 2017 AVIRIS-NG image. The plume is from Newby Island Land fill in San Jose, CA. (A) Results from the original AVIRIS-NG image. (B) The matched filter results from the 30 m simulated satellite image with 200 SNR. (C) Results from the 60 m simulated satellite image with about 400 SNR. The left side of the scale bar are units in parts per million per meter (ppm-m) above the background. The right side of the scale bar are methane units in g/m^2.

Adjacent to the landfill is a wastewater treatment facility. Figure 3.7 shows a small plume that is evidently emanating from one of the tanks. The plume is clearly visible in the AVIRIS-NG image, but less so in the 30 m and 60 m images. Given this result, the detection of a methane plume from this particular source will be difficult for the satellite instruments modeled here.

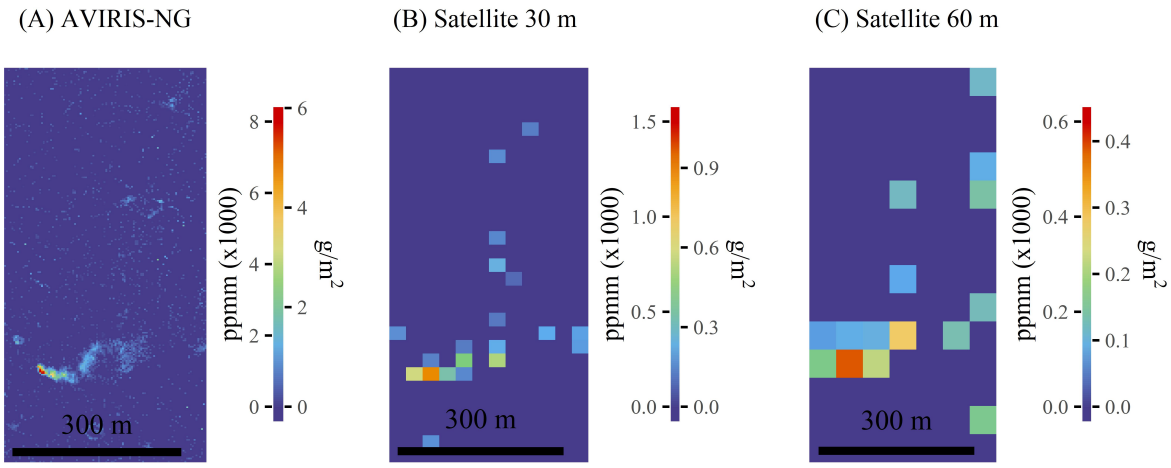


Figure 3.7: Matched filter methane retrieval results for a plume from a 18 Jun, 2017 AVIRIS-NG image. The plume a wastewater treatment plant south of the Newby Island Landfill. (A) The matched filter results from the original AVIRIS-NG image. (B) Results from the 30 m simulated satellite image with 200 SNR. (C) Results from the 60 m simulated satellite image with about 400 SNR. The left side of the scale bar are units in parts per million per meter (ppm-m) above the background. The right side of the scale bar are methane units in g/m^2.

Dairies

Enteric fermentation and manure management make up about 28 percent of global anthropogenic methane emissions [71, 72, 95]. This is a significant anthropogenic methane source, but the most difficult to map using this method. Enteric fermentation is an area source and does not produce methane from a single easily identifiable point. This makes mapping methane from cattle with imaging spectroscopy more difficult. However, there is an exception for some methods of manure management. Many manure lagoons from large dairies and some digesters in California produce small yet detectable plumes. Figure 3.8 shows the matched filter results of a plume from a typical dairy manure lagoon. It is clearly visible in the AVIRIS-NG images and remains detectable in the 30 m and 60 m images.

An anaerobic digester is an enclosed area where the breakdown of organic material (manure) is promoted and the biogas is then captured and used as an energy source. Many studies have measured the potential biogas produced from digesters in order to estimate gas production

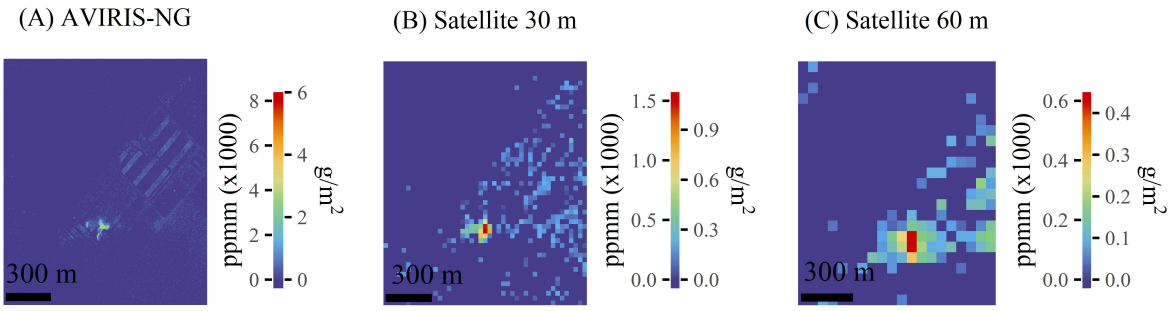


Figure 3.8: . Matched filter methane retrieval results for a plume from a 16 June, 2017 AVIRIS-NG image. The plume is from a typical manure lagoon on a California dairy. (A) The matched filter results from the original AVIRIS-NG image. (B) The matched filter results from the 30 m simulated satellite image with 200 SNR. (C) The matched filter results from the 60 m simulated satellite image with about 400 SNR. The left side of the scale bar are units in parts per million per meter (ppm-m) above the background. The right side of the scale bar are methane units in g/m^2.

[93, 96]. However, few studies have looked at the gas lost due to leaks. In addition, emissions from manure can be well constrained with isotopic measurements, but this does not allow for the distinction between an open manure lagoon and a digester [97]. Regular satellite measurements of large dairy production areas like California's San Joaquin Valley would improve understanding of the dynamics of methane emission from manure management. Figure 3.9 shows the matched filter results of three plumes in the upper left corner coming off a digester in California. In the 30 m and 60 m simulated images, the plume is still visible, but has blended into one larger plume instead of three smaller ones.

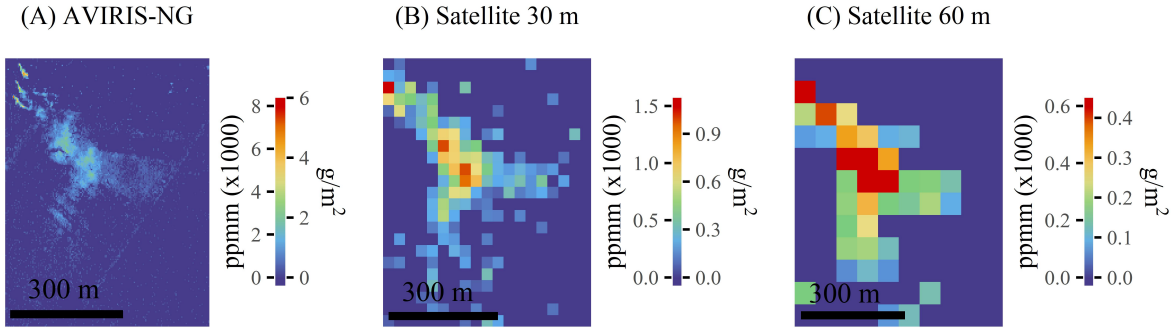


Figure 3.9: Matched filter methane retrieval results of a plume from a 16 June, 2017 AVIRIS-NG image. The plume is from a covered lagoon digester in California. (A) The matched filter results from the original AVIRIS-NG image. (B) The matched filter results from the 30 m simulated satellite image with 200 SNR. (C) The matched filter results from the 60 m simulated satellite image with about 400 SNR. The left side of the scale bar are units in parts per million per meter (ppm-m) above the background. The right side of the scale bar are methane units in g/m^2.

Controlled Release Experiment

In September 2018, a controlled release experiment was performed to test the accuracy of the AVIRIS-NG methane retrievals. Natural gas was released by a pipeline operator at a known flux while AVIRIS-NG flew over. We analyzed one scene from this experiment to verify that our methods were producing reasonable results (Figure 3.10). The flux during this flight was 103.71 kg/h and the retrieval from AVIRIS-NG with our methods was 117.59 ± 15.53 kg/h. The agreement between the AVIRIS-NG flux and actual flux was good, however, the agreement for the 30 m and 60 m images was not as close (Table 3.2). This was a smaller plume and the entire plume spanned one or two pixels in the 60 m satellite simulation, therefore calculating an accurate flux was more difficult. Regardless, the plumes were visible in both the 30 m and 60 m, which indicates that plumes with a flux as small as 100 kg/h will be visible with the next generation of satellite imaging spectrometers.

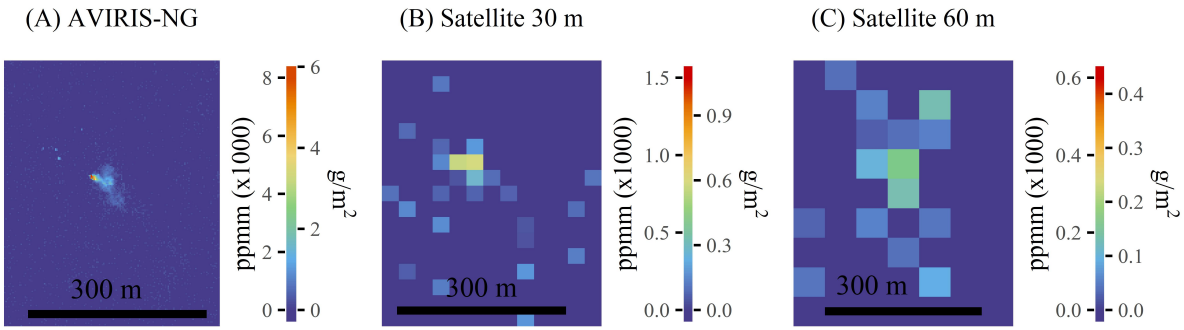


Figure 3.10: Matched filter methane retrieval results from a controlled release experiment on 17 September, 2018. (A) The matched filter results from the original AVIRIS-NG image. (B) The matched filter results from the 30 m simulated satellite image with 200 SNR. (C) The matched filter results from the 60 m simulated satellite image with about 400 SNR. The left side of the scale bar are units in parts per million per meter (ppm-m) above the background. The right side of the scale bar are methane units in g/m^2.

3.4.2 Flux

The fluxes for the AVIRIS-NG, 30 m, and 60 m images were calculated using the methods presented above. Calculating the flux allows the scientific community to quantitatively assess the volume of methane emitted per source and sector. We tested an image from a controlled release experiment (presented above) to empirically validate our flux estimates. We calculated a flux estimation of 117.59 ± 15.53 kg/h for the AVIRIS-NG image of the controlled release experiment. The reported flux at the time of the image was 103.71 kg/h. These results are close enough that we feel confident that the AVIRIS-NG images provide a good estimation of the magnitude of the flux. We can therefore compare the results from the satellite simulations to the original AVIRIS-NG image to understand how well a satellite system would perform. In general, the flux estimates from the satellite simulations are consistent with the flux estimations from the AVIRIS-NG image. Table 3.2 provides the results of the flux estimates for the AVIRIS-NG, the 30 m, and 60 m images. Figure 3.11 shows the flux results from the 30 m and 60 m image plotted against the flux results from the AVIRIS-NG image. The relationship between the satellite simulations and the AVIRIS-NG image was strong (R^2 = 0.98), although

the linear regression line did not match the 1:1 line, the error bars crossed or came close to the 1:1 line. The satellite simulations tended to overestimate the flux for both simulations. In addition, the overestimation appears to become larger as the size of the methane plume increases, however, when the error is normalized by the size of the plume, this relationship breaks down. One explanation for the overestimation is that the coarser spatial resolution inflates the spatial extent of the plume, which increases the IME and plume length. However, the IME tends to increase more than the plume length, causing the flux to also increase. In a similar study, Cusworth et al. found that the satellite simulation underestimated the AVIRIS-NG retrieval, but they used a different retrieval algorithm, a different plume mask, and did not simulate a 60 m instrument [29]. More work will be needed to be done to understand precisely how increasing spatial resolution changes the IME and therefore the flux.

Table 3.2: The flux and uncertainty due to wind for the selected plumes.

		Flux (kg/hr)	
Source	**AVIRIS-NG**	**30 m**	**60 m**
Gas Storage Facility	1209.97 ± 131.11	1497.54 ± 162.26	1674.46 ± 181.43
Gas Distribution Line	156.20 ±48.17	224.63 ±69.28	225.62 ±69.58
Landfill	1231.67 ±332.78	1613.23 ±435.87	1663.51 ±449.45
Well	553.03 ±92.76	578.53 ±108.46	547.73 ±91.87
Wastewater Treatment	198.00 ±40.38	159.42 ±32.51	179.11 ±36.53
Dairy Manure Lagoon	397.89 ±434.38	584.28 ±637.86	480.28 ±524.33
Dairy Digester	552.65 ±47.75	578.53 ±49.98	580.00 ±20.11
Controlled Release	117.59 ±15.53	167.20 ±22.09	65.42 ±8.64

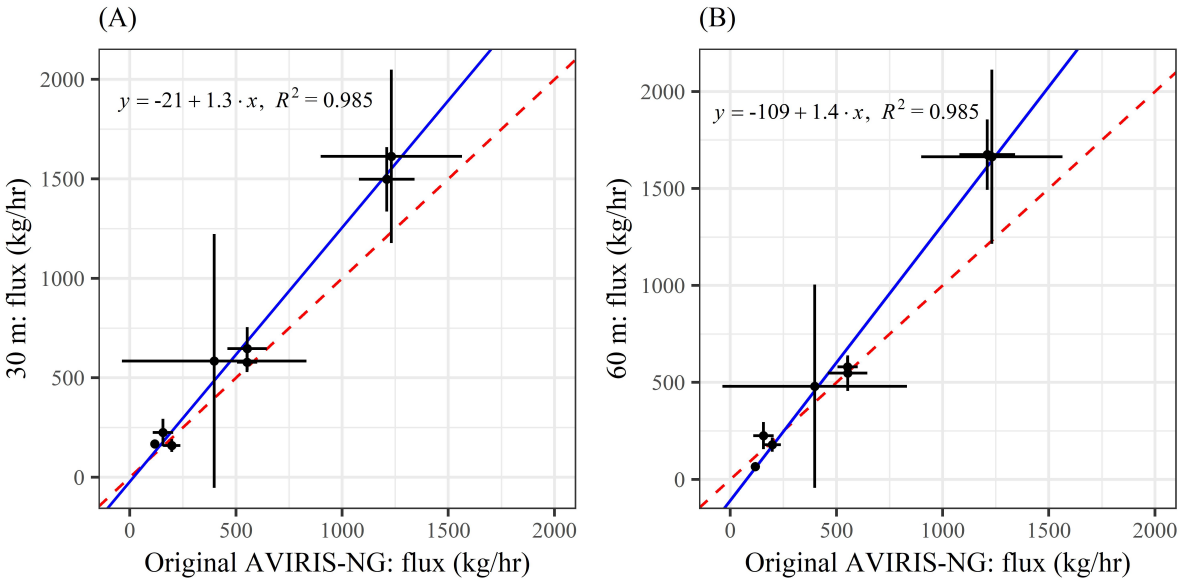


Figure 3.11: (A) The 30 m flux plotted against the original AVIRIS-NG. The error bars represent uncertainty in the wind speed estimate, which in turn leads to uncertainty in the flux estimate. The R2 = 0.98, the slope = 1.3, and the y-intercept = 21. (B) The 60 m flux is plotted against the original AVIRIS-NG. The errors bars represent error due to wind speed. The R2 = 0.98, the slope = 1.4, and the y-intercept = 109. For both figures, the red dashed line is the one-to-one line and the blue line is the best fit linear regression.

3.4.3 Spatial Resolution and Signal-to-Noise Ratio

In this analysis, the spatial resolution and SNR are the two variables that distinguish the 30 m and 60 m satellite simulations. Sensor design often requires compromises between different performance measures. For example, designers may sacrifice SNR for finer spatial resolution and vice versa. We looked at which of these factors had the largest impact on methane gas mapping. We used the Honor Ranch gas storage facility as an example and tested how our retrieval changed with different noise levels; no added noise, 400 SNR, and 200 SNR. We found that visually, the plume became less distinct from the background and the presence of spurious signals increased, which in turn slightly increased the flux estimate (Figure 3.12). We also tested the image with the same SNR at the native resolution (1.6 m), 30 m, and 60 m. We found that the plume became less detailed with coarsening spatial resolution, indicating that

spatial resolution, rather than SNR, had a larger influence on detecting plumes. In addition, we performed an Analysis of Variance (ANOVA) with a Tukey post hoc using the flux and standard deviation, and found that the only image that was significantly different ($p \leq 0.05$) from the original AVIRIS-NG was the 60 m image. More plumes as well as a larger range in SNR and pixel size will be needed to accurately quantify how noise versus spatial resolution effects plume retrieval. However, these results indicate that changing the spatial resolution has a larger impact than changing the noise.

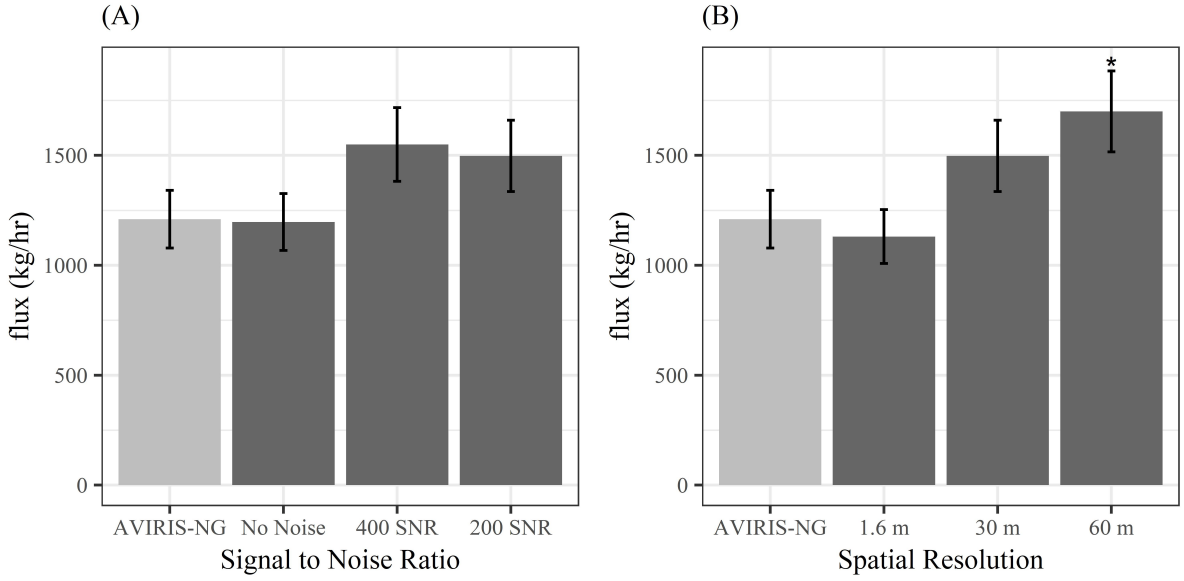


Figure 3.12: (A) The y-axis is the flux in kg/h and each bar on the x-axis represents an image. The spatial resolution is held constant (30 m) but the SNR varies from no additional noise, 400 SNR in the SWIR, and 200 SNR in the SWIR. (B) The y-axis is the flux (kg/h) and the bars on the x-axis represent images where the SNR is constant (200 SNR) but the spatial resolution is the native 1.6 m, 30 m, and 60 m. The 60 m image is the only image that is significantly different from the AVIRIS-NG, p = 0.019. The light gray bar in both charts is the original AVIRIS-NG for reference and the error bars represent the flux error due to wind speed uncertainty.

3.4.4 Limitations

The satellite simulations indicate that point source methane mapping will be possible with the future generation of satellite imaging spectrometers. However, there are some limitations with the simulations presented here. While the specifications for the simulation represent the best available knowledge about the design of a future spectrometer (EMIT), there remains a possibility that specifications will change before launch. Other satellite designs might include different spectral, spatial, or SNR characteristics not modeled here, however these are unlikely to be drastically different. In addition, this study did not account for other factors associated with satellite sensors including potential orbits, cloud cover, sun angles, and surface brightness. In particular, surface brightness has proven to have a large influence on methane retrievals [29, 98]. While there is inherent variability in surface brightness in the AVIRIS-NG scenes, we were not able to control this variable. Finally, while the flightlines from this study represent a range of emissions over variable surface terrain, more challenging examples containing lower fluxes were not tested.

Other limitations in the study include the methods we used to create a plume mask and the flux estimate. The plume mask is intended to isolate the plume and filter out spurious signals or false positives. Spurious signals were present in both the airborne data and the satellite simulations. For this study, we attempted to be as consistent as possible and therefore generally used consistent thresholds to isolate the plume. It should be noted, however, that more tailored thresholding could produce better results in future studies. The thresholding and segmentation can have a large impact on the results, more work is needed to determine the best practices for how to approach this. Additional work is required to assess the impact that these spurious signals may have on our IME and flux estimates. This study also used a simple method to estimate the flux of the plumes. More robust flux calculations could lead to more accurate results.

3.5 Conclusions

We tested the potential to use future Earth observing satellites such as EMIT or SBG to map and measure methane plumes from the three main anthropogenic emission sectors. These particular future satellites will measure in the SWIR with 7–10 nm spectral sampling, the spatial resolution will range from 30 m to 60 m pixels, and will have a SNR in the SWIR between 200 and 400. To test the potential of using these instruments for high resolution methane mapping, we simulated two proposed satellite designs from the AVIRIS-NG data. The first was a 30 m pixel resolution with a 200 SNR in the SWIR, the second was a 60 m pixel resolution with 400 SNR in the SWIR. We then ran a matched filter methane retrieval algorithm on the simulated satellite images and compared it to the original AVIRIS-NG.

We found that for almost all plumes, the methane enhancement remained visible at the coarser spatial resolutions. This indicated that most point source emissions from the largest anthropogenic sources should be detectable, at minimum, in a 30 m resolution image. We found that when we quantified the flux of the plume in the simulated images, it correlated well with the flux calculated from the AVIRIS-NG results. In addition, for the controlled release experiment, the flux calculated from the AVIRIS-NG data was similar to the known flux. Within the limits of our study, we also found that the spatial resolution had a larger impact on the results than the SNR. We conclude that a satellite system will be able to map and quantify the biggest of the point source emitters and should be able to detect plumes as small as 100 kg/h, although accurate quantification of flux may be more difficult. These plumes may only be a small fraction of the total number of plumes, but likely represent up to 40 percent of emitted methane.

While the future generation of satellite imaging spectrometers were not designed for high resolution gas mapping, this work indicates that they will be able to map methane plumes and quantify emission rates. However, imaging spectrometer concepts have been developed that

would utilize finer spectral resolution to improve gas sensitivities [75, 62]. Eventually, these sensors will become integrated into larger greenhouse gas monitoring schemes and will help scientists better understand global methane emissions.

Chapter 4

Exploring the Effects of Wind Speed, Flux Rate, and Spatial Resolution on Mapping Methane Plumes with Imaging Spectrometers

With Philip E Dennison, Andrew K Thorpe, Siraput Jongaramrungruan, Christian Frankenberg, Daniel Cusworth, Riley M Duren, David R Thompson, Christopher Funk, Jennifer Y King, and Dar A Roberts

4.1 Abstract

The Airborne Visible and Infrared Imaging Spectrometer Next Generation (AVIRIS-NG) and similar imaging spectrometers are becoming commonly used for point source greenhouse gas emissions mapping. These point source maps are a critical information source that will help us understand and mitigate a very dangerous source of radiative forcing. As methane mapping with these instruments and similar future satellite sensors becomes more prevalent, understanding the factors that influence detection and quantification of methane plumes is essential. In this study, we analyze how wind speed, spatial resolution, and flux rate influence the detectability and quantification of methane plumes. We first use synthetic images and a novel statistical test to determine the best thresholds to apply to two commonly used methane retrieval algorithms. For the first time, we show how the optimal threshold maybe derived empirically, providing an alternative to the use of ad hoc values.We then use the results from the threshold analysis to segment Large Eddy Simulation (LES) methane plumes. The LES plumes, which model plumes with various wind speed and flux rates, are used to understand the sensitivities regarding wind speed, flux rate, and spatial resolution. We identify the minimum flux rates detectable at 5-15 m spatial resolution to be between 20-30 kg/hr. For the 30-60 m resolution, the minimum detection was between 40-210 kg/hr, and for the 120-500 m resolution, the minimum detection was between 220–5000 kg/hr. We also calculate the percent errors in the flux rate calculation associated with wind speed. The most accurate calculated flux rates were found to be at moderate wind speeds (2-4 m/s). These results quantify error associated wind speed and indicate which spatial resolution will be best for mapping point source methane emissions globally.

4.2 Introduction

Methane (CH_4) is an important greenhouse gas (stronger radiative forcing per molecule than CO_2), and increasing concentrations are contributing significantly to global climate change. Overall, methane is estimated to be responsible for about 20 percent of all atmospheric radiative forcing [2]. About 60 percent of all methane emissions are anthropogenic, and the majority of those emissions come from the energy, waste, and agriculture sectors [3]. Emissions from these sectors tend to be point sources, meaning they are methane plumes emanating from localized and identifiable sources. Finding these sources is a critical aspect of effective mitigation. Methane mapping with imaging spectrometers is becoming a prominent method for detecting and quantifying point source methane plumes [99]. As mapping techniques become integral to our greenhouse gas observing system, understanding the limitation of these sensors also becomes crucial. In previous studies, wind speed and flux rate have been shown to greatly impact methane detections [100, 76]. In addition, sensitivities to wind speed and flux rates can change with spatial resolution [28, 29]. This study focuses on the sensitivity of methane detection and quantification to wind speed, flux rate, and spatial resolution. In addition, we present a statistical method for quantitatively determining thresholds for methane detection and use these thresholds in a sensitivity analysis.

Imaging spectrometers, such as AVIRIS NG, are able to locate methane plumes and attribute those plumes directly to their source [20]. This works particularly well for point sources [27]. The shape and size of the methane plume once it escapes from the source are primarily driven by speed and direction of the wind. Previous studies have shown how wind speed can affect the shape of a plume and the integrated mass enhancement (IME) value, which is the total mass of methane within the plume area. By changing the shape and IME, wind speed can therefore affect the calculated flux estimates [100]. However, measuring wind speed at the location of the plume and at the time of the flight can be difficult. Typically, anemometer

measurements at the exact location of the plume are unavailable. Therefore, Large Eddy Simulations (LES), mathematical models for simulating turbulent flows, have become an important tool for understanding the interactions between wind and the methane plumes [100]. These 3D simulations can be reduced to 2 dimensions to mimic what an imaging spectrometer would retrieve and can help us understand the effect of wind on methane plumes retrievals.

This work is especially important given the rapid advances in our Earth observation systems. A new generation of satellite imaging spectrometers and high spatial resolution gas mapping satellites is forthcoming. These include imaging spectrometer missions such as the PRecursore IperSpettrale della Missione Applicativa (PRISMA), which recently launched [79]. The Earth surface Mineral dust source Investigation (EMIT) and the Environmental Mapping and Analysis Program (EnMAP)[80, 77] are additional sensors with methane mapping potential. These two sensors are scheduled to launch in 2022. Missions such GHGsat and the Carbon Mapper mission are methane specific missions that use similar technology to target greenhouse gases [30]. These sensors have or will have a wide range in spatial resolutions, and some are still in the planning phase, where the spatial resolution, along with the other sensor attributes, is yet to be determined. Previous studies have highlighted that spatial resolution may be an important factor in determining how well these sensors can map point sources [28].

To calculate the methane concentration from the airborne or satellite data, two main methane retrieval algorithms have emerged in the published literature: matched filters [87, 21, 50] and the Iterative Maximum a Posteriori Differential Optical Absorption Spectroscopy (IMAP-DOAS) algorithm [23, 51]. The matched filter technique is a statistically based methane detection technique and is the primary method for detecting methane with imaging spectrometer data. More recently it has also been used, with success, to estimate the per-pixel abundance of methane [87]. IMAP-DOAS is a physically based quantitative retrieval algorithm that is used post-detection to estimate per-pixel methane abundance.

In interpreting the results from both of these algorithms, a detection threshold is applied to

separate the background from the plume. In previous studies, the threshold values applied to these algorithms have been decided a priori in an ad hoc manner. For example some studies have used a 200 ppm-m threshold while others have used a 500 or 1000 ppm-m threshold, and the exact rationale for threshold selection has not been formalized [27, 25, 100]. In this study, for the first time, we use synthetic images to quantitatively determine appropriate thresholds. We then analyze the effect of different thresholds on the final results. Determining appropriate thresholds is a necessary precursor to using the LES plumes, but it is also an important study on its own. The LES plumes include methane values that would not realistically appear in an actual methane retrieval; therefore, they need a threshold applied. In addition, methane retrievals with AVIRIS-NG data tend to be noisy and thresholding the data is a necessary step in isolating plumes. Not only is this a sensitivity study, but the analysis of thresholds for the two retrieval algorithms will also benefit future studies and improve emission estimates using imaging spectrometers.

As this field moves forward and new instruments are developed, it is crucial that we understand how factors such as wind speed and flux rate affect detections at different spatial resolutions. This study, therefore, will help us to understand the limitations of our current sensors and to optimize future sensors. Below we present results determining the best thresholds for two retrieval techniques. Then we applied those to LES plumes to understand the sensitivities regarding wind speed, flux rate, and spatial resolution. More specifically, the goals of the sensitivity study are to i) identify thresholds for segmenting the methane retrievals. ii) identify minimum flux rates detectable at different spatial resolutions, and iii) explore how wind speed changes the size and shape of plumes and therefore the calculated flux estimates.

4.3 Methods

In this study, we first created a synthetic AVIRIS NG image with known modeled methane values. We then ran two common methane retrieval algorithms, the matched filter and IMAP-DOAS, on the synthetic image. We used the retrieval results to determine the best thresholds to filter the background values from the plume. We then used LES plume models with different wind speeds, flux rates, and spatial resolutions to see how the different thresholds impacted the calculated fluxes. We looked at how the minimum detectable flux rate changed with wind speed and spatial resolution and how the wind speed affected the size and shape of the plume and therefore the calculated flux. Figure 4.1 summarizes the flow of the methods in this study.

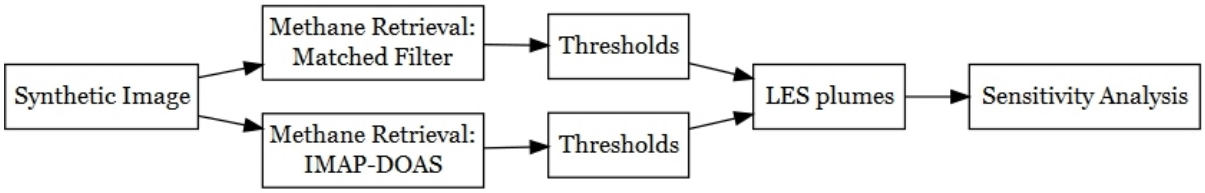


Figure 4.1: Flow chart of the methods

4.3.1 Synthetic Images

A synthetic image was created to use as the basis for objective tests of the two algorithms. Synthetic images provide a solid foundation for such evaluation, because the methane concentration at each pixel is a known quantity. The base for the synthetic image was a 2014 AVIRIS NG flight line from the Santa Barbara area. We started with the Jet Propulsion Laboratory (JPL) reflectance product. To convert the reflectance data to radiance, a radiance look-up table was created in MODTRAN6 [56]. The lookup library consisted of methane values that varied from 0.0 to 7.4 ppm above background in the bottom 1 km of the atmosphere with a 0.2 ppm step. The albedo varied from 0.0 to 1.0 with a 0.001 step; this was intended to capture as much variation in surface albedo as possible. It is important to note the the solar zenith angle assumed

in the model was 29.77 degrees. The MODTRAN6 models also assumed a sensor height above the upper limit of the simulated atmosphere (120 km), to simulate how the methane absorption spectra would look from a spacecraft. The additional atmospheric constituents (gases, aerosols, etc.) were held constant and are listed in Table 4.1. A methane gradient was created to represent the methane enhancement or "plume" in the image. The gradient extended the width of the flight line and varied from 0.2 to 7.4 ppm above background, with a 0.2 ppm step. In total, the methane enhancement took up about 3 percent of the image.

In order to convert from reflectance to radiance, we iterated through every pixel in the reflectance image. For each wavelength of each reflectance spectrum (each pixel), the original reflectance value was matched with the closest simulated reflectance value for a specified methane concentration [52]. The corresponding radiance from the lookup table was then extracted and saved, and the process was repeated for the next wavelength. This resulted in a synthetic image of radiance spectra with known atmospheric parameters. For more information on creation of the synthetic image, please see Ayasse et al. (2018).

One parameter of interest in this study is the albedo in the Short Wave Infrared (SWIR). The albedo in the synthetic image will come from the albedo inherent in the original AVIRIS NG flight. The original AVIRIS NG flight from which we derive the underlying surface reflectance is a flight from June 2014 over Santa Barbara, CA. The solar zenith angle at the time of the flight was 14.4 degrees. In addition, the underlying surface was a combination of residential and commercial buildings with significant vegetation cover (see Figure 4.4). This diversity of surfaces represents a large range of albedos from which to do our analysis.

4.3.2 Matched Filter

The matched filter technique used in this study was the robust column-wise matched filter tuned with a methane unit absorption spectrum [50]. This matched filter tests each spectrum

Table 4.1: MODerate resolution atmospheric TRANsmission (MODTRAN) inputs for simulating the atmosphere.

Attribute	Values
Wavelengths	350-2500 nm
Carbon dioxide	405 ppm
Water Vapor	1.535 cm
Visibility	30 km
Methane (background)	1.7 ppm

against a target signature while accounting for the background covariance. Here the target signature is a methane unit absorption spectrum, computed from the change in radiance corresponding to a 1 ppm change in methane concentration enhancement in MODTRAN6 for the scene's sensor height and solar zenith angle. The column-wise matched filter recognizes that push broom sensors, like AVIRIS NG, have a different detector for each column with unique spectral sensitivity and noise characteristics, resulting in a slightly different background covariance for each column. Therefore, the matched filter is applied separately to each column. More information on this method can be found in Thompson et al. (2015).

The resulting methane enhancement image is measured in ppm-m, where ppm represents concentration in parts per million and m represents the path length over which absorption occurs in meters. This algorithm can be interpreted as a detection result (presence/absence of methane for a positive/zero enhancement value) or as a per-pixel quantitative retrieval.

4.3.3 IMAP-DOAS

Differential Optical Absorption Spectroscopy (DOAS) describes the relationship between incident intensity for the vertical column and the measured intensity after passing through a light path containing an absorber [66]. The IMAP-DOAS retrieval incorporates optimal estimation theory to adjust the column densities of gases until there is optimal agreement between the measured and modeled radiances. It has been modified for use with AVIRIS NG [51]. For

more information on this retrieval algorithm, please see Thorpe et al. (2017).

The IMAP-DOAS algorithm retrieves a scale factor and a volume mixing ratio (VMR) for the entire column. The DOAS algorithm is designed to estimate the actual methane concentration for each pixel; therefore, the scale factor produced by the algorithm represents a value to be multiplied by the prior in order to properly scale the prior to the correct concentration. In order to get a value that is comparable with the matched filter and the synthetic image, the IMAP-DOAS results must be converted to ppm-m. To convert the units we first take the Vertical Column Densities (VCD) in units of molecule/cm^2 from the IMAP-DOAS prior. The VCD is then multiplied by the scale factor to get the actual VCD for every pixel. The VCD is then converted to ppm-m assuming a standard atmosphere. The following equation shows the VDC to pmm-m unit conversion.

$$\alpha_{ppm-m} = \frac{\alpha_{VCD} molec}{100 cm^3} * \frac{1 cm^3}{1E-6 m^3} * \frac{1 mol}{6.022E23 molec} * \frac{22.4L}{1 mol} * \frac{1 m^3}{1000L} * 1E6 ppm \quad (4.1)$$

Where α_{ppm-m} is a pixel in units of ppm-m and α_{VCD} is the vertical column density in units of molecules/cm^2 for each pixel.

4.3.4 Large-Eddy Simulation Plumes

Large Eddy Simulations (LES) model a realistic three-dimensional distribution of methane in the boundary layer [100, 101, 102]. These models were run assuming methane emitting from a point source with a stable emission rate of 500 CH_4 kg/hr and a cloud free convective atmosphere. The model was run with wind values that ranged from 1 to 10 m/s. Studies have found that the average terrestrial wind speeds range from 0 to 10.5 m/s with the majority of average wind speeds falling between 1.5 and 6 m/s [103]. Although wind speeds can be much higher, 1 to 10 m/s is a common terrestrial wind speed range found in methane studies. For

each wind speed, the model is spun up and 15 two-dimensional snapshots in time are saved. For our analysis focusing on the spatial resolution and flux rate, we picked the final snapshot for each wind speed. An example of the LES plumes at different wind speeds is shown in Figure 4.2. For our analysis on wind speed we looked at all 15 snapshots. Additional information on the model parameters, beyond wind speed, can be found in Matheous and Bowman (2016) and Matheous and Chung (2014).

The flux rate for each plume was modeled by multiplying the original plume by a scalar to change the per-pixel concentration. We modeled 34 flux rates between 50-5000 kg CH_4/hr. We also examined 24 flux rates between 10 and 250 kg CH_4/hr. The second range of fluxes allowed us to examine the lower flux rates with more detail. In two previous studies surveying methane plumes with AVIRIS NG over large areas [27, 25], the range in flux rates was 10 to 10,000 kg CH_4/hr. In this study, we are primarily focusing on identifying the minimum detectable flux rates and therefore chose to only focus on the smaller half of the previously reported ranges.

The spatial resolution was adjusted by resampling the original image with bilinear interpretation. The spatial resolution of the original LES plumes was 5 m. We tested 8 different spatial resolutions: 5, 15, 30, 45, 60, 120, 250, 500 m. Five meters is typical for AVIRIS NG if flying 5 km above the ground, and 15 m is a reasonable resolution for a airborne sensor flying at a higher elevation. Thirty, 45, and 60 m are potential ranges of spatial resolutions for satellite sensors. The recently launched PRISMA (30 m), the planned imaging spectrometer missions including EMIT(60 m), EnMAP (30 m), and the planned carbon specific missions such as Carbon Mapper and GHGsat [40, 104] have resolutions within this range. One hundred and twenty, 250, and 500 m are spatial resolution ranges for more moderate resolution instruments such as the Environment Defense Funds' (EDF) MethaneSAT. The stated satellite missions' have other qualities (SNR, spectral resolution) that may improve or hinder methane detection, so this analysis is not a review of these mission's methane detection abilities but rather an evaluation of how an imaging spectrometer similar to AVIRIS NG would perform at

different spatial resolutions.

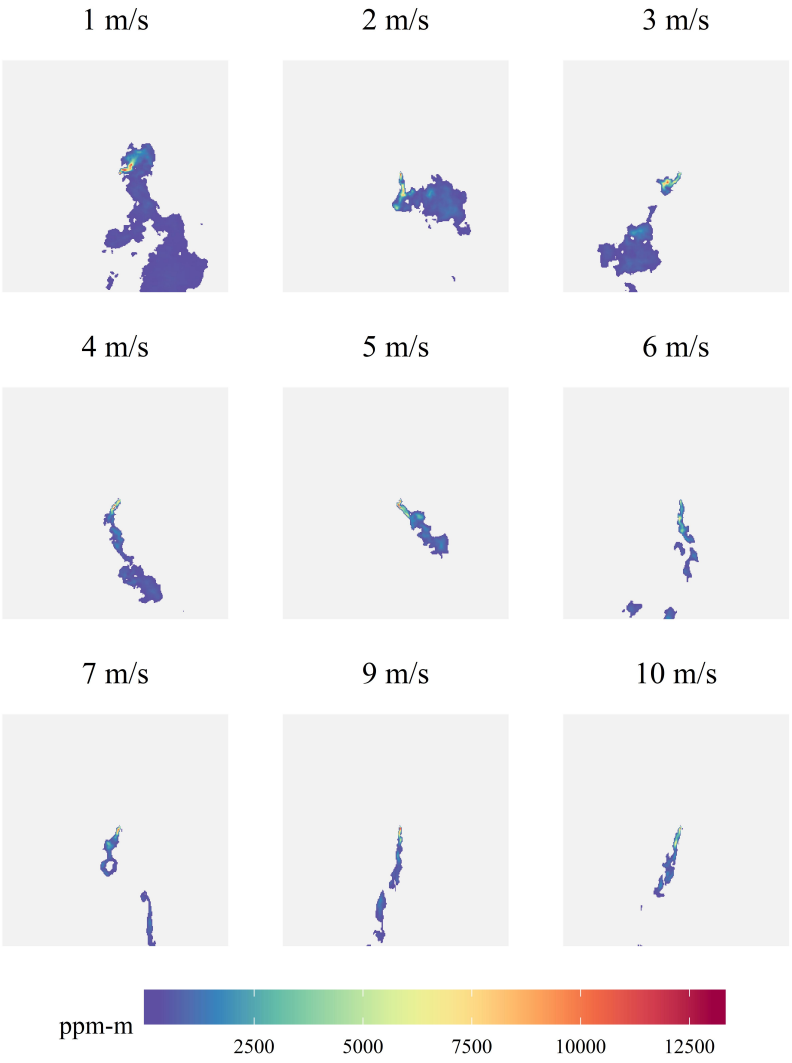


Figure 4.2: Each tile is an example of an LES plume at a different wind speed. In this example the flux rate is 500 kg CH_4/hr and the spatial resolution is 5 m. One snapshot was chosen for each wind speed, and the threshold is 400 ppm-m. Note the elongated plume shape at high wind speeds and the pooling of methane at low wind speeds.

4.3.5 Thresholds and Plume Detection

To separate the plume from the background, we applied a methane threshold to each image to filter out background noise. The best practices for determining a threshold for methane re-

trievals from imaging spectrometers have not yet been established, and often theoretical values are used to determine what the threshold should be. Here we quantitatively determined the best thresholds. Previous studies have shown that albedo can have a large influence on results [98]. We therefore looked for the best threshold for low, medium, and high albedo scenarios. We define high albedo as pixels that have a value of 2.1 μWcm^{-2}nm^{-1}sr^{-1} at 2139 nm or higher. Medium albedo are pixels between 1.3 and 2.1 μWcm^{-2}nm^{-1}sr^{-1} at 2139 nm and low albedo are pixels below 1.3 μWcm^{-2}nm^{-1}sr^{-1} at 2139 nm. In addition, we looked at different thresholds for each methane retrieval algorithm. These thresholds are evaluated, and one was selected to isolate the plume in LES images. However, the thresholds, and the threshold selection process, can also act as a guide for thresholding plumes in future work.

In order to determine appropriate thresholds, we characterized the variation in the results from the non-methane pixels and compared them to the distribution of results from the methane-enhanced pixels. We filtered the pixels into low, medium, and high albedo values as well as separating the analyses by algorithm. We then proceeded systematically from the lowest modeled methane enhancements to the highest methane enhancements (as modeled in the synthetic image) and analyzed the distribution of the results for each enhancement. We then used a Kolmogorov-Smirnov (KS) test [105] to determine if the enhanced distribution was significantly different from the background distribution at a p-value of 0.005. The value at which the distribution of the methane enhancement is significantly different from the background was the value of the threshold. It should be noted that the existence of spatial autocorrelation in the imagery may result in an over-estimate of p-values. The spatial structure in the images reduces the true degrees of freedom within the information contained in the simulated scenes, and the number of pixels therefore probably overestimates the number of independent observations. Nonetheless, this approach does provide a systematic evidence-based method for determining thresholds.

4.3.6 Calculated Flux Rates

For every plume the parameter of interest is the flux rate. Therefore, for each plume we calculated a flux rate which is referred to as the calculated flux rate. For this study we used a simple flux rate equation. Equation 4.2 shows the simple flux calculation.

$$flux = \frac{IME}{l}u \tag{4.2}$$

Where l is the length of the plume (m), u is the wind speed (m/s) and IME is the Integrated Mass Enhancement (kg). We calculated an Integrated Mass Enhancement (IME) for each plume by multiplying the area of each pixel (m^2) by the methane value (kg/m^2) and summing all of pixels in the plume (Equation 4.3).

$$IME = k\sum_{i=0}^{n}\alpha(i)S(i) \tag{4.3}$$

where $\alpha(i)$ is the methane value in ppm-m for the ith pixel in the plume with a pixel area of $S(i)$. The constant k is used to convert to methane mass units. The length is measured from the point of origin or the source to the furthest point downwind in the contiguous plume. In this study, the plume length was calculated by creating a convex hull around the area of the plume. We then calculated the Euclidean distance between the two furthest away points on the convex hull. Figure 4.3 shows an example of the plume length measurement. This method works well for elongated plumes; however, this method is less accurate for highly concentrated plume, i.e. plumes associated with low wind speeds.

The majority of the equation for the flux rate is a ratio between the IME and the plume length. The plume length and the IME are the two variables that are calculated directly from the plume, and therefore play an integral role in quantifying the plume. Ideally as the thresholds for detection sensitivity change, the IME and the plume length would change at a similar rate

to produce a consistent flux estimate. This makes the calculated flux a good metric of detection ability because it combines the IME and the plume length.

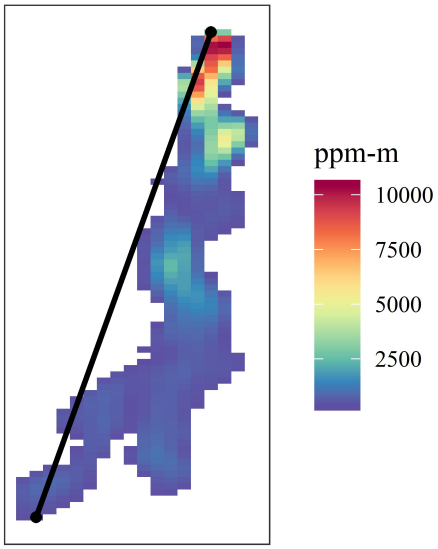


Figure 4.3: An example of the plume length measurement. This plume has a spatial resolution of 5 m, a flux of 500 kg/hr, and a wind speed of 9 m/s with a 400 ppm-m threshold. The black line shows how to measure the distance from the point of origin (where there are higher methane values) to the furthest downwind point on the plume. The measured length is 561.65 m, the calculated flux is 657.05 kg/hr.

4.4 Results

4.4.1 Thresholds

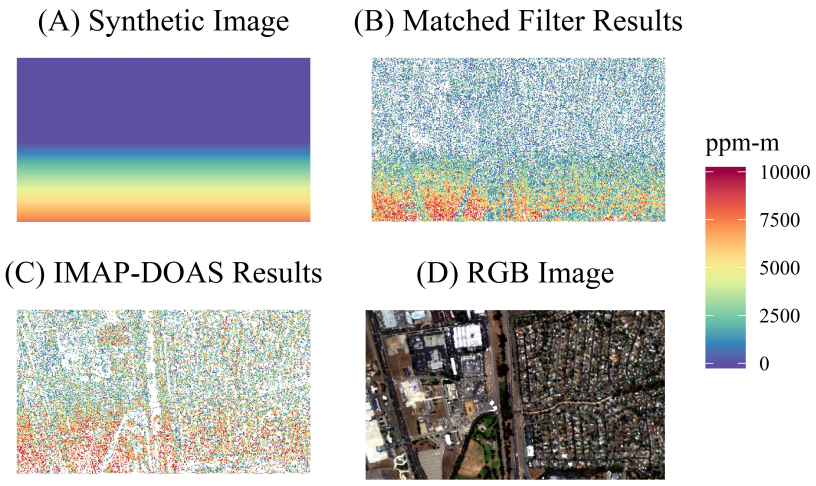


Figure 4.4: The synthetic image enhancement (A), results from the matched filter (B) and IMAP-DOAS algorithm (C), and an True color image of the background (D). The data from this figure is used to determine the thresholds.

The results from the Matched Filter and the IMAP-DOAS algorithms are shown in Figure 4.4. These results provided inputs for the threshold analysis. Note that the pattern in the synthetic image holds for both of the retrievals, but the results are fairly noisy. This is typical of an AVIRIS-NG methane retrieval. Also note that the results differ between algorithms and that the results are clearly influenced by the underlying landcover. Therefore, we separated the thresholds by algorithm and albedo.

The KS tests reveal four threshold values between the matched filter, IMAP-DOAS, and the three different albedo levels. The p-values of interest for the KS tests are reported in Table 4.2. Figures 4.5 and 4.6 show examples of the distributions used to run the KS tests. The distribution of the enhanced pixels (blue) become visually more distinct from the distribution of the background pixels (black) as the enhancement value increases. The background pixels are any pixels that do not have a modeled methane enhancement. For example, in Figure 4.4, this would be the top half of the images. For the IMAP-DOAS algorithm results from high albedo pixels, the enhanced values showed a significant deviation from the background values at 400 ppm-m. For the medium albedo results, the enhanced distribution is significantly

different from the background at 600 ppm-m, and for the low albedo results the threshold value is at 2200 ppm-m.

The matched filter at the high albedo and the medium albedo cases both show significant deviation from the background at 600 ppm-m. Two hundred ppm-m also has a significant p-value with the high albedo pixels, but the plotted results in Figure 4.6 show that the 200 ppm-m distribution is significantly less than the background and therefore does not count as a value with a methane enhancement that is above the background. For the low albedo case, the matched filter did not show a significant deviation from the background until 1000 ppm-m.

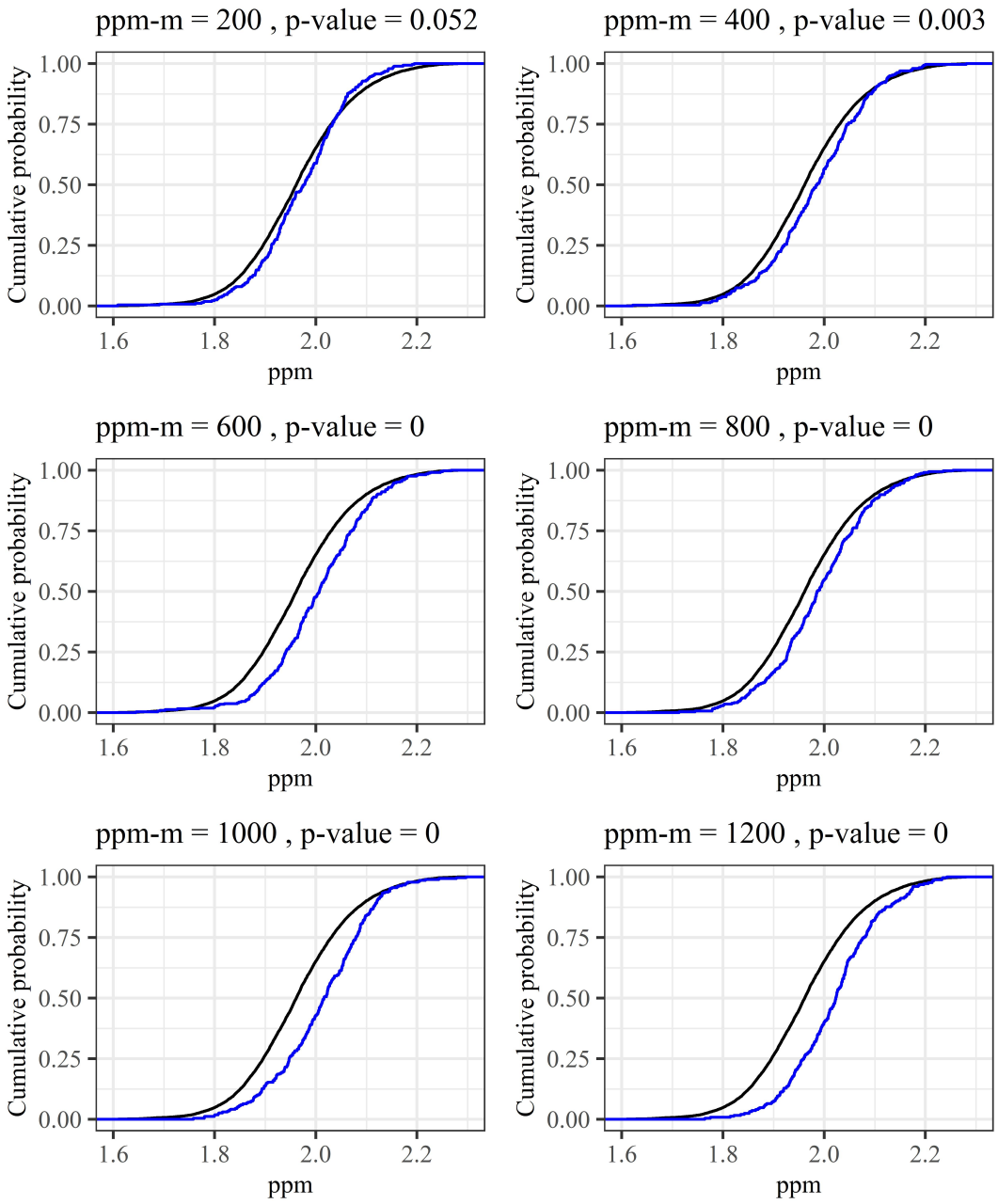


Figure 4.5: Each plot shows an empirical cumulative distribution function (ECDF) for the high albedo IMAP-DOAS results. The black line is the ECDF for the background pixels, and the blue line is the ECDF for each enhancement. The enhancement value is listed in the title of each tile. As the enhancement gets larger, the two ECDFs become more distinct. Note that the x-axis is ppm, the original IMAP-DOAS results are reported in ppm, and the original values were used in this analysis and later converted to ppm-m.

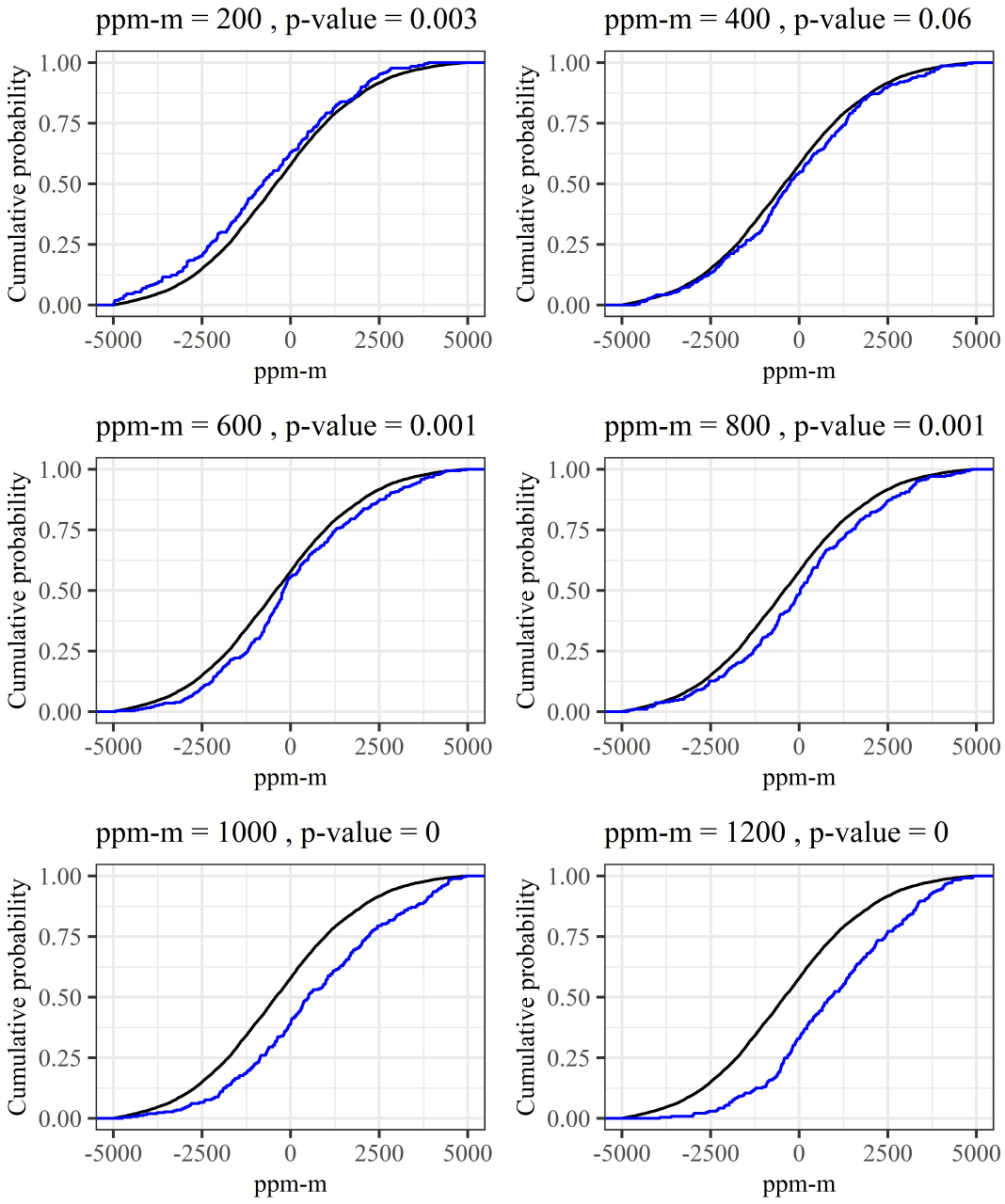


Figure 4.6: Each tile is an empirical cumulative distribution function (ECDF) for the high albedo matched filter results. The black line is the ECDF for the background pixels and the blue line is the ECDF for each enhancement. The enhancement value is listed in the title of each tile. As the enhancement gets larger, the two ECDFs become more distinct.

Table 4.2: MODerate resolution atmospheric TRANsmission (MODTRAN) inputs for simulating the atmosphere from the aircraft to the top-of-atmosphere (TOA).

	Methane ppm-m	Matched Filter	IMAP-DOAS
High Albedo	200	0.003**	0.052
	400	0.06	0.003*
	600	0.001*	0.0*
Medium Albedo	400	0.081	0.082
	600	0.0*	0.002*
Low Albedo	1000	0.003*	0.083
	1200	0.00	0.146
	1400	0.0	0.011
	1600	0.0	0.327
	1800	0.0	0.603
	2000	0.0	0.111
	2200	0.0	0.0*

$*p < 0.005$
** p is significant, but the distribution of the pixels with enhancements is lower than the background distribution.

The results indicate that there is no one best threshold that works for all scenarios. Determining a threshold is dependent on the methane retrieval algorithm, the relative albedo of the scene, and the user preference. The results also highlight some differences between the two retrieval algorithms. For the high albedo analysis, the IMAP-DOAS algorithm is much more sensitive to the methane enhancement at a lower threshold. For the medium albedo analysis, the two algorithms performed similarly. For the low albedo analysis, the matched filter is able to identify a methane enhancement at a much lower level than the IMAP-DOAS algorithm. These results indicate that the matched filter has a lower threshold in low albedo scenarios while the IMAP-DOAS has a lower threshold in high albedo environments.

In the next stage of our analysis, we apply a threshold to the LES plumes. The LES plumes do not have background noise that needs to be filtered out as it would need to be done with a plume retrieved from an image. Therefore, for this study we look at how each of the four possible thresholds performed when calculating a flux rate with the LES plumes. Figure 4.7 shows

the calculated flux plotted against the modeled flux with the various wind speeds displayed in the color scale for each of the identified thresholds. The 400 ppm-m threshold has the highest correlation (R) value, followed by 600, 1000, and 2200 ppm-m. The correlation coefficient or slope for all thresholds is one or close to one. In general, all of the thresholds had similar results: however, the 400 ppm-m threshold had the best R value. For the latter part of this analysis we chose to use the 400 ppm-m threshold. The 600 ppm-m threshold is chosen as the ideal threshold more times; therefore, if we were to be using retrievals from AVIRIS-NG rather than LES plumes, 600 ppm-m would be the better threshold. However, in the sensitivity analysis we use LES plumes, which are an idealized version of the AVIRIS-NG plume; therefore the lower and more accurate threshold is better.

Also important to note in Figure 4.7 is the distribution of the results in regards to the wind speeds. The higher wind speeds (plotted in red/orange) tend to be above the one-to-one line, revealing a pattern of flux overestimation. The low wind speeds (purple/blue) tend to be below the one to one line showing a pattern of flux underestimation. Additional analysis into the wind speed is reported in the next section.

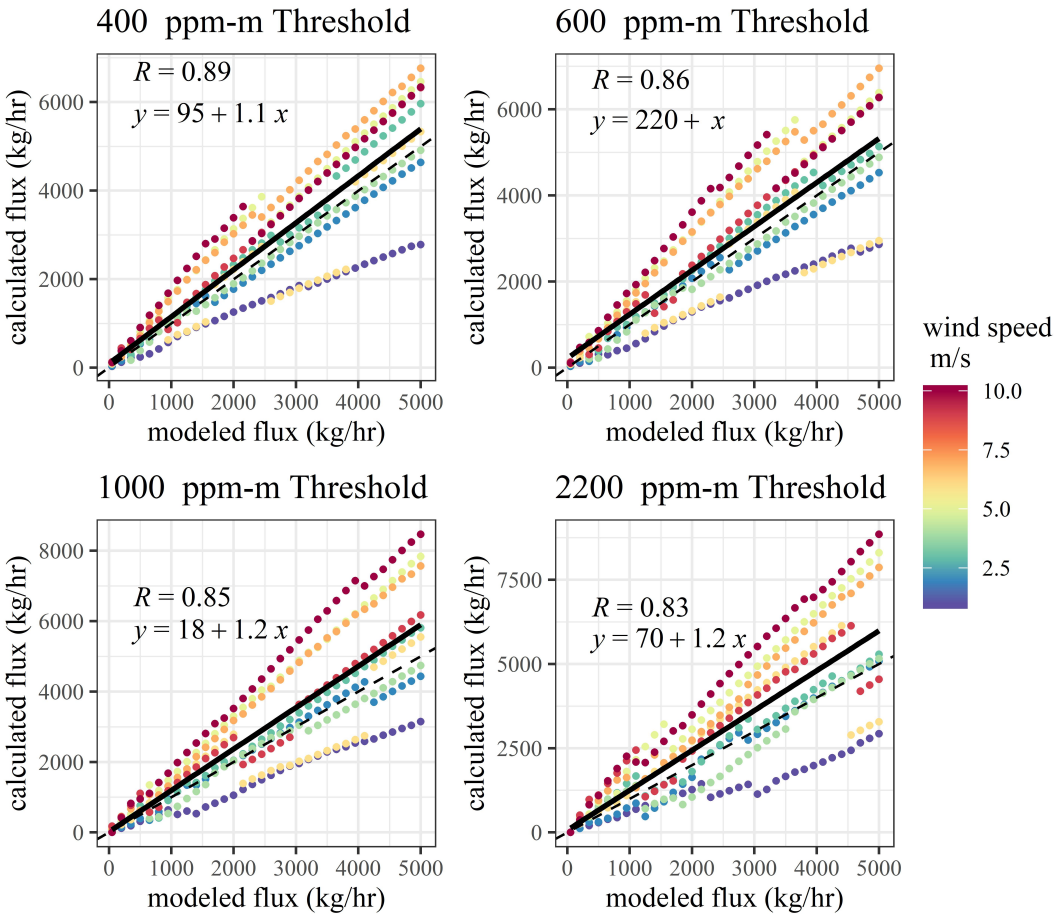


Figure 4.7: The modeled flux is plotted against the calculated flux for every flux rate and wind speed at 5 m spatial resolution with a 400, 600, 1000, or 2200 ppm-m threshold. The dashed line in all plots is the one to one line, the black solid line is the regression line. The R, slope, and intercept are shown on each plot. The colors represent different wind speeds.

4.4.2 Spatial Resolution and Wind Speed

Figure 4.8 shows the calculated fluxes from the LES plumes for every wind speed and flux rate at each spatial resolution. In addition, the mean and standard deviation of the pixel count (number of pixels in each plume) is displayed for each spatial resolution plot. The left column of plots are the finer spatial resolution plots and therefore the analysis focuses on the lower flux rates. The right column panels are the coarser spatial resolution plots, and therefore focus on a higher range of flux rates. Every pixel represents a plume, the colors represent the calculated

flux rates, and the gray pixels are plumes where the entire plume was below the 400 ppm-m threshold. The mean pixel count is included because it is a good metric of the level of detail in the plume at that resolution. Generally, in remote sensing, as the spatial resolution becomes coarser there are fewer pixels covering the same area on the ground, and therefore less detail or resolution. However, it is still important to note when a calculated flux is based off of one pixel or 150 pixels. The pixel count, in conjunction with the calculated flux gives the most accurate picture of detectability at different spatial resolutions and wind speeds.

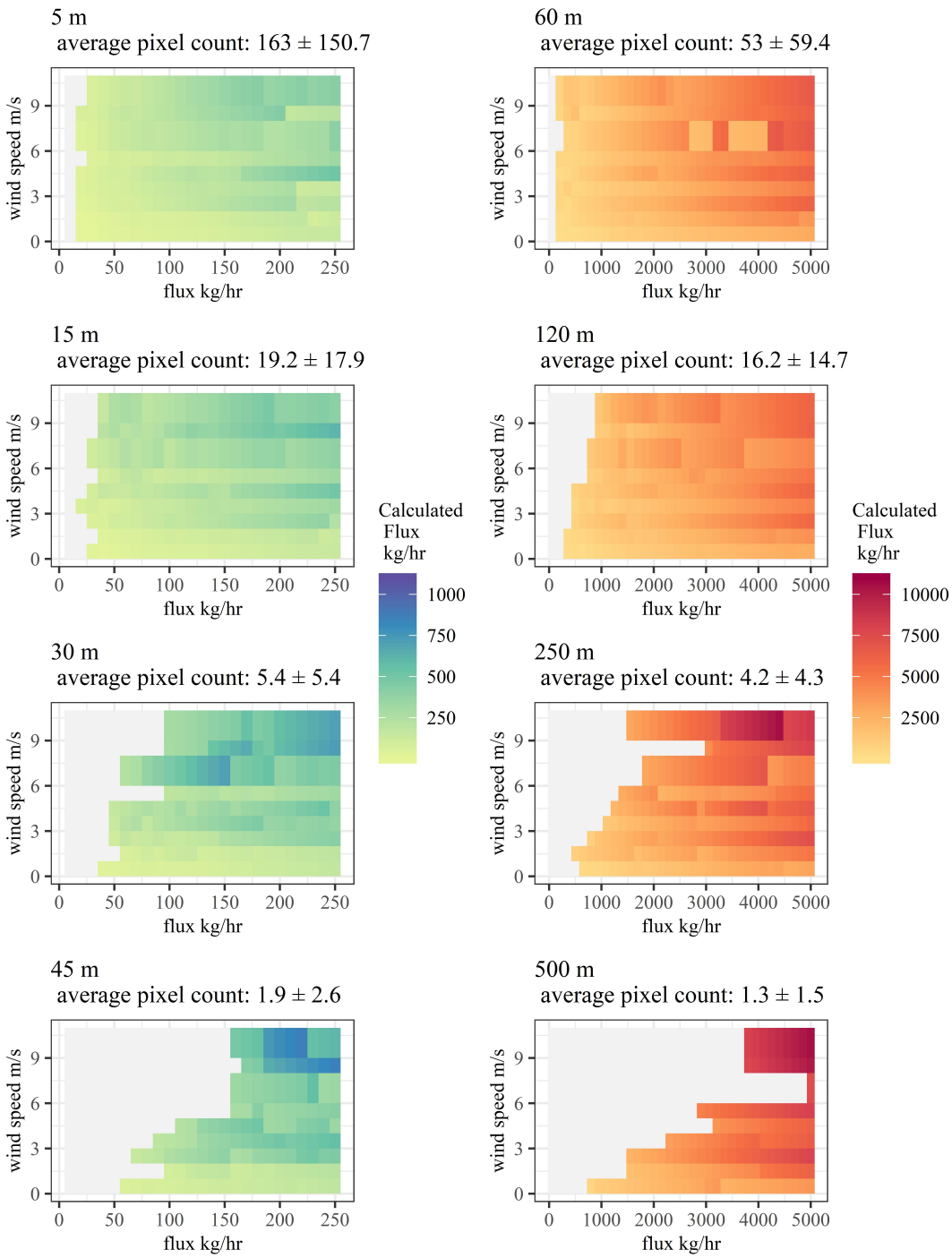


Figure 4.8: Each plot shows the calculated flux rate for every modeled flux rate (x-axis) and wind speed (y-axis) at the spatial resolution listed above it. Also listed in the plot title is the average pixel count. The left column of plots are the fine spatial resolution plots which share the same x-axis (0 -250 kg/hr) and scale bar. The right column of plots are the coarse spatial resolution plots. They also share the same x-axis (0 -5000 kg/hr) and scale bar.

Spatial Resolution

A noticeable trend in Figure 4.8 is the reduction in the average pixel count with coarsening spatial resolution. As expected, the coarsening spatial resolution causes the pixel count to decrease. This means that at coarse spatial resolutions there are less data used to calculate the flux rate. The calculated flux rate, which uses the IME and plume length and therefore is sensitive to both, tends to increase with a coarser spatial resolution. For example, in the left column of Figure 4.8 the maximum calculated flux for the 45 m plume is about 1000 kg/hr when the maximum modeled flux is 250 kg/hr. In contrast, the maximum calculated flux for the 5 m plume is about 500 kg/hr. For the right column the maximum calculated flux rates for the 500 m plume were about 10,000 kg/hr and the maximum calculated flux rates for the 60 m plume were about 7000 kg/hr. The maximum modeled flux rate for both was 5000 kg/hr. In both cases the coarser spatial resolution overestimates the flux rate. The increase in calculated flux is due to a change in the ratio between the IME and the plume length. With an overestimation of the flux rate, the IME is either too small or the plume length is too long to accurately calculate the flux rate. In addition, with coarsening spatial resolution, more plumes become undetectable, meaning there were no pixels above the threshold. In Figure 4.8, as the spatial resolution coarsens, there is an increase in the gray area in each plot. From this we can conclude that coarsening the resolution makes detection more difficult and increases the error in the calculated flux.

Figure 4.9 distills the results from Figure 4.8 regarding spatial resolution. The lines represent the lowest flux rate at which there are pixels above the threshold. The 1 m/s and 10 m/s (blue and red lines respectively) do this for the stated wind speeds. The max line finds the flux rate at which the plume has at least one pixel above the threshold for all wind speeds. The min line is the flux rate where at least one wind speed displays a pixel above the threshold. Figure 4.9 shows that detection became more difficult with coarse resolution. It also shows the

minimum modeled flux rate for which a plume is detectable at each spatial resolution (note the non-linear x-axis). Without considering other factors, such as SNR or spectral resolution, the minimum detection ranges for the spatial resolutions are as follows: For 5 – 15 m the minimum detection is between 20-30 kg CH_4/hr, the 30-60 m minimum detection is between 40-210 kg CH_4/hr, and for 120-500 m the minimum detection is between 220 – 5000 kg CH_4/hr.

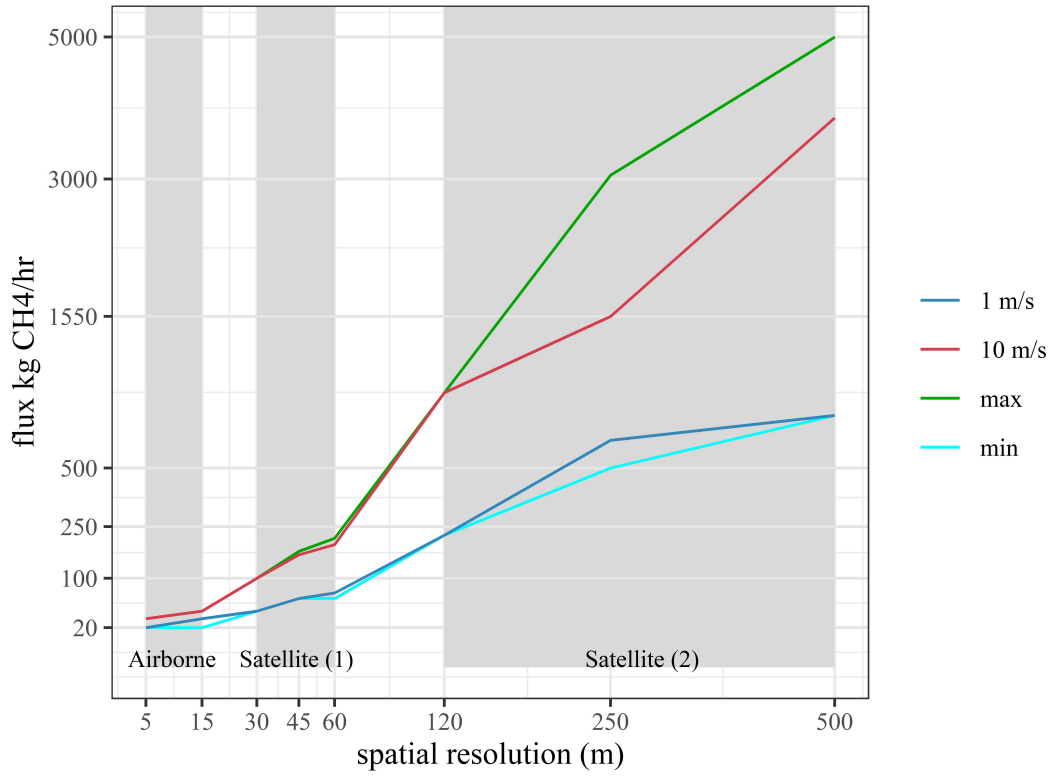


Figure 4.9: For every spatial resolution the minimum flux detectable with a 400 ppm-m methane enhancement. The blue line is for 1 m/s, and the red line is for 10 m/s. The green line is maximum value, or the flux value at which all wind speeds have a detectable plume. The cyan line is the minimum value, or the flux value where at least one wind speed shows a detectable plume. Satellite (1) represent imaging spectrometers with a 30-60 m spatial resolution, and Satellite (2) represent imaging spectrometers with a 120 to 500 m spatial resolution.

Wind Speed

Apart from spatial resolutions, Figure 4.8 also shows how detectability and the calculated flux change with wind speed. In general, we see that as the wind speed increases, more plumes

become undetectable. This is because as the wind speed increases, the plume spreads out over a larger area and causes the per-pixel methane values to decrease. This in turn results in plumes where all the pixels are below the threshold and are therefore undetectable. Figure 4.9 shows that the minimum detection limits are much higher for 10 m/s wind speed than for 1 m/s wind speed.

Wind speed can also influence the accuracy of the flux calculation. Figure 4.10 shows the mean and standard deviation of the percent error for the calculated flux at each wind speed. The mean and standard deviation of the percent error for each wind speed is calculated from 15 snapshots at each wind speed and from flux rates between 50 and 5000 kg CH_4/hr. The lowest wind speed (1 m/s) causes the flux rate to be underestimated. The moderate wind speeds (2 – 4 m/s) produce the most accurate results. The high wind speeds (5 m/s and higher) cause an overestimate of the flux rate. Figure 4.10 shows 5, 30, and 250 m as representatives of each spatial resolution category. As the spatial resolution coarsens, the variation in the percent error increases, but the overall pattern remains the same.

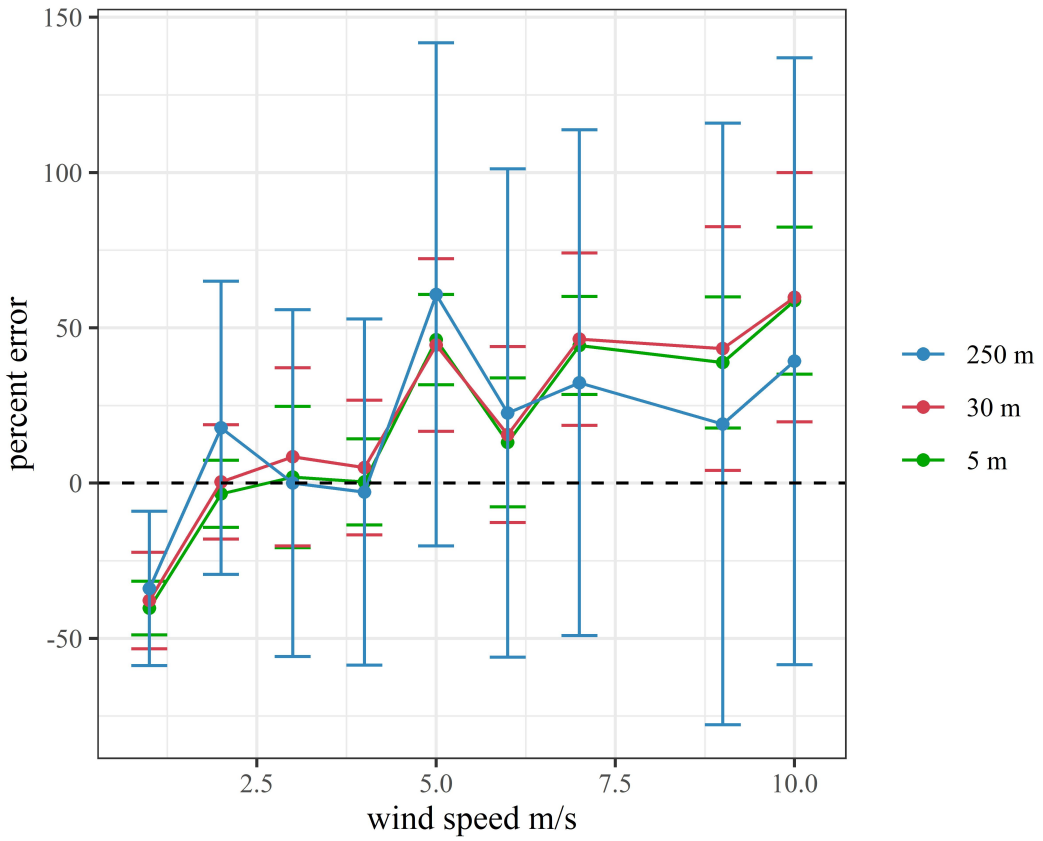


Figure 4.10: For every windspeed (x-axis) the percent error between the calculated flux rate and the modeled flux rate. The error bars are one standard deviation. Each line represents a different spatial resolution. The dashed line is at zero and represent the ideal results.

4.5 Discussion

4.5.1 Thresholds

In this study, we identified four thresholds using a KS test (400, 600, 1000, and 2200 ppm-m). Here, we discuss these thresholds and what they tell us about the retrieval algorithms. We then discuss the thresholds in the context of previous studies. Finally, we discuss the threshold used in this study to isolate the plume in the LES images.

One important result from our study is that IMAP-DOAS tends to perform better at high albedos, while the matched filter tends to perform better at low albedos. Hence, 400 ppm-m

was the high albedo IMAP-DOAS threshold and 600 ppm-m was the high albedo matched filter threshold. The IMAP-DOAS algorithm has a slightly lower threshold than the matched filter which indicates the IMAP-DOAS is slightly more sensitive to low methane values at high albedos. For the medium albedo pixels, both algorithms had a 600 ppm-m threshold. There was no change in the matched filter threshold between the high and medium albedo, showing that the matched filter is less affected by the albedo than the IMAP-DOAS algorithm. The matched filter low albedo threshold was 1000 ppm-m, and the IMAP-DOAS threshold for the same albedo range was 2200 ppm-m. The matched filter threshold is lower, indicating that it is less sensitive to low albedos than IMAP-DOAS. An important advance, demonstrating, for the first time, the ability to use an empirical test to automatically identify these values.

Applying thresholds to this type of data is standard practice. To date, there are two major studies that have applied these methane retrieval algorithms to map methane over a large area with AVIRIS NG. One study investigated plumes in the Four Corners region of the United States and used a 200 ppm-m threshold to segment plumes [25]. The other study looked at all methane sources in the state of California and used a 1000 ppm-m threshold to segment plumes [27]. While the 200 ppm-m threshold is lower than the lowest value identified in this study, the 1000 ppm-m is a threshold identified in this study. These results indicate the thresholds chosen in previous studies were reasonable, but not rigorously tested. From the analysis, we saw that the correlation between the calculated flux and the modeled flux can change with different thresholds. This indicates the necessity to have a concrete methodology to determine an appropriate threshold. This study offers a methodology to determine the thresholds or provides a range of potential thresholds. These thresholds can be used in future studies or this methodology can be used to determine future thresholds.

In this study, we apply one threshold to the LES plumes. The LES plumes are an idealized representation of a methane retrieval from an imaging spectrometer. An actual methane plume retrieval has noise in the background, it has spurious signals (also known as false positives),

and it is influenced by the underlying land cover, which can cause changes to the perceived plume shape. In both a real methane retrieval and an LES plume, if the threshold is too high, then too much of the plume is filtered out. However, in a real retrieval, if the threshold is too low, then spurious signals can be introduced into the plume. In contrast, if a threshold is too low in the LES plumes, no spurious signal is introduced. The threshold and the threshold choice are much more important for real images than they are for LES images. For this analysis we felt confident in choosing the threshold that produced the best calculated flux results (400 ppm-m). However, other factors, such as albedo and primary retrieval algorithm, would need to be considered when selecting the threshold for a real image. In fact, had we been using real images, a 600 ppm-m threshold may have been better.

4.5.2 Spatial Resolution

Spatial resolution plays a major role in determining the size of plumes that can be detected and accurately mapped with imaging spectrometers. The main driver of the lack of detection with spatial resolution is the reduction in the per-pixel methane value with coarsening resolution. As the spatial resolution becomes coarser, the plume becomes less distinct and the per-pixel methane value decreases. As the per-pixel methane value decreases, more pixels end up below the detection threshold (400 ppm-m). A possible solution for decreasing the minimum detectable flux in coarse spatial resolution scenarios is to reduce the threshold. The distribution of the background pixels should also decrease with coarsening resolution, and there should be less noise. This should make plumes with a lower per-pixel ppm-m value stand out. Therefore, decreasing the threshold will allow more pixels to be included in the plume. Not only did the minimum detectable flux increase with coarsening spatial resolution, but we also found that the calculated flux rate increased with increasing spatial resolution. This is due to the IME being too small in relation to the plume length or the plume length being too long

in relation to the IME. Again, it is possible that reducing the threshold could help solve this problem, but additional experimentation with determining thresholds at coarsening resolutions will be necessary to verify this hypothesis. In general, we can conclude that coarsening spatial resolution causes plumes to become less detectable and the flux result to be less accurate.

The effect of spatial resolution is especially important because it is one of the features that distinguishes different sensors and it can determine what types of emissions a sensor can target. The variety of spatial resolutions represented in this study are similar to the spatial resolutions in our current and future field of sensors. It is critical to note that each sensor also has different SNRs and spectral resolutions which can significantly change the per-pixel sensitivity to methane. This study did not provide an analysis of the sensitivity of any specific sensor but rather an analysis for an ideal imaging spectrometer at different spatial resolutions. However, the analysis done at the 5 m spatial resolution is a similar resolution to AVIRIS NG and other airborne sensors currently in operation. The spatial resolution of AVIRIS NG is directly correlated to the height of the plane. In the event the plane flies at a much higher altitude, the spatial resolution could be as coarse as 15 m. Previous studies have identified 10 kg CH_4/hr as the minimum detection limit for AVIRIS NG [27]. From our analysis, we can conclude that airborne flights have the capability to target smaller plumes on the order of tens of kg/hr or larger. Plumes from sources with flux rates below 100 kg/hr make up a little less than half of known point source plumes [27]. Although it should be noted this statistic is from two AVIRIS NG campaigns and therefore does not take into account plumes smaller that 10 kg CH_4/hr. Nevertheless, a sensor with this resolution range should, therefore, capture more plumes than a coarse resolution sensor.

The future generation of imaging spectrometers that include PRISMA, EnMAP, EMIT, and SBG are all in the 30 to 60 m range. GHGSat and the planned Carbon Mapper are also in the 30-60 m range. Although this analysis does not specifically test the capabilities of these sensors, an ideal imaging spectrometer with a 30 to 60 m spatial resolution has the ability to target sources

with plumes on the order of 100s of kg/hr or larger. Previous studies have identified 100 kg CH_4/hr as the minimum flux rate detectable by a spaceborne imaging spectrometer [28, 29], and our findings agree with this limit. According to the data from previous AVIRIS NG campaigns, plumes 100 kg/hr or larger make up a little over half of the known plumes but contribute well over 75 percent of total emissions [27]. Although sensors with this range of resolutions may miss the small plumes, they will capture the majority of point source emissions. MethaneSAT, a methane-specific satellite from the Environmental Defense Fund has spatial resolution of 400 x 100 m. Again, we did not test this specific sensor, but if an imaging spectrometer were to have a spatial resolution between 250 and 500 m, the minimum plume range would be somewhere between 250 and 5000 kg/hr. Therefore, this range of sensor could detect a small fraction of plumes. However, plumes at 500 kg/hr and larger represent about half of all emissions. Therefore this sensor may be able to detect plumes know as super-emitters, or the handful of plumes that represent the majority of emissions.

4.5.3 Wind Speed

Wind is the driving factor in determining the shape of the plume and is also a critical parameter in the flux calculation. In this analysis, we isolated the effects of the wind speed on the plume detection/quantification in order to understand what the most desired wind speeds are for calculating flux rates. In general, the minimum detection limit increases with increasing wind speed. In Figure 4.9 we see that the 1 m/s wind speed has a significantly lower detection limit than the 10 m/s wind speed. As the wind speed increases, the methane becomes more dispersed, and the per-pixel methane concentration decreases, causing more of the pixels to fall below the threshold and therefore become indistinguishable from the background. Besides making the plume less detectable, it also artificially shortens the length of the plume. For the flux calculation, not only does the plume need to be detected, but there also needs to be an

accurate measurement of the plume length and the IME.

Low wind speeds cause the plume to form a non-linear shape, which can make determining the downwind direction and plume length difficult. For this type of flux estimate to work properly, there needs to be some wind to elongate the plume and make the length calculation clear. However, there also needs to be enough methane above the threshold to get an accurate IME. Therefore moderate wind speeds are best for flux estimations. In both Figure 4.7 and Figure 4.10 we see that moderate wind speeds result in the most accurate flux rates. This may be because as the wind speed increases, the plume becomes more spread out and the end falls below the threshold. This results in the the length of the plume becoming too short with respect the IME. As a result, the IME increases at a faster rate than the plume length, and the flux rate tends to get over estimated. In the results, we see that wind speeds at 5 m/s and above overestimate the flux rate. At 1 m/s we see the opposite phenomena: the plume length appears to be too long for the associated IME, causing the flux rate to be underestimated. Thus, between 2 and 4 m/s, the ratio between the IME and the plume length results in the most accurate flux estimations. This pattern was also noted in Varon et al. (2018) [76]. In this case the authors used a similar method to calculate the plume but used an effective wind speed instead of the observed wind speed. They determined the effective wind speed by building an empirical relationship between the observable wind speed and a back calculated wind speed. By applying this empirical relationship to the observed wind speed before calculating the flux they were able to improve the accuracy of the flux estimation at high wind speeds. This is a possible solution to the error pattern observed in the results of this study. However, it is important to note that Varon et al. (2018) also used LES plumes, therefore additional work is needed to determine if the pattern observed with the wind speed is a true phenomenon or a function of the LES.

Wind speed has long been a large source of error in calculating flux from static plume images. The error typically comes from uncertainties regarding the wind speed at the time

of the image acquisition. The average error associated with unknown wind speeds at time of acquisition, when using modeled data, is $\pm$ 19 percent [27]. However, here we show that even with perfect knowledge of the ambient wind speed, the wind inserts a different type of uncertainty. The wind speed can change the apparent size and shape of the plume which in turn affects the accuracy of the measured plume length and IME. For 1 m/s wind speed the mean percent error was between -33 percent and -40 percent depending on the spatial resolution. For the 2 – 4 m/s wind speeds, the mean percent error is between -3 percent and 17 percent error. For the 5 m/s wind speed and higher the mean percent error was between 13 and 60 percent depending on the spatial resolution (Figure 4.10). This type of error is derived from errors in measuring length and IME. Novel methods to deduce the wind speed and methods of calculating flux rate that are less sensitive to wind speed may be necessary to reduce the error introduced into the flux estimate from wind. For example in satellite-based cloud and precipitation analyses, rapidly repeated observations of thermal infrared radiation are used to infer wind speeds. Similar approaches might be feasible, at least for space-borne monitoring systems.

4.6 Conclusion

We used synthetic images to develop and demonstrate a useful empirical approach to identifying detection thresholds, based on KS goodness-of-fit tests. We identified thresholds for the two main methane retrieval algorithms at different albedos. A 400 ppm-m threshold was then identified as the best threshold for high albedo scenes with the IMAP-DOAS algorithm. This threshold produced the highest R value for the modeled versus calculated flux estimates and was therefore used throughout the study. We then applied the threshold to LES plumes in order to understand the sensitivity of wind speed, flux rate, and spatial resolution on detection and calculated flux. Specifically, we sought to understand the minimum detection limits for

different spatial resolutions and wind speeds and to understand the effect of wind speed on the calculated flux.

In general we found that coarsening spatial resolution caused plumes to become less detectable and for the calculated flux to be less accurate. We found that for imaging spectrometers with a 5 – 15 m spatial resolution, the minimum detection was between 20-30 kg/hr. For the 30-60 m resolution, the minimum detection was between 40-210 kg/hr. And for the 120-500 m resolution, the minimum detection was between 220– 5000 kg/hr. As more sensors become operational and as other sensors are designed, understanding the detection limits due to spatial resolution can help define what types of methane emissions a certain sensor can map. It can also help guide sensor development to target a specific type of methane emissions. We also found that moderate wind speeds (2-4 m/s) have the most accurate calculated flux rates. We found the mean percent errors associated with low wind speeds (1 m/s) were between -33 and 40 percent, while the mean percent errors for moderate wind speeds (2-4 m/s) were the lowest, with ranges between -3 and 17 percent. The high wind speeds (>5 m/s) caused the largest errors, with average percent errors between 13 and 60 percent, depending on the spatial resolution. Wind speed can introduce error in the results when there is too little wind to form a distinct plume or when there is too much wind and the plume is blown out.

As more imaging spectrometer data becomes available and new sensors are developed, it is crucial that we understand how factors such as wind speed, flux rate, and spatial resolution affect detection of methane emissions. This study quantitatively identified the size of methane plumes visible at different spatial resolutions and thereby what percent of emissions can be mapped with different satellites. This study also highlighted an important source of error associated with wind speed. With these results we can now improve the accuracy of methane plume quantification and guide future sensor development. While methane retrievals will remain challenging, our results indicate that a space-based 30 to 60 m imaging spectrometers should be capable of detecting the largest emitters that account for the bulk of methane emissions.

Chapter 5

Conclusion

The overall goal of this research was to use synthetic images to test the sensitivity of methane mapping with imaging spectrometers to a variety of factors. This dissertation looked at the effects of albedo, land cover, wind speed, spatial resolution, retrieval thresholds, and SNR on airborne and satellite mapping with imaging spectrometers. Here I will review the key finding of each chapter, I will talk about the role this research can play in current and future work, and I will discuss future directions.

In Chapter 2, I used synthetic AVIRIS-NG images to test the effects of land cover and albedo on methane retrievals with the IMAP-DOAS algorithm. The synthetic image allowed for control over the methane concentrations, albedo, and land cover, as well as other atmospheric variables. Overall, I found excellent agreement between the modeled methane and the IMAP-DOAS results. I found that the most accurate retrievals were over soils and paved surfaces due to their high SWIR albedo. Conversely, I found that surfaces with low SWIR albedos (below 0.10 μWcm^{-2}nm^{-1}sr^{-1} at 2139 nm) caused higher error in the retrieval results. The low albedo surfaces include green vegetation and water. Confusers also had higher error due to the absorption features in the 2200-2400 nm window. Most importantly I quantitatively showed that changes in the surface can significantly affect our ability to retrieve the column

concentration of methane accurately.

In Chapter 3, I expanded the use of synthetic images to test the potential to use future Earth observing satellites such as EMIT or SBG to map and measure methane plumes. I showed that point source methane emissions from the energy, agriculture, and waste sectors will be detectable from space. Also in this study, I varied the SNR and spatial resolution of the synthetic satellite scenes and concluded that spatial resolution, more than SNR, was the driver of detectability. I concluded that a satellite system will be able to map and quantify methane plumes from sources with fluxes as small as 100 kg/hr.

Lastly in Chapter 4, I looked more closely at the effect of spatial resolution as well the effects that wind speed and flux rates have on methane detection. Again, I utilized synthetic images to quantitatively determine methane detection limits and thresholds. I then applied the thresholds to Large Eddy Simulations. I found that coarsening spatial resolution inhibited methane detection and accurate quantification of flux rates. I also found that low wind speed and very high wind speed resulted in larger errors in the flux estimation than moderate wind speeds.

This research is currently being applied to use imaging spectrometers for methane mapping and is informing the design of future methane specific imaging spectrometers. Most notably, the work done in Chapter 3 has spurred the use of imaging spectrometers not designed for methane mapping to do just that. In Chapter 3, I focus on EMIT and SBG, two future missions. Although theses missions are not yet operational, researchers involved in both projects are aware of the potential use for mapping methane and are willing to use the instrument to collaborate with the gas mapping community. In addition, other imaging spectrometers that are currently becoming operational, such as PRISMA, have already been used to map a few methane plumes. Most importantly, thanks in part to this work and the work of many co-authors, missions specifically for gas mapping are being planned. Most notable is the Carbon Mapper, a joint mission with JPL, Planet Labs, and the State of California. Already my work

has provided support for modeling features as the sensor is designed and planned.

A methane specific imaging spectrometer on a satellite platform will have an unparalleled impact on our ability to constrain localized point source methane plume. In addition it will allow us to study super-emitters in a way that has never before been done. Currently, the airborne imaging spectrometers do not have the spatial nor temporal coverage to measure all known sources. Moving to a satellite platform will increase the spatial resolution from a few regional sites to practically global coverage. Areas such as fracking sites, international oil and gas infrastructure, and international landfills can be monitored and the emissions can be directly linked to their sources. This will provide information on the true number of super emitters and their locations. The improved temporal resolution will also help to understand the persistence versus intermittence of these large plumes. In addition, with repeat coverage of areas we can also help to improve the sensitivity to smaller plumes. while one methane enhancement could be overlooked as an error, repeat enhancements would improve confidence that the detection is real.

Beyond expanding applications and new sensor design, my work has provided a better idea of what types of emissions we can detect and how imaging spectrometers can be integrated into the carbon monitoring system. The work done in all three chapters helped to analyze the performance of the methane retrieval algorithms, thereby building confidence in the accuracy of this type of methane mapping. In addition, the sensitivity analysis helped identify the scenarios where methane retrievals are least and most accurate. By building confidence in the results, we can now firmly advocate for imaging spectrometers to be used by industry, government, and other interested parties to map methane. We can also begin collaborating with other carbon scientists to better understand methane emission patterns. More importantly the work in all three chapters helped to define detection limitations for this type of methane mapping. By defining these limitations, we know what type of methane plumes imaging spectrometers can and cannot detect and under what conditions. We can show how imaging spectrometers can

be used with other gas mapping satellite missions and other airborne missions to get the most complete picture of methane emissions.

This research will also contribute to methane mitigation efforts. By examining the sensitivies and quantifying limitation we can now build a frame work to use this data to control emissions. Thanks to this work, the limitations of various instruments have been quantified, so now an efficient plan to use different instruments in tandem can be implemented for monitoring efforts. For example, a satellite cannot detect small individual plumes but it will detect a larger anomaly that would not be caught with the infrequent airborne surveys. This detection can trigger an aircraft to be sent to survey and further isolate individual plumes from the large anomaly. With both the airborne and satellite platforms, data on leaks can be quickly and efficiently communicated to oil, gas, and landfill operators to help them understand where to concentrate repair efforts. In addition, this can also help identify new sources and work with new industries to fix potential emissions. One example is the dairy industry; there are many large plumes coming from manure lagoons and dairy digesters but there is little effort to examine or mitigate these emissions.

The synthetic images have proven an excellent tool for sensitivity analysis and for looking at the potential of future sensors. As more sensors are designed, the framework pioneered in this dissertation will be important for the continual testing and analysis of the new sensors. In addition, as the application of imaging spectrometers moves beyond methane to other greenhouse gases, the synthetic images can be used to test other gases. Similar studies can and need to be done for carbon dioxide, water vapor, or nitrous oxide. As greenhouse gases continue to increase and more efforts are made to map and measure them, this type of work will continue to be necessary.

Bibliography

[1] G. Myhre, D. T. Shindell, F.-M. Breon, W. J. Collins, J. Fuglestvedt, J. Huang, D. Koch, J.-F. Lamarque, D. Lee, B. Mendoza, T. Kakajima, A. Robock, G. Stephens, T. Takemura, and H. Zhang, *Anthropogenic and Natural Radiative Forcing*, *Climate Change 2013: The Physical Science Basis. Contribution of Working Group I to the Fifth Assessment Report of the Intergovernmental Panel on Climate Change [Stocker,* (2013).

[2] S. Kirschke, P. Bousquet, P. Ciais, M. Saunois, J. G. Canadell, E. J. Dlugokencky, P. Bergamaschi, D. Bergmann, D. R. Blake, L. Bruhwiler, P. Cameron-Smith, S. Castaldi, F. Chevallier, L. Feng, A. Fraser, M. Heimann, E. L. Hodson, S. Houweling, B. Josse, P. J. Fraser, P. B. Krummel, J.-F. Lamarque, R. L. Langenfelds, C. Le Quéré, V. Naik, S. O'Doherty, P. I. Palmer, I. Pison, D. Plummer, B. Poulter, R. G. Prinn, M. Rigby, B. Ringeval, M. Santini, M. Schmidt, D. T. Shindell, I. J. Simpson, R. Spahni, L. P. Steele, S. a. Strode, K. Sudo, S. Szopa, G. R. van der Werf, A. Voulgarakis, M. van Weele, R. F. Weiss, J. E. Williams, and G. Zeng, *Three decades of global methane sources and sinks*, *Nature Geoscience* **6** (2013), no. September 813–823.

[3] M. Saunois, A. R. Stavert, B. Poulter, P. Bousquet, J. G. Canadell, R. B. Jackson, P. A. Raymond, E. J. Dlugokencky, S. Houweling, P. K. Patra, P. Ciais, V. K. Arora, D. Bastviken, P. Bergamaschi, D. R. Blake, G. Brailsford, L. Bruhwiler, K. M. Carlson, M. Carrol, S. Castaldi, N. Chandra, C. Crevoisier, P. M. Crill, K. Covey, C. L. Curry, G. Etiope, C. Frankenberg, N. Gedney, M. I. Hegglin, L. Höglund-Isaksson, G. Hugelius, M. Ishizawa, A. Ito, G. Janssens-Maenhout, K. M. Jensen, F. Joos, T. Kleinen, P. B. Krummel, R. L. Langenfelds, G. G. Laruelle, L. Liu, T. MacHida, S. Maksyutov, K. C. McDonald, J. McNorton, P. A. Miller, J. R. Melton, I. Morino, J. Müller, F. Murguia-Flores, V. Naik, Y. Niwa, S. Noce, S. O'Doherty, R. J. Parker, C. Peng, S. Peng, G. P. Peters, C. Prigent, R. Prinn, M. Ramonet, P. Regnier, W. J. Riley, J. A. Rosentreter, A. Segers, I. J. Simpson, H. Shi, S. J. Smith, L. Paul Steele, B. F. Thornton, H. Tian, Y. Tohjima, F. N. Tubiello, A. Tsuruta, N. Viovy, A. Voulgarakis, T. S. Weber, M. Van Weele, G. R. Van Der Werf, R. F. Weiss, D. Worthy, D. Wunch, Y. Yin, Y. Yoshida, W. Zhang, Z. Zhang, Y. Zhao, B. Zheng, Q. Zhu, Q. Zhu, and Q. Zhuang, *The global methane budget 2000-2017*, *Earth System Science Data* **12** (2020), no. 3 1561–1623.

[4] K. J. Wecht, D. J. Jacob, M. P. Sulprizio, G. W. Santoni, S. C. Wofsy, R. Parker, H. B??sch, and J. Worden, *Spatially resolving methane emissions in California: Constraints from the CalNex aircraft campaign and from present (GOSAT, TES) and future (TROPOMI, geostationary) satellite observations*, *Atmospheric Chemistry and Physics* **14** (2014), no. 15 8173–8184.

[5] a. J. Turner, D. J. Jacob, K. J. Wecht, J. D. Maasakkers, E. Lundgren, a. E. Andrews, S. C. Biraud, H. Boesch, K. W. Bowman, N. M. Deutscher, M. K. Dubey, D. W. T. Griffith, F. Hase, a. Kuze, J. Notholt, H. Ohyama, R. Parker, V. H. Payne, R. Sussmann, C. Sweeney, V. a. Velazco, T. Warneke, P. O. Wennberg, and D. Wunch, *Estimating global and North American methane emissions with high spatial resolution using GOSAT satellite data*, vol. 15. 2015.

[6] C. Zhao, A. E. Andrews, L. Bianco, J. Eluszkiewicz, A. Hirsch, C. MacDonald, T. Nehrkorn, and M. L. Fischer, *Atmospheric inverse estimates of methane emissions from Central California*, *Journal of Geophysical Research Atmospheres* **114** (2009), no. 16 1–13.

[7] S. Jeong, Y. K. Hsu, A. E. Andrews, L. Bianco, P. Vaca, J. M. Wilczak, and M. L. Fischer, *A multitower measurement network estimate of California's methane emissions*, *Journal of Geophysical Research Atmospheres* **118** (2013), no. 19 11339–11351.

[8] L. Hamlin, R. O. Green, P. Mouroulis, M. Eastwood, D. Wilson, M. Dudik, and C. Paine, *Imaging spectrometer science measurements for terrestrial ecology: AVIRIS and new developments*, *IEEE Aerospace Conference Proceedings* (2011) 1–7.

[9] G. P. Asner, D. E. Knapp, T. Kennedy-Bowdoin, M. O. Jones, R. E. Martin, J. Boardman, and C. B. Field, *Carnegie Airborne Observatory: in-flight fusion of hyperspectral imaging and waveform light detection and ranging (wLiDAR) for three-dimensional studies of ecosystems*, *Journal of Applied Remote Sensing* **1** (2007), no. 1 013536.

[10] T. U. Kampe, B. R. Johnson, M. Kuester, and M. Keller, *NEON: the first continental-scale ecological observatory with airborne remote sensing of vegetation canopy biochemistry and structure*, *Journal of Applied Remote Sensing* **4** (2010), no. 1 043510.

[11] R. O. Green, M. L. Eastwood, C. M. Sarture, T. G. Chrien, M. Aronsson, B. J. Chippendale, J. A. Faust, B. E. Pavri, C. J. Chovit, M. Solis, M. R. Olah, and O. Williams, *Imaging spectroscopy and the Airborne Visible/Infrared Imaging Spectrometer (AVIRIS)*, *Remote Sensing of Environment* **65** (1998), no. 3 227–248.

[12] L. S. Rothman, I. E. Gordon, A. Barbe, D. C. Benner, P. F. Bernath, M. Birk, V. Boudon, L. R. Brown, A. Campargue, J. P. Champion, K. Chance, L. H. Coudert,

V. Dana, V. M. Devi, S. Fally, J. M. Flaud, R. R. Gamache, A. Goldman, D. Jacquemart, I. Kleiner, N. Lacome, W. J. Lafferty, J. Y. Mandin, S. T. Massie, S. N. Mikhailenko, C. E. Miller, N. Moazzen-Ahmadi, O. V. Naumenko, A. V. Nikitin, J. Orphal, V. I. Perevalov, A. Perrin, A. Predoi-Cross, C. P. Rinsland, M. Rotger, M. Šimečková, M. A. H. Smith, K. Sung, S. A. Tashkun, J. Tennyson, R. A. Toth, A. C. Vandaele, and J. Vander Auwera, *The HITRAN 2008 molecular spectroscopic database*, *Journal of Quantitative Spectroscopy and Radiative Transfer* **110** (2009), no. 9-10 533–572.

[13] P. Forster and V. Ramaswamy, *Changes in Atmospheric Constituents and in Radiative Forcing*, *Climate Change 2007: The Physical Science Basis. Contribution of Working Group I to the Fourth Assessment Report of the Intergovernmental Panel on Climate Change* **30** (2007), no. 22 129–234.

[14] J. T. Kiehl and K. E. Trenberth, *Earth's Annual Global Energy Budget*, *Bulletin of the American Meteorological Society* **78** (1997), no. 2 197–208.

[15] D. a. Roberts, E. S. Bradley, R. Cheung, I. Leifer, P. E. Dennison, and J. S. Margolis, *Mapping methane emissions from a marine geological seep source using imaging spectrometry*, *Remote Sensing of Environment* **114** (mar, 2010) 592–606.

[16] H. H. Aumann, M. T. Chahine, C. Gautier, M. Goldberg, E. Kalnay, and L. Mcmillin, *AIRS / AMSU / HSB on the Aqua Mission : Design , Science Objectives , Data Products and Processing Systems*, *IEEE Geoscience and Remote Sensing Letters* **41** (2003), no. 2.

[17] H. Bovensmann, J. P. Burrows, M. Buchwitz, J. Frerick, S. Noël, V. V. Rozanov, K. V. Chance, and A. P. Goede, *SCIAMACHY: Mission objectives and measurement modes*, *Journal of the Atmospheric Sciences* **56** (1999), no. 2 127–150.

[18] H. Hu, J. Landgraf, R. Detmers, T. Borsdorff, J. Aan de Brugh, I. Aben, A. Butz, and O. Hasekamp, *Toward Global Mapping of Methane With TROPOMI: First Results and Intersatellite Comparison to GOSAT*, *Geophysical Research Letters* **45** (2018), no. 8 3682–3689.

[19] E. S. Bradley, I. Leifer, D. A. Roberts, P. E. Dennison, and L. Washburn, *Detection of marine methane emissions with AVIRIS band ratios*, *Geophysical Research Letters* **38** (2011), no. 10 n/a–n/a.

[20] A. K. Thorpe, D. A. Roberts, P. E. Dennison, E. S. Bradley, and C. C. Funk, *Point source emissions mapping using the Airborne Visible/Infrared Imaging Spectrometer (AVIRIS)*, *SPIE Proceedings-Algorithms and Technologies for Multispectral, Hyperspectral, and Ultraspectral Imagery XVIII* **8390** (may, 2012) 839013–1/9.

[21] C. C. Funk, J. Theiler, D. A. Roberts, and C. C. Borel, *Clustering to improve matched filter detection of weak gas plumes in hyperspectral thermal imagery*, *IEEE Transactions on Geoscience and Remote Sensing* **39** (2001), no. 7 1410–1420.

[22] A. K. Thorpe, D. a. Roberts, E. S. Bradley, C. C. Funk, P. E. Dennison, and I. Leifer, *High resolution mapping of methane emissions from marine and terrestrial sources using a Cluster-Tuned Matched Filter technique and imaging spectrometry*, *Remote Sensing of Environment* **134** (jul, 2013) 305–318.

[23] C. Frankenberg, U. Platt, and T. Wagner, *Iterative maximum a posteriori (IMAP)-DOAS for retrieval of strongly absorbing trace gases: Model studies for CH₄ and CO₂ retrieval from near infrared spectra of SCIAMACHY onboard ENVISAT*, *Atmos. Chem. Phys. Discuss.* **4** (2004), no. 5 6067–6106.

[24] A. K. Thorpe, C. Frankenberg, and D. A. Roberts, *Retrieval techniques for airborne imaging of methane concentrations using high spatial and moderate spectral resolution: application to AVIRIS*, *Atmospheric Measurement Techniques* **7** (feb, 2014) 491–506.

[25] C. Frankenberg, A. K. Thorpe, D. R. Thompson, G. Hulley, E. A. Kort, N. Vance, J. Borchardt, T. Krings, K. Gerilowski, C. Sweeney, S. Conley, B. D. Bue, A. D. Aubrey, S. Hook, and R. O. Green, *Airborne methane remote measurements reveal heavy-tail flux distribution in Four Corners region*, *Proceedings of the National Academy of Sciences* **113** (2016), no. 35 201605617.

[26] D. R. Thompson, A. K. Thorpe, C. Frankenberg, R. O. Green, R. Duren, L. Guanter, A. Hollstein, E. Middleton, L. Ong, and S. Ungar, *Space-based Remote Imaging Spectroscopy of the Aliso Canyon CH ₄ Super-emitter*, *Geophysical Research Letters* (2016).

[27] R. M. Duren, A. K. Thorpe, K. T. Foster, T. Rafiq, F. M. Hopkins, V. Yadav, B. D. Bue, D. R. Thompson, S. Conley, N. Colombi, C. Frankenberg, I. McCubbin, M. L. Eastwood, M. Falk, H. Herner, B. E. Croes, R. O. Green, and C. E. Miller, *California's Methane Super-Emitters*, tech. rep., 2019.

[28] A. K. Ayasse, P. E. Dennison, M. Foote, A. K. Thorpe, S. Joshi, R. O. Green, R. M. Duren, D. R. Thompson, and D. A. Roberts, *Methane mapping with future satellite imaging spectrometers*, *Remote Sensing* **11** (2019), no. 24.

[29] D. H. Cusworth, D. J. Jacob, D. J. Varon, C. Chan Miller, X. Liu, K. Chance, A. K. Thorpe, R. M. Duren, C. E. Miller, D. R. Thompson, C. Frankenberg, L. Guanter, and C. A. Randles, *Potential of next-generation imaging spectrometers to detect and quantify methane point sources from space*, *Atmospheric Measurement Techniques* **12** (2019), no. 10 5655–5668.

[30] D. J. Varon, J. McKeever, D. Jervis, J. D. Maasakkers, S. Pandey, S. Houweling, I. Aben, T. Scarpelli, and D. J. Jacob, *Satellite Discovery of Anomalously Large Methane Point Sources From Oil/Gas Production*, *Geophysical Research Letters* **46** (2019), no. 22 13507–13516.

[31] D. H. Cusworth, R. M. Duren, V. Yadav, A. K. Thorpe, K. Verhulst, S. Sander, F. Hopkins, T. Rafiq, and C. E. Miller, *Synthesis of Methane Observations Across Scales: Strategies for Deploying a Multitiered Observing Network*, *Geophysical Research Letters* **47** (2020), no. 7 0–3.

[32] P. Ciais, C. Sabine, G. Bala, L. Bopp, V. Brovkin, J. Canadell, A. Chhabra, R. DeFries, J. Galloway, M. Heimann, C. Jones, C. L. Quéré, R. Myneni, S. Piao, and P. Thornton, *Carbon and Other Biogeochemical Cycles*, *Climate Change 2013 - The Physical Science Basis* (2013) 465–570, [1011.1669].

[33] IPCC, *Inventory of U . S . Greenhouse Gas Emissions and Sinks : 1990 – 2014*, *IPCC* (2016).

[34] E. G. Nisbet, E. J. Dlugokencky, and P. Bousquet, *Methane on the Rise- Again*, *Science* **343** (2014), no. 6170 493–495.

[35] E. G. Nisbet, E. J. Dlugokencky, M. R. Manning, D. Lowry, R. E. Fisher, J. L. France, S. E. Michel, J. B. Miller, J. W. C. White, B. Vaughn, P. Bousquet, J. A. Pyle, N. J. Warwick, M. Cain, R. Brownlow, G. Zazzeri, M. Lanoisellé, A. C. Manning, E. Gloor, D. E. J. Worthy, E. Brunke, C. Labuschagne, E. W. Wolff, and A. L. Ganesan, *Rising atmospheric methane: 2007–2014 growth and isotopic shift*, *Global Biogeochemical Cycles* **30** (2016) 1356–1370.

[36] H. Schaefer, S. E. Fletcher, C. Veidt, K. R. Lassey, G. W. Brailsford, T. M. Bromley, E. J. Dlugokencky, S. E. Michel, J. B. Miller, I. Levin, D. C. Lowe, R. J. Martin, B. H. Vaughn, and J. W. White, *A 21st-century shift from fossil-fuel to biogenic methane emissions indicated by13CH4*, *Science* **352** (2016), no. 6281 80–84.

[37] S. Schwietzke, O. A. Sherwood, L. M. P. Bruhwiler, J. B. Miller, G. Etiope, E. J. Dlugokencky, S. E. Michel, V. A. Arling, B. H. Vaughn, J. W. C. White, and P. P. Tans, *Upward revision of global fossil fuel methane emissions based on isotope database*, *Nature* **538** (2016), no. 7623 88–91.

[38] M. Rigby, S. A. Montzka, R. G. Prinn, J. W. C. White, D. Young, S. O'Doherty, M. F. Lunt, A. L. Ganesan, A. J. Manning, P. G. Simmonds, P. K. Salameh, C. M. Harth, J. Mühle, R. F. Weiss, P. J. Fraser, L. P. Steele, P. B. Krummel, A. McCulloch, and S. Park, *Role of atmospheric oxidation in recent methane growth*, *Proceedings of the National Academy of Sciences* **114** (2017), no. 21 5373–5377.

[39] A. J. Turner, C. Frankenberg, P. O. Wennberg, and D. J. Jacob, *Ambiguity in the causes for decadal trends in atmospheric methane and hydroxyl*, *Proceedings of the National Academy of Sciences* **114** (2017), no. 21 5367–5372.

[40] D. J. Jacob, A. J. Turner, J. D. Maasakkers, J. Sheng, K. Sun, X. Liu, K. Chance, I. Aben, J. McKeever, and C. Frankenberg, *Satellite observations of atmospheric*

methane and their value for quantifying methane emissions, *Atmospheric Chemistry and Physics* **16** (2016), no. 22 14371–14396.

[41] C. Frankenberg, I. Aben, P. Bergamaschi, E. J. Dlugokencky, R. Van Hees, S. Houweling, P. Van Der Meer, R. Snel, and P. Tol, *Global column-averaged methane mixing ratios from 2003 to 2009 as derived from SCIAMACHY: Trends and variability*, *Journal of Geophysical Research Atmospheres* **116** (2011), no. 4 1–12.

[42] L. L. Strow, S. E. Hannon, S. De Souza-Machado, H. E. Motteler, and D. Tobin, *An overview of the AIRS radiative transfer model*, *IEEE Transactions on Geoscience and Remote Sensing* **41** (2003), no. 2 PART 1 303–313.

[43] T. Yokota, Y. Yoshida, N. Eguchi, Y. Ota, T. Tanaka, H. Watanabe, and S. Maksyutov, *Global Concentrations of CO2 and CH4 Retrieved from GOSAT: First Preliminary Results*, *Sola* **5** (2009) 160–163.

[44] R. O. Green, B. E. Pavri, and T. G. Chrien, *On-orbit radiometric and spectral calibration characteristics of EO-1 hyperion derived with an underflight of AVIRIS and In situ measurements at Salar de Arizaro, Argentina*, *IEEE Transactions on Geoscience and Remote Sensing* **41** (2003), no. 6 PART I 1194–1203.

[45] K. Gerilowski, A. Tretner, T. Krings, M. Buchwitz, P. P. Bertagnolio, F. Belemezov, J. Erzinger, J. P. Burrows, and H. Bovensmann, *MAMAP - A new spectrometer system for column-averaged methane and carbon dioxide observations from aircraft: Instrument description and performance analysis*, *Atmospheric Measurement Techniques* **4** (2011), no. 2 215–243.

[46] S. Krautwurst, K. Gerilowski, H. Jonsson, D. Thompson, R. Kolyer, A. Thorpe, M. Horstjann, M. Eastwood, I. Leifer, S. Vigil, T. Krings, J. Borchardt, M. Buchwitz, M. Fladeland, J. Burros, and H. Bovensmann, *Methane emissions from a Californian landfill , determined from airborne remote sensing and in-situ measurements Methane emissions from a Californian landfill , determined from airborne remote sensing and in-situ measurements*, *Atmos. Meas. Tech.* (2017), no. December 3429–3452.

[47] T. Krings, K. Gerilowski, M. Buchwitz, J. Hartmann, T. Sachs, J. P. Burrows, and H. Bovensmann, *Quantification of methane emission rates from coal mine ventilation shafts using airborne remote sensing data*, *Atmos. Meas. Tech.* (2013) 151–166.

[48] G. C. Hulley, R. M. Duren, F. M. Hopkins, S. J. Hook, N. Vance, P. Guillevic, W. R. Johnson, B. T. Eng, J. M. Mihaly, V. M. Jovanovic, S. L. Chazanoff, Z. K. Staniszewski, L. Kuai, J. Worden, C. Frankenberg, G. Rivera, A. D. Aubrey, C. E. Miller, N. K. Malakar, J. M. Sánchez Tomás, and K. T. Holmes, *High spatial resolution imaging of methane and other trace gases with the airborne Hyperspectral Thermal Emission Spectrometer (HyTES)*, *Atmospheric Measurement Techniques Discussions* (2016), no. February 1–32.

[49] D. M. Tratt, K. N. Buckland, J. L. Hall, P. D. Johnson, E. R. Keim, I. Leifer, K. Westberg, and S. J. Young, *Remote Sensing of Environment Airborne visualization and quanti fi cation of discrete methane sources in the environment*, *Remote Sensing of Environment* **154** (2014) 74–88.

[50] D. R. Thompson, B. C. Gao, R. O. Green, D. A. Roberts, P. E. Dennison, and S. R. Lundeen, *Atmospheric correction for global mapping spectroscopy: ATREM advances for the HyspIRI preparatory campaign*, *Remote Sensing of Environment* **167** (2015) 64–77.

[51] A. K. Thorpe, C. Frankenberg, D. R. Thompson, R. M. Duren, A. D. Aubrey, B. D. Bue, R. O. Green, K. Gerilowski, T. Krings, J. Borchard, E. A. Kort, S. Conley, D. A. Roberts, P. E. Dennison, J. Borchardt, E. A. Kort, C. Sweeney, S. Conley, D. A. Roberts, and P. E. Dennison, *Airborne DOAS retrievals of methane, carbon dioxide, and water vapor concentrations at high spatial resolution: Application to AVIRIS-NG*, *Atmospheric Measurement Techniques* **10** (2017), no. 10 3833–3850.

[52] P. E. Dennison, A. K. Thorpe, E. R. Pardyjak, D. a. Roberts, Y. Qi, R. O. Green, E. S. Bradley, and C. C. Funk, *High spatial resolution mapping of elevated atmospheric carbon dioxide using airborne imaging spectroscopy: Radiative transfer modeling and power plant plume detection*, *Remote Sensing of Environment* **139** (dec, 2013) 116–129.

[53] B.-C. C. Gao and A. F. H. Goetz, *Column atmospheric water vapor and vegetation liquid water retrievals from Airborne Imaging Spectrometer data*, *Journal of Geophysical Research* **95** (1990), no. D4 3549–3564.

[54] L. Guanter, K. Segl, and H. Kaufmann, *Simulation of Optical Remote-Sensing Scenes With Application to the EnMAP Hyperspectral Mission*, *IEEE Transactions on Geoscience and Remote Sensing* **47** (2009), no. 7 2340–2351.

[55] Z. Zhang, N. E. Zimmermann, A. Stenke, X. Li, E. L. Hodson, G. Zhu, C. Huang, and B. Poulter, *Emerging role of wetland methane emissions in driving 21st century climate change*, *Proceedings of the National Academy of Sciences* (2017) 201618765.

[56] A. Berk, P. Conforti, R. Kennett, T. Perkins, F. Hawes, and J. Van Den Bosch, *MODTRAN® 6: A major upgrade of the MODTRAN® radiative transfer code*, *Workshop on Hyperspectral Image and Signal Processing, Evolution in Remote Sensing* **2014-June** (2014) 1–4.

[57] F. Kruse, *Comparison of ATREM, ACORN, and FLAASH Atmospheric Corrections Using Low-Altitude AVIRIS Data of Boulder, CO*, *13th JPL Airborne Geoscience Workshop.* (2004) 1–10.

[58] C. J. Miller, *Performance assessment of ACORN atmospheric correction algorithm*, in *SPIE 4725, Algorithms and Technologies for Multispectral, Hyperspectral, and Ultraspectral Imagery VIII*, vol. 4725, pp. 438–449, 2002.

[59] S. M. Adler-Golden, M. W. Matthew, L. S. Bernstein, R. Y. Levine, A. Berk, S. C. Richtsmeier, P. K. Acharya, G. P. Anderson, J. W. Felde, J. A. Gardner, M. L. Hoke, L. S. Jeong, B. Pukall, A. J. Ratkowski, and H.-h. K. Burke, *Atmospheric correction for shortwave spectral imagery based on MODTRAN4*, in *SPIE's International Symposium on Optical Science, Engineering, and Instrumentation*, vol. 3753, pp. 61–69, 1999.

[60] M. W. Matthew, S. M. Adler-Golden, A. Berk, G. Felde, G. P. Anderson, D. Gorodetzky, S. Paswaters, and M. Shippert, *Atmospheric correction of spectral imagery: Evaluation of the FLAASH algorithm with AVIRIS data*, in *Applied Imagery Pattern Recognition Workshop*, pp. 157–163, 2002.

[61] R. Richter, *Atmospheric correction of DAIS hyperspectral image data*, *Computers & Geosciences* **22** (1996), no. 7 785–793.

[62] A. K. Thorpe, C. Frankenberg, A. D. Aubrey, D. A. Roberts, A. A. Nottrott, T. A. Rahn, J. A. Sauer, M. K. Dubey, K. R. Costigan, C. Arata, A. M. Steffke, S. Hills, C. Haselwimmer, D. Charlesworth, C. C. Funk, R. O. Green, S. R. Lundeen, J. W. Boardman, M. L. Eastwood, C. M. Sarture, S. H. Nolte, I. B. Mccubbin, D. R. Thompson, and J. P. McFadden, *Mapping methane concentrations from a controlled release experiment using the next generation airborne visible/infrared imaging spectrometer (AVIRIS-NG)*, *Remote Sensing of Environment* **179** (2016) 104–115.

[63] S. B. Carr, *The Aerosol Models in MODTRAN : Incorporating Selected Measurements from Northern Australia*, tech. rep., 2005.

[64] D. A. Roberts, M. Alonzo, E. B. Wetherley, K. L. Dudley, and P. E. Dennison, *Multiscale Analysis of Urban Areas Using Mixing Models*, in *Integrating Scale in Remote Sensing and GIS*, pp. 247–282. 2017.

[65] R. F. Kokaly, B. R. Couvillion, J. M. Holloway, D. A. Roberts, S. L. Ustin, S. H. Peterson, S. Khanna, and S. C. Piazza, *Remote Sensing of Environment Spectroscopic remote sensing of the distribution and persistence of oil from the Deepwater Horizon spill in Barataria Bay marshes*, *Remote Sensing of Environment* **129** (2013) 210–230.

[66] U. Platt, *Differential optical absorption spectroscopy (DOAS)*, in *Air monitoring by spectroscopic techniques*. John Wiley, New York, 1994.

[67] C. Frankenberg, J. F. Meirink, M. van Weele, U. Platt, and T. Wagner, *Assessing Methane Emissions from Global Space-Borne Observations*, *Science* **308** (2005), no. 5724 1010–1014.

[68] F. X. Kneizys, L. W. Abreu, G. P. Anderson, J. H. Chetwynd, E. Shettle, A. Berk, L. Bernstein, D. Robertson, P. Acharya, L. S. Rothman, J. E. A. Selby, W. O. Gallery, and S. A. Clough, *The MODTRAN 2/3 report and LOWTRAN 7 model*, tech. rep., 1996.

[69] R. N. Clark, *Spectroscopy of rocks and minerals, and principles of spectroscopy*, vol. 3. 1999.

[70] S. D. Bridgham, H. Cadillo-Quiroz, J. K. Keller, and Q. Zhuang, *Methane emissions from wetlands: Biogeochemical, microbial, and modeling perspectives from local to global scales*, *Global Change Biology* **19** (2013), no. 5 1325–1346.

[71] M. Saunois, A. R. Stavert, B. Poulter, P. Bousquet, Josep G. Canadell, R. B. Jackson, P. A. Raymond, E. J. Dlugokencky, S. Houweling, P. K. Patra, P. Ciais, V. K. Arora, D. Bastviken, P. Bergamaschi, N. Chandra, C. Crevoisier, P. M. Crill, K. Covey, C. L. Curry, G. Miller, J. R. Melton, I. Morino, J. Müller, F. Murguia-Flores, V. Naik, Y. Niwa, S. Noce, S. O'Doherty, R. J. Parker, C. Peng, S. Peng, G. P. Peters, C. Prigent, R. Prinn, M. Ramonet, Pierre Regnier, W. J. Riley, J. A., Rosentreter, A. Segers, I. J. Simpson, H. Shi, S. J. Smith, L. P. Steele, B. F. Thornton, H. Tian, Y. Tohjima, F. N. Tubiello, A. T. N. Viovy, A. Voulgarakis, T. S. Weber, M. van Weele, and Zhuang, *The Global Methane Budget 2000-2017*, *Journal of Chemical Information and Modeling* **53** (2019), no. 9 1689–1699, [1011.1669].

[72] EPA, *Global Anthropogenic Non-CO 2 Greenhouse Gas Emissions : 1990 - 2030 How to Obtain Copies How to Obtain the Data For Further Information :*, *Office of Atmospheric Programs Climate Change Division U.S. Environmental Protection Agency* (2011), no. August 1990–2030.

[73] D. T. Allen, D. W. Sullivan, D. Zavala-Araiza, A. P. Pacsi, M. Harrison, K. Keen, M. P. Fraser, A. D. Hill, B. K. Lamb, R. F. Sawyer, J. H. Seinfeld, D. W. Sullivan, D. Zavala-Araiza, M. Harrison, K. Keen, M. P. Fraser, A. D. Hill, R. F. Sawyer, and J. H. Seinfeld, *Methane emissions from process equipment at natural gas production sites in the United States: Pneumatic controllers*, *Environmental Science and Technology* **49** (2015), no. 1 633–640.

[74] X. Xiong, C. Barnet, E. Maddy, C. Sweeney, X. Liu, L. Zhou, and M. Goldberg, *Characterization and validation of methane products from the Atmospheric Infrared Sounder (AIRS)*, *Journal of Geophysical Research: Biogeosciences* **113** (2008), no. 3 1–14.

[75] D. H. Cusworth, D. J. Jacob, J. X. Sheng, J. Benmergui, A. J. Turner, J. Brandman, L. White, and C. A. Randles, *Detecting high-emitting methane sources in oil/gas fields using satellite observations*, *Atmospheric Chemistry and Physics* **18** (2018), no. 23 16885–16896.

[76] D. J. Varon, D. J. Jacob, J. McKeever, D. Jervis, B. O. A. Durak, Y. Xia, and Y. Huang, *Quantifying methane point sources from fine-scale satellite observations of atmospheric methane plumes*, *Atmospheric Measurement Techniques* **11** (2018), no. 10 5673–5686.

[77] M. Rast and T. H. Painter, *Earth Observation Imaging Spectroscopy for Terrestrial Systems: An Overview of Its History, Techniques, and Applications of Its Missions*, *Surveys in Geophysics* **40** (2019), no. 3 303–331.

[78] P. Stefano, P. Angelo, P. Simone, R. Filomena, S. Federico, S. Tiziana, A. Umberto, C. Vincenzo, N. Acito, D. Marco, M. Stefania, C. Giovanni, C. Raffaele, D. B. Roberto, L. Giovanni, and A. Cristina, *The PRISMA hyperspectral mission: Science activities and opportunities for agriculture and land monitoring*, *International Geoscience and Remote Sensing Symposium (IGARSS)* (2013) 4558–4561.

[79] R. Loizzo, R. . Guarini, F. . Longo, T. . Scopa, R. . Formaro, C. . Facchinetti, G. . Varacalli, I. Space, and A. Via, *PRISMA : THE ITALIAN HYPERSPECTRAL MISSION*, *IGARSS 2018 - 2018 IEEE International Geoscience and Remote Sensing Symposium* (2018) 2018–2021.

[80] L. Guanter, H. Kaufmann, K. Segl, S. Foerster, C. Rogass, S. Chabrillat, T. Kuester, A. Hollstein, G. Rossner, C. Chlebek, C. Straif, S. Fischer, S. Schrader, T. Storch, U. Heiden, A. Mueller, M. Bachmann, H. Mühle, R. Müller, M. Habermeyer, A. Ohndorf, J. Hill, H. Buddenbaum, P. Hostert, S. Van Der Linden, P. J. Leitão, A. Rabe, R. Doerffer, H. Krasemann, H. Xi, W. Mauser, T. Hank, M. Locherer, M. Rast, K. Staenz, and B. Sang, *The EnMAP spaceborne imaging spectroscopy mission for earth observation*, *Remote Sensing* **7** (2015), no. 7 8830–8857.

[81] T. Matsunaga, A. Iwasaki, S. Tsuchida, K. Iwao, J. Tanii, and O. Kashimura, *HISUI STATUS TOWARD FY2019 LAUNCH National Institute for Environmental Studies (NIES), Japan The University of Tokyo , Japan National Institute of Advanced Industrial Science and Technology (AIST), Japan Japan Space Systems , Japan*, .

[82] *Thriving on Our Changing Planet: A Decadal Strategy for Earth Observation from Space Committee*. The National Academies Press, Washington, DC, 2018.

[83] R. O. Green, N. M. Mahowald, R. N. Clark, B. L. Ehlmann, O. V. Ginoux, P. A. Kalashnikova, R. L. Miller, G. Okin, T. H. Painter, V. J. Pérez García-Pando, C. Realmuto, G. A. Swayze, E. Thompson, D. R. Middleton, L. Guanter, E. Ben Dor, and B. R. Phillips, *NASA's Earth Surface Mineral Dust Source Investigation*, 2018.

[84] J. W. Chapman, D. R. Thompson, M. C. Helmlinger, B. D. Bue, R. O. Green, M. L. Eastwood, S. Geier, W. Olson-Duvall, and S. R. Lundeen, *Spectral and radiometric calibration of the Next Generation Airborne Visible Infrared Spectrometer (AVIRIS-NG)*, *Remote Sensing* **11** (2019), no. 18.

[85] J. Theiler and B. R. Foy, *Effect of signal contamination in matched-filter detection of the signal on a cluttered background*, *IEEE Geoscience and Remote Sensing Letters* **3** (2006), no. 1 98–102.

[86] D. Manolakis and G. Shaw, *Detection Algorithms for Hyperspectral Imaging Applications*, *IEEE Signal Processing Magazine* (2002) 29–43.

[87] M. D. Foote, P. E. Dennison, A. K. Thorpe, D. R. Thompson, S. Jongaramrungruang, C. Frankenberg, and S. C. Joshi, *Fast and Accurate Retrieval of Methane Concentration From Imaging Spectrometer Data Using Sparsity Prior*, *IEEE Transactions on Geoscience and Remote Sensing* (2020) 1–13.

[88] B. K. Blaylock, J. D. Horel, and S. T. Liston, *Cloud archiving and data mining of High-Resolution Rapid Refresh forecast model output*, *Computers and Geosciences* **109** (2017), no. July 43–50.

[89] J. Horel and B. Blaylock, "Archive of the High Resolution Rapid Refresh model."

[90] EPA, *Methane and Nitrous Oxide Emissions from Natural Sources, a review*, 2010.

[91] E. A. Kort, C. Frankenberg, K. R. Costigan, R. Lindenmaier, M. K. Dubey, and D. Wunch, *Four corners: The largest US methane anomaly viewed from space*, *Geophysical Research Letters* (2014) 6898–6903.

[92] H. G. Bingemer and P. J. Crutzen, *The production of methane from solid wastes*, *Journal of Geophysical Research* **92** (1987), no. D2 2181.

[93] N. J. Themelis and P. A. Ulloa, *Methane generation in landfills*, *Renewable Energy* **32** (2007), no. 7 1243–1257.

[94] C. D. Goldsmith, J. Chanton, T. Abichou, N. Swan, R. Green, and G. Hater, *Methane emissions from 20 landfills across the United States using vertical radial plume mapping*, *Journal of the Air & Waste Management Association* **62** (2012), no. 2 183–197.

[95] *Thriving on Our Changing Planet*. 2018.

[96] M. Westerholm, J. Moestedt, and A. Schnürer, *Biogas production through syntrophic acetate oxidation and deliberate operating strategies for improved digester performance*, *Applied Energy* **179** (2016) 124–135.

[97] A. Townsend-Small, S. C. Tyler, D. E. Pataki, X. Xu, and L. E. Christensen, *Isotopic measurements of atmospheric methane in Los Angeles, California, USA: Influence of "fugitive" fossil fuel emissions*, *Journal of Geophysical Research Atmospheres* **117** (2012), no. 7 1–11.

[98] A. K. Ayasse, A. K. Thorpe, D. A. Roberts, C. C. Funk, P. E. Dennison, C. Frankenberg, A. Steffke, A. D. Aubrey, P. E. Dennison, C. C. Funk, and A. Teffke, *Evaluating the effects of surface properties on methane retrievals using a synthetic airborne visible/infrared imaging spectrometer next generation (AVIRIS-NG) image*, *Remote Sensing of Environment* **215** (2018), no. December 2017 386–397.

[99] R. M. Duren, A. K. Thorpe, K. T. Foster, T. Rafiq, F. M. Hopkins, V. Yadav, B. D. Bue, D. R. Thompson, S. Conley, N. K. Colombi, C. Frankenberg, I. B. McCubbin, M. L. Eastwood, M. Falk, J. D. Herner, B. E. Croes, R. O. Green, and C. E. Miller, *California's methane super-emitters*, *Nature* **575** (2019), no. 7781 180–184.

[100] S. Jongaramrungruang, C. Frankenberg, G. Matheou, A. K. Thorpe, D. R. Thompson, L. Kuai, and R. Duren, *Towards accurate methane point-source quantification from high-resolution 2D plume imagery*, *Atmospheric Measurement Techniques Discussions* (2019), no. May 1–22.

[101] G. Matheou and D. Chung, *Large-eddy simulation of stratified turbulence. Part II: Application of the stretched-vortex model to the atmospheric boundary layer*, *Journal of the Atmospheric Sciences* **71** (2014), no. 12 4439–4460.

[102] G. Matheou and K. W. Bowman, *A recycling method for the large-eddy simulation of plumes in the atmospheric boundary layer*, *Environmental Fluid Mechanics* **16** (2016), no. 1 69–85.

[103] S. C. Pryor, R. J. Barthelmie, D. T. Young, E. S. Takle, R. W. Arritt, D. Flory, W. J. Gutowski, A. Nunes, and J. Roads, *Wind speed trends over the contiguous United States*, *Journal of Geophysical Research Atmospheres* **114** (2009), no. 14.

[104] W. Marshall, *Michael Bloomberg, State Of California And Planet Partner To Deliver New Satellite Climate Data Solutions*, 2019.

[105] F. J. Massey, *The Kolmogorov-Smirnov Test for Goodness of Fit*, *Journal of the American Statistical Association* **46** (1951), no. 253 68–78.